Characterizing the antenna and gate of RIMFAX

Håkon Hellemo

Thesis submitted for the degree of
Master in Signal processing and imaging
60 credits

Department of Physics
Faculty of mathematics and natural sciences

UNIVERSITY OF OSLO

Autumn 2020

Characterizing the antenna and gate of RIMFAX

Håkon Hellemo

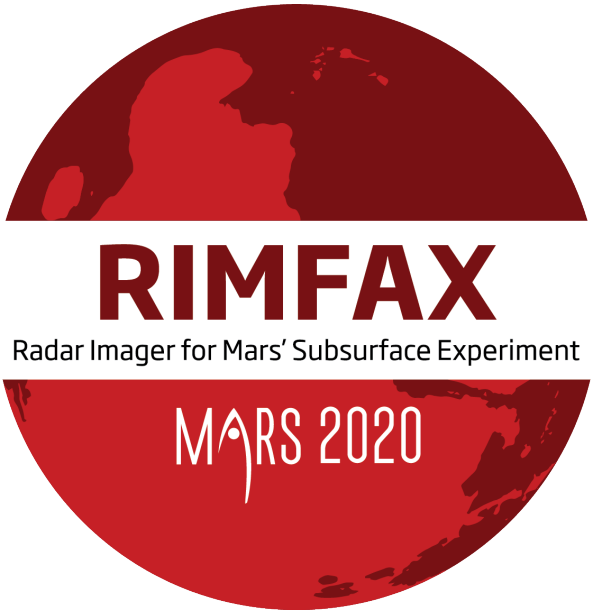

Characterizing the antenna and gate of RIMFAX

http://www.duo.uio.no/

Printed: Reprosentralen, University of Oslo

Abstract

Radar Imager for Mars' Subsurface Experiment (RIMFAX) is a Ground Penetrating Radar created for the Mars Perseverance rover mission. RIMFAX consists of an antenna and an electronic box which contains the transmitter/receiver of the radar. The objective of RIMFAX is to gather information about the subsurface of Mars. One piece of this information is the dielectric constant, which defines the electric properties of a material. In order to estimate the dielectric constant, it is important to have accurate models of the waves that are transmitted from the antenna. Thus, we have attempted to characterize the antenna of RIMFAX.

Measured radiation patterns have been interpolated with Spherical Harmonic functions. This method yielded good results at frequencies 150-220 MHz and 465-570 MHz. A Spectral Domain Fitting Model (SDFM) was used to interpolate the frequency behavior of the antenna. Due to difficulties in estimating the radiation efficiency of the antenna and inaccurate phase-information in the measured radiation patterns, this method was deemed unreliable. Far-field considerations led to two suggested frequency bands for estimating the dielectric constant; 465-570 MHz and 465-780 MHz.

The electronic box of RIMFAX separates the receiver, transmitter and antenna with a gate. This gate switches access to the antenna between the transmitter and receiver periodically. If the gate is set to transmit while a wave reflects back to the antenna, some proportion of the reflected wave will not be received. To correct for this, we have characterized the behavior of the gate. The lost energy due to gating results in an an amplitude change in the radar traces. We call this amplitude change the gate-function. The gate-function was estimated from measurements and showed similarities to its theoretical counterpart. It also seemed to have features that were not present in the theoretical function, indicating that the amplitude could be corrected more accurately with the estimated function.

Acknowledgements

Firstly, I would like to thank my supervisor Adjunct Professor Svein-Erik Hamran for the opportunity to work with something as exciting as space technology. Your guidance has really helped me to understand the core issues in my thesis. I would also like to thank my second supervisor Professor Sverre Holm for your encouragement and constructive feedback on the writing of my thesis.

Equally deserving of gratitude are my classmates, who offered great companionship and discussion through the lonely process of writing a masterthesis. My two dear friends Adrian and Mats also deserve recognition for their textual feedback.

I also must acclaim my family for their never-ending support. My grandfather Arthur has always been my inspiration for studying the workings of nature.

Thank you God. Had your grace not shone upon me, this would not have been possible.

Contents

List of Figures

List of Tables

Acronyms

A/D converter Analog/Digital converter. 35

CID Configuration ID. viii, 37, 38, 61–65, 75

CUDA Compute Unified Device Architecture. 29, 118

CW Continuous Wave. 61

DSP Digital Signal Processing. vii, 42, 43

EM Electromagnetic. 5

EQM Engineering Qualification Model. xv, 41

FFI Norwegian Defence Research Establishment. 3, 41

FFT Fast Fourier Transform. 35, 40

FMCW Frequency Modulated Continuous Wave. xv, 32, 35

GPR Ground Penetrating Radar. i, 3, 6, 7

I2EM The Improved IEM Scattering Model. v, 13, 76

IEM Integral Equation Method. xiii, 13

IF Instantaneous Frequency. 35, 36, 39, 40

IFFT Inverse Fast Fourier Transform. 42

ISO International Organization for Standardization. 23, 26

LFMCW Linear Frequency Modulated Continuous Wave. 35

LPDA Log-Periodic Dipole Array. 80–83

MBPE Model Based Parameter Estimation. 10, 31, 73, 77

MEDA Mars Environmental Dynamics Analyzer. 2

MOXIE Mars Oxygen In-Situ Resource Utilization Experiment. 2

MSE Mean squared error. 67

OLS Ordinary least squares. 28, 29, 32

PIXL Planetary Instrument for X-ray Litochemistry. 2

RIMFAX Radar Imager for Mars' Subsurface Experiment. i, ix, 2–4, 20, 25, 31–37, 41, 61, 74, 80–83, 125

RMS Root mean squared. 13

Rx Receive. 36

SDFM Spectral Domain Fitting Model. i, viii, 10, 22, 24, 31, 33, 57–59, 67, 73, 76–78

SH Spherical Harmonic. i, ix, 10, 22–24, 29, 34, 45, 46, 67, 68, 70, 76–78, 115, 117, 118

SHERLOC Scanning Habitable Environments with Raman & Luminescence for Organics & Chemicals. 3

Tx Transmit. 36

VNA Vector Network Analyzer. xv, 41, 42, 74

Glossary

cavity based method Cavity based methods are ways of estimating antenna efficiency where the antenna is placed inside a conducting chamber. The wheeler cap [1] is an example of such a method.. 78

correlation function The surface correlation function is defined as, $p(\xi) = \frac{\langle z(x,y)z(x',y')\rangle}{s^2}$. $p(\xi)$ is the measure of the degree of correlation between the surface at location (x, y) and the surface at location (x', y') [2].. xv

correlation length The correlation length is the value of ξ at which the correlation function, $p(\xi) = e^{-1}$.. 13

cut A cut of the radiation pattern refers to the samples that have been obtained by performing one full rotation of the mast in 3.2a. 29, 116

direct signal The "direct signal" refers to a VNA measurements made in the setup where the VNA is connected directly to the cable reflectors, as in Fig. 4.8b.. 41, 42, 61–65, 74, 75

euclidean 2-norm for a vector x, its euclidean norm (L2-norm) is $||x||_2 := \sqrt{x_1^2 + \cdots + x_n^2}$.. 28

gated signal The "gated signal" refers to the radar traces of the EQM when connected to a cable network. The setup is pictured in Fig. 4.8a.. 41, 42, 61–65, 74, 75

ramp-rate The rate of modulation of an FMCW radar.. 37

summing method the summing method is a radiation pattern interpolation method that sums the H-plane and E-plane of the radiation pattern to obtain a model of the full radiation pattern. This is further described in Section D.2.. 78

truncation order The truncation order of the spherical harmonic series (See. subsection 3.8.5). 46, 69

Chapter 1

Introduction

1.1 Background

1.1.1 The Mars Perseverance mission

The journey to Mars

Between 20. July and 5. August 2020, an Atlas V541 rocket will launch from Cape Canaveral Air force station in Florida. After the first stage of the rocket is done, the second stage will fire its engine twice. The first firing will get it into low earth orbit, and the second will propel the vehicle to Mars [3].

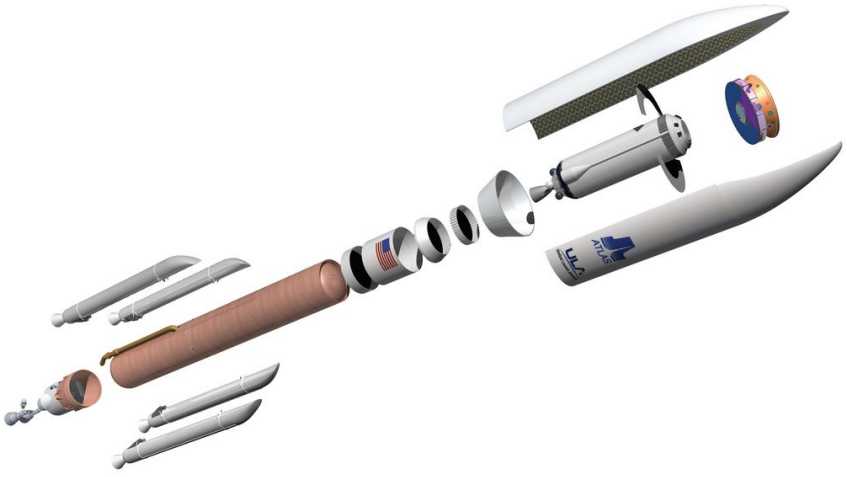

Figure 1.1: The Atlas V541 in parts. *Credits: NASA*

Upon reaching Mars the large heatshield will have to convert most of the kinetic energy into heat. When the payload has slowed down sufficiently, the descent vehicle of Fig. 1.2 will fire its engines and carry the rover safely to the surface. If all goes well, the *Perseverance* rover will reach the surface of Mars Feb. 18, 2021.

Figure 1.2: Descent vehicle. *Credits: NASA*

The Mars Perseverance rover

The *MARS Perseverance* rover is about the same size as a car, with a length of 3 meters and a width of 2.7 meters. It has six wheels, a robotic arm, and a mast standing about 2.2 meters tall [4]. Many instruments are mounted to the mast, the arm, and the body of the rover. All is powered by a generator that converts heat from the natural radioactive decay of plutonium to electricity. This power system charges the two primary batteries with approximately 110 watts. The rover can communicate directly with Earth, or via satellites that orbit Mars. The latter option provides considerably higher data-rates.

Perseverance has seven different science instruments [5]. **RIMFAX** is the instrument which is the object of this thesis. It is a ground-penetrating radar, meaning that it uses microwaves to "see" into the ground. In the next section this will be explained in more detail. **Mastcam-Z** can take stereoscopic pictures and video, and has the ability to zoom at distant targets. This can enable scientists to discover rocks that might contain evidence of past life. It is mounted on the mast of the rover, at a height of 2 meters. **MEDA** makes weather measurements. It can measure wind speed and direction, temperature, humidity, and can estimate the amount and size of dust particles in the atmosphere. Accurate prediction of weather will be important for future manned missions. The third instrument is **MOXIE**. It is a demonstration of how oxygen may be produced if we send people to Mars.

PIXL is an instrument that identifies chemical elements at a tiny scale. It is mounted at the end of the robotic arm. It has a camera that can take pictures up-close, and uses an X-ray spectrometer to analyze the chemical composition of rocks. This allows PIXL to detect signs of microbial life.

SHERLOC is another instrument that is mounted on the end of the robotic arm. SHERLOC also utilizes a fluorescence spectrometer, but it uses an UV-laser instead of the X-ray. It combines the spectrometer and the laser with a camera to search for organics, and minerals that may have been altered by watery environments.

SuperCam is the secondary instrument that is mounted on the mast of the rover. Similarly to SHERLOC, SuperCam uses spectrometers, laser and a camera to find rocks that may have been formed or changed in water. SuperCam is, however, a remote-sensing instrument, meaning that it is aimed at longer-range measurements compared to SHERLOC. In addition, SuperCam can provide data about atmospheric molecules that may be used for weather prediction.

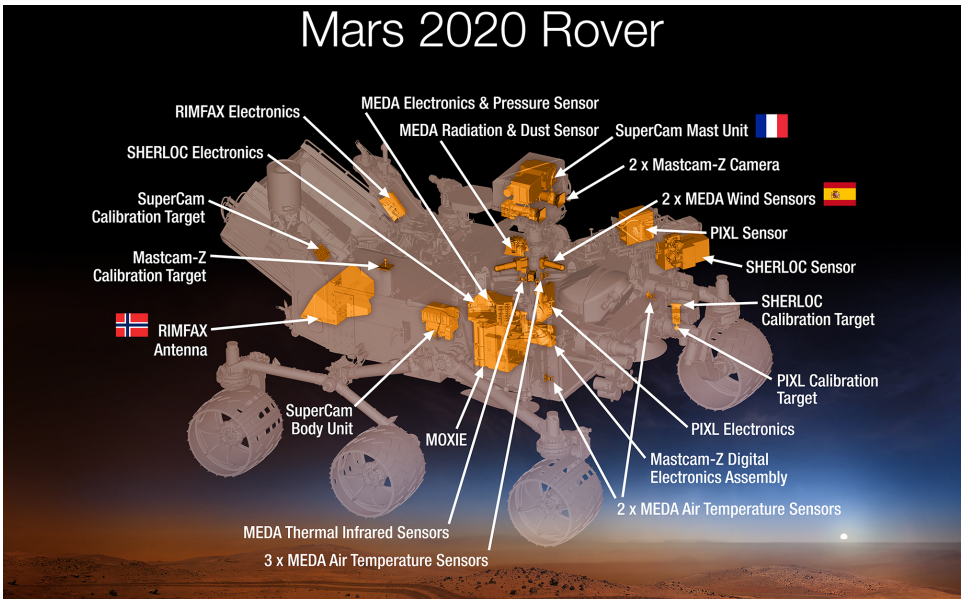

Figure 1.3: The instruments in the rover. *Credits: NASA*.

1.1.2 What is RIMFAX?

Radar Imager for Mars' Subsurface Experiment (RIMFAX), is a Ground Penetrating Radar developed by Norwegian Defence Research Establishment (FFI). The name is inspired by *Hrímfaxi*, a horse from Norse mythology, that draws *Nótt* (night) across the sky. Radar is an instrument used to detect objects with electromagnetic waves. It relies on an antenna, which directs the EM-waves in a particular direction, a signal transmitter and a receiver. There is also a duplexer, which is responsible for the signal flow between the transmitter/receiver and the antenna. A duplexer can either be a "gate" that periodically switches between the transmitter and receiver, or it can be a circulator, which gives continuous access to the antenna for both the transmitter and receiver.

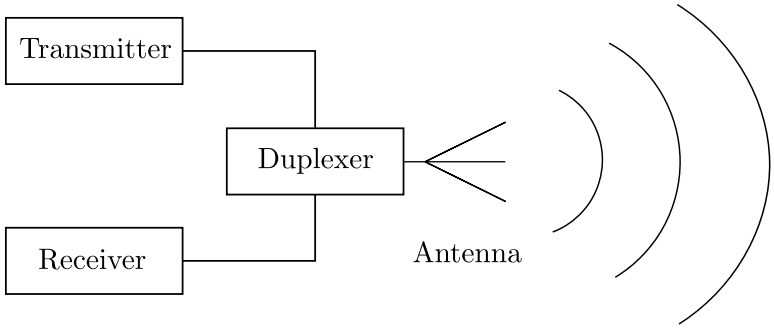

Figure 1.4: Radar system diagram

RIMFAX is "gated", in order to prevent leakage from the transmitter to the receiver. The antenna, which is located underneath the rover (see Fig. 1.3), emits microwaves into the ground, and captures the waves that return. The receiver can then generate a trace of measurements. The depth of each of these measurements is proportional to the sampled time, by the wave velocity. By moving the rover and repeating this process, we can stack many traces on top of each other to generate an image of the subsurface. An example of this is illustrated in Fig. 1.5.

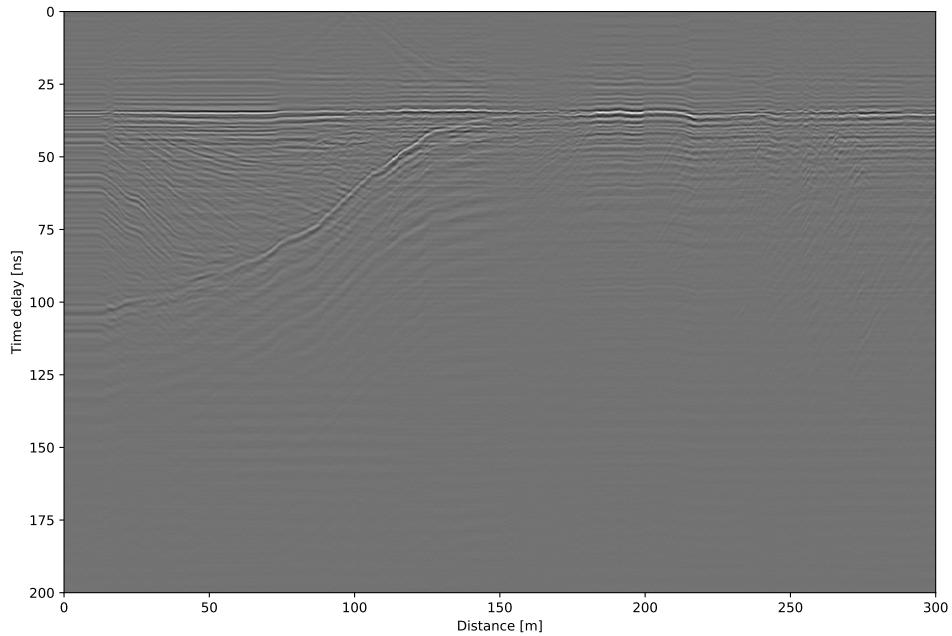

Figure 1.5: RIMFAX data from Coral Pink Sand Dunes in Utah. The sloping single reflector which starts at $\sim$ 100 ns is likely to be bedrock [6]. As the rover moves over the sand dunes the distance to bedrock changes.

In this figure, the traces are stacked column-wise. The x-axis represents distance from the original position of the rover.

To understand what this image shows us, we need to know how EM-waves behave. When electromagnetic waves propagate in the ground, they travel through many different mediums. Upon entering a new medium, the wave will split into two waves, a reflected wave and a transmitted wave.

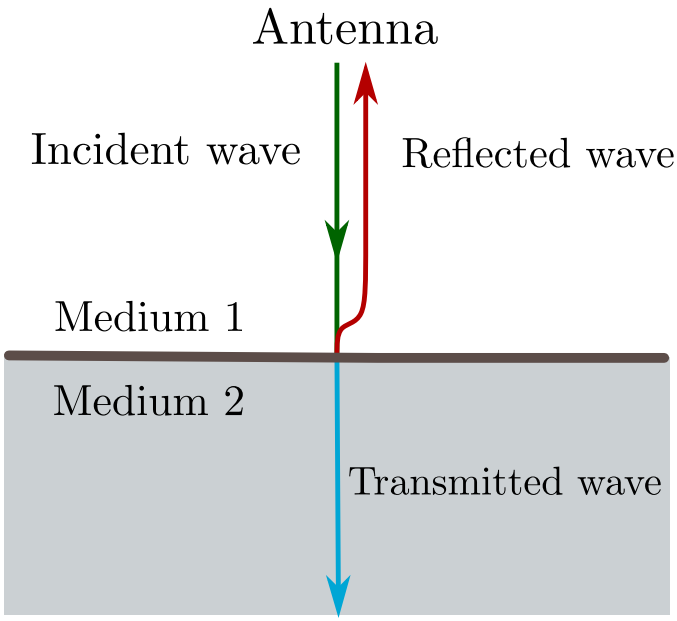

Figure 1.6: Wave reflection

The waves that reflect back to the receiver at some point are possible to measure. All radars rely on this principle, that EM-waves reflect when entering a medium with different electromagnetic properties. By gathering data about the reflected wave, we can characterize the medium it has traveled through.

1.1.3 The research objective of this thesis

The main goal of this thesis is the following: Laying the groundwork for measuring the dielectric constant of the surface layers on Mars. The principle illustrated in Fig. 1.6 will be used to accomplish this.

Electromagnetic wave theory posits that the strength of a reflected wave is related to the strength of the incident wave by the dielectric constant. We can, inversely, compute the dielectric constant if we know the strength of the two waves. The same result can be achieved by not modeling the transmitted/reflected waves directly, but instead relating the received/transmitted power to the dielectric constant using Friis transmission formula or the radar equation. These models are described in chapter 2.

For some of these models, the spatial behavior of antenna gain is required. Because the transmitted signal may have a large bandwidth, we also need to characterize the frequency behavior of the antenna. The received data also need to be corrected for the gate, which removes some of the signal

energy during transmit and receive. Finally, the surface reflection needs to be found in the corrected data. In summary, the procedure is:

1. Model the power of the received wave relative to the transmitted wave. (Suggestions for this are in chapter 2)
2. Characterize the spatial/frequency behavior of antenna gain. (See chapter 3)
3. Correcting the received data for the gate. (See chapter 4)
4. Extracting the surface reflection. (This part has not been done)

Step 3 of this list is not only necessary for estimating the dielectric constant. To properly "see" what is underground, the amplitude change applied by the gate needs to be corrected.

1.1.4 The history of Ground Penetrating Radar

The first reported attempt at measuring subsurface features with radar was in 1956, where the interference pattern, along with knowledge about the average dielectric constant of the medium was used to estimate the distance to the underground water table [7].

A few years later, in 1961, the US Air Force reported altimeter errors when attempting to land aircraft on the Greenland ice sheet. This was the first repeatable indication of subsurface penetration through a naturally occurring material. Electromagnetic waves attenuate little when propagating through ice, and thus can reflect detectable responses at large depths.

Further research was done on ice glaciers in the 1960s. Other use-cases, such as coal- and salt-mines were explored, as they contain low-loss dielectric materials in some instances.

It was believed that the lunar subsurface had similar electrical characteristics to that of ice. Thus, techniques similar to that of [7] was used on the lunar orbiter. Interpretation of the radar images led them to find features that had been formed by surface volcanic flows [8]. The lunar orbiter carried a pulsed radar, similar to the ice sounders that were used in the 60s.

In the 1970s The Geological Survey of Canada explored many applications for Ground Penetrating Radar. One example was the need for pipelines to carry oil and gas through the Canadian arctic. Ground Penetrating Radar was used to better understand the permafrost terrain in the region. Another example was the use of borehole radar to investigate rock quality for proposed nuclear disposal sites.

The interest for Ground Penetrating Radar declined at the beginning of the 1980s, as people realized that many environments were not suitable. As the 90s came, a new interest sparked for Ground Penetrating Radar, as many

organizations utilized the rapidly increasing computational power. One of the developments was the commercial use of Ground Penetrating Radar for landmine detection.

In 2019 the Norwegian Institute for Cultural Heritage Research (NIKU) found a Viking ship in Norway [9]. It was discovered from the images generated by a Ground Penetrating Radar; the MALÅ 3D Imaging Radar Array (MIRA). This system, developed by Guideline Geo, does imaging in all three spatial dimensions. Similarly to an MRI, it can create slices of the underground and show these as images at different depths.

The main source of information for this section has been [10, p. 3-7].

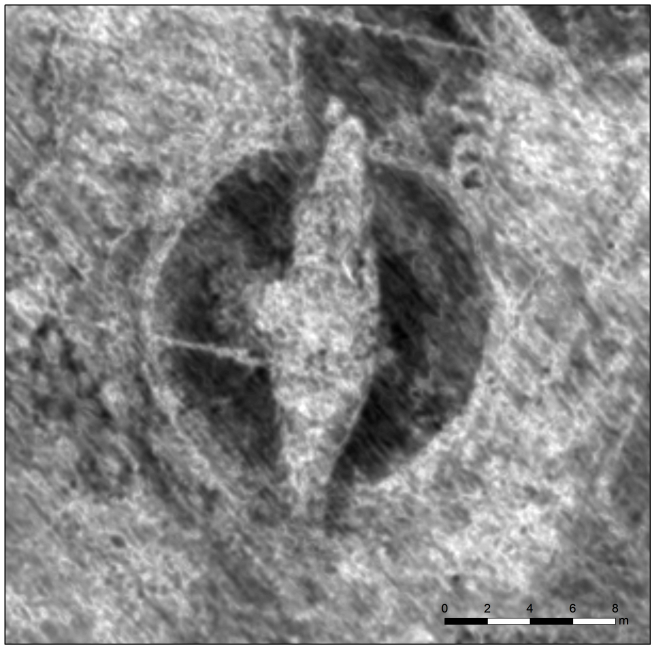

Figure 1.7: Viking ship image. *Credits: NIKU*.

1.2 Motivation

1.2.1 The objectives of RIMFAX

The Mars Perseverance rover project has four stated objectives [11]:

- **Looking for Habitability:** Identify past environments capable of supporting microbial life.
- **Seeking Biosignatures:** Seek signs of possible past microbial life in those habitable environments, particularly in special rocks known to preserve signs of life over time.
- **Caching Samples:** Collect core rock and "soil" samples and store them on the Martian surface
- **Preparing for Humans:** Test oxygen production from the Martian atmosphere

RIMFAX aims to contribute to the first two objectives. As there is not much water on Mars, the microwaves that RIMFAX produces can penetrate far into the ground. It will be the first instrument to extract high-resolution stratigraphic information about the Martian subsurface. Before this, we have only been able to "see" a few cm into the subsurface of Mars. RIMFAX can, in comparison, receive data from several meters below the surface.

The layers of sediment, rock, ice, water or saltwater reveal a record of the ancient climate conditions on Mars. RIMFAX can access this information because the waves that are reflected reveal electromagnetic properties about the materials and their structure.

Water is one of the building blocks for all life on Earth. Thus, the detection of water, or an environment that has contained water, is a major advancement for our knowledge about the possibility for life on Mars; past, present, or future. It is ironic that water is in one sense a "curse", when dealing with radar, but at the same time is the very objective of this mission.

1.2.2 How this thesis contributes to the RIMFAX objectives

The problem to be solved in this thesis was introduced in section 1.1.3. Below is one of the reasons why obtaining estimates of the dielectric constants is important. The density of the surface can be calculated from the dielectric constant and it is one component of information about the "regolith". Regolith is a term that was coined in 1897 by the geologist R. B. Merrill. The regolith designates the fragmental layer of rock that mantles the Earth's surface. On Earth this is manifested as soil. The Earth's soil contains large amounts of organic carbon and weathered rocks, that have been moved by wind or water. Living organisms have also played a major role in the forming of the Earth's regolith. In contrast, the Moon's regolith has never been disturbed by wind, water or organic life. It consists of rock fragments that

range from submicron dust to meter-sized blocks. The Moon's regolith is maintained by meteorites and the radiation from open space [12, p. 276].

Because of how organic life, water, etc. shapes the regolith, we may gain insight about a planet's history by inspecting it.

1.3 Outline

- **Chapter 1 - Introduction**
  The introduction is aimed at sparking the readers interest, by explaining the greater context of this project. It presents the research objective of this thesis and relates it to the goals of the *Mars Perseverance* mission.

- **Chapter 2 - Estimating the dielectric constant**
  This chapter presents three suggestions for calculating the dielectric constant from the measurement data on Mars and the antenna characteristics.

- **Chapter 3 - Characterizing the antenna**
  Starts with a description of how measurements of the antenna radiation pattern was obtained. Furthermore, the geometry of these measurements is defined mathematically, and it is shown how these can be transformed into more useful coordinate systems. Finally, a method of using Spherical Harmonic (SH) functions to interpolate the full 3D radiation pattern from the measurements is detailed, in addition to a Model Based Parameter Estimation (MBPE) approach for interpolating the frequency characteristics of the antenna.

- **Chapter 4 - Characterizing the gate**
  Explains some of the inner workings of the gate, which is used to switch between transmit- and receive-mode. Some models for how the gate works "ideally" are presented. Finally, we derive a method to estimate the gate-function using measurements, and then show its DSP-implementation.

- **Chapter 5 - Results**
  This chapter shows the SH-interpolation results at three frequencies; 150, 500 and 1130 MHz. The results from the SDFM-interpolation are also displayed. Finally the estimated gate-function is shown for several configurations of the gate.

- **Chapter 6 - Discussion**
  This chapter discusses the results of the SH- and SDFM-interpolation. The accuracy of the interpolated radiation pattern is evaluated. The features of the estimated gate-function are compared to the theoretical one. Finally the results are discussed with regard to estimating the dielectric constant.

- **Chapter 7 - Conclusion and future works**
  The conclusion summarizes the discussion and presents ideas for improving the methods used in this thesis. Some proposals for future projects are then stated.

Chapter 2

Estimating the dielectric constant

2.1 Overview

Three suggestions for estimating the dielectric constant will be presented in this chapter . The first model only uses the measured boresight gain to estimate the dielectric constant. The two other models require interpolation of the antenna gain, and are thus important motivations for chapter 3.

2.2 Using the Normal incidence model

The simplest method to estimate the dielectric constant is to calculate the Fresnel reflection coefficient Γ at normal incidence, with the transmit and receive gain set to maximum gain. Friis transmission formula can be then be used to relate the received/transmitted power to the Fresnel reflection coefficient:

$$\frac{P^r}{P^t} = G_{max}^2 \left(\frac{\lambda}{4\pi R}\right)^2 \Gamma \tag{2.1}$$

The reflection coefficient can then be used to calculate the intrinsic impedance:

$$\Gamma = \left|\frac{\eta_t - \eta_i}{\eta_t + \eta_i}\right|^2 \tag{2.2}$$

which can be used, under the assumption that the medium is lossless[1], to calculate the dielectric permittivity $\varepsilon = \varepsilon'\varepsilon_0$ of the transmit[2] medium:

$$\eta = \sqrt{\frac{\mu_0}{\varepsilon'\varepsilon_0}} \tag{2.3}$$

The magnetic permeability in free-space is $\mu_0 = 4\pi \times 10^{-7} H/m$, and the permittivity of free-space is $\varepsilon_0 = 8.85 \times 10^{-12} F/m$.

[1] Probably a fair approximation due to the absence of liquid water in the Martian subsurface.

[2] Here referring to Fig. 1.6.

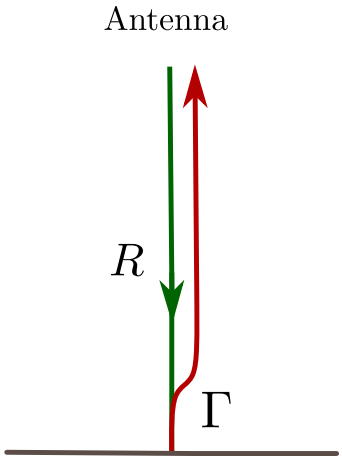

Figure 2.1: Reflection at normal incidence.

2.3 Taking the mean of the interpolated gain

The gain of the antenna may vary a lot for different directions, and the distance $R \approx 60cm$ is quite small relative to the size of the antenna $l \approx 20cm$. Because of this, even specular reflections will return back to the antenna, for small angles. We suggest averaging the antenna gain over a small surface on the ground to improve the normal incidence model.

$$\frac{P_p^r}{P_q^t} = mean\left\{G(\theta_m, \phi_m)^2\right\}\left(\frac{\lambda}{4\pi R}\right)^2 \Gamma_{pq} \tag{2.4}$$

The surface should at least be smaller than the Fresnel zone (See Fig. 2.2), as this marks the surface from which reflections will add constructively. However, the Fresnel zone is rather large for a large part of the frequency band of this radar. For example, at 500 MHz the Fresnel angle is $\theta_f \approx 37°$. For this frequency, a smaller surface should be used, because of the incidence angle dependency of the reflection coefficient, distance, etc.

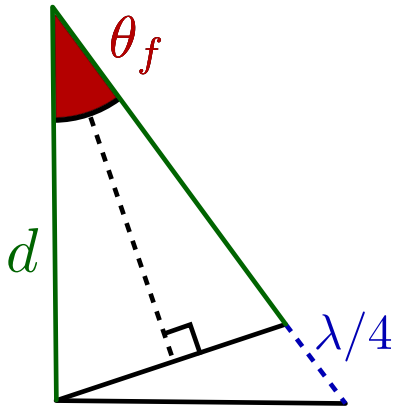

Figure 2.2: The Fresnel zone corresponds to values of theta $\theta < \theta_f$.

2.4 Applying the I2EM back-scattering model

A third option for estimating the dielectric constant is to apply a backscattering model of the surface. We can then average the radar equations model of received/transmitted power. This may give more accurate results, as we can average over a much larger surface. The following equation is often referred to as "the radar equation":

$$\frac{P_p^r}{P_q^t} = mean\left\{\frac{G(\theta_m,\phi_m)^2\lambda^2}{(4\pi)^3R^4}\sigma_{pq}(\theta_m)\right\} \tag{2.5}$$

The Improved IEM Scattering Model (I2EM) can estimate back-scattering as a function of the dielectric constant, RMS height, RMS-slope and the correlation length of the surface. It also takes frequency, incidence angle and polarization parameters.

Because of this, we can create a forward model of back-scattering, relative to the dielectric constant when the roughness of the surface is known. These features can perhaps be estimated by using image analysis techniques on pictures of the surface of Mars. By putting the back-scattering model into the right-side of Eq. 2.5, we can find the dielectric constant that makes the right-side equal to the left-side.

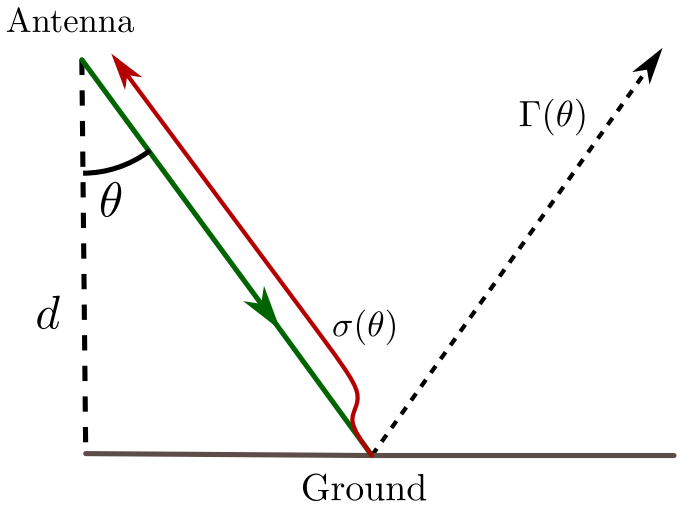

Figure 2.3: Back-scattering $\sigma(\theta)$ and specular reflection $\Gamma(\theta)$.

Chapter 3

Characterizing the antenna

3.1 Overview

In subsection 1.1.3 one of the tasks of this thesis was presented: *'Model the spatial/frequency behavior of the antenna gain'*. The intended application of this is to estimate the dielectric constant with better accuracy than when using the normal incidence model from Eq. 2.1. Knowledge of how the transmitted radiation is distributed might also be beneficial for general interpretation of the received signal.

The following section in this chapter explains how the characteristics of antennas depend on distance, and how we can model their radiation in the far field. Then, it is explained how measurements of the radiation pattern was obtained, and how this data can be represented in different coordinate systems. A few spatial interpolation methods are discussed, and the chosen interpolation method is explained in detail. Finally, a method to interpolate the radiation pattern in the frequency domain is outlined.

3.2 Electromagnetic characteristics

The electromagnetic characteristics of antennas vary with distance, and are typically divided into three regions [13]:

1. The reactive near field is the region adjacent to the antenna. The E-field and H-field are 90-degrees out of phase in this region. To radiate the E- and H-field need to be orthogonal and in phase with each other.

2. The radiative near field is the region where the electromagnetic fields start to transition from reactive to radiating fields. The radiation pattern still varies with distance.

3. The far field is where the electromagnetic fields are dominated by radiating fields. The E- and H-fields and the direction of propagation are orthogonal. The radiation pattern changes very little with distance.

If we are in the far field of an antenna, we can treat it as a direction- and frequency-dependent amplifier. The gain of the antenna can be written as,

$$G(\theta, \phi) = \epsilon \cdot D(\theta, \phi) \tag{3.1}$$

where $\epsilon = P_{rad}/P_{in}$ is the amount of radiated power relative to input power (efficiency), and $D(\theta, \phi)$ is the radiation intensity in a particular direction, relative to the mean radiation intensity.

$$D(\theta, \phi) = \frac{U(\theta, \phi)}{\overline{U}} \tag{3.2}$$

3.3 Far field region

There are many models for determining the boundary between the near field and the far field. Charles Capps [14] has explained the theoretical background for some of these definitions.

3.3.1 Phase difference model

Under the assumption that the length of an antenna is much shorter than the distance to an object of interest, Charles Capps [14] has shown that we can approximate the far field boundary with respect to antenna length. If we allow a phase error of $\pi/16$, the far field is,

$$r = \frac{4l^2}{\lambda}$$

where l is the length of the antenna. In our case the antenna size is not that small relative to the distance to the ground. Its longest side is approximately one third the distance to the ground. However, the term that has been removed in the approximation from [14, Eq. 9] is the square of the antenna length, so that makes it less significant. Still, this estimation of the far field should only be seen as a rough estimate, and it should only be used for a relatively small solid angle. This is because the phase differences increase substantially when waves approach the antenna at greater angles.

3.3.2 Wave impedance model

The wave impedance model for estimating the far field boundary looks at how the wave impedance changes with distance. The wave impedance is used to calculate the Fresnel reflection coefficient, so we should investigate this method for defining the far field. To calculate the far field boundary we need to determine how high an error in wave impedance we deem acceptable. If we are willing to accept a higher error, we get a closer far field.

From [14, Fig. 2] we see that an acceptable error of $\pm 20\%$ in wave impedance puts the far field at:

$$r = \frac{3\lambda}{2\pi}$$

Setting the error margin to $\pm 10\%$, gives:

$$r = \frac{5\lambda}{2\pi}$$

These far-field estimates were derived in [14] by calculating the electric and magnetic field equations of a short current element in a vacuum. As long as there are no other conductors, these equations can be scaled by the dielectric permittivity and magnetic permeability to obtain the field equations of any medium. This means that the statement that the wave impedance is proportional to the intrinsic impedance of a vacuum [14], can be extended to any lossless medium:

$$\eta_{wave} = c \cdot \eta_{intrinsic}$$

c depends on range, frequency and antenna length. Thus, the Fresnel reflection equation will give the same result even if the wave impedance hasn't yet converged to the intrinsic impedance of the medium:

$$\Gamma = \left| \frac{c\eta_t - c\eta_i}{c\eta_t + c\eta_i} \right|^2 = \left| \frac{\eta_t - \eta_i}{\eta_t + \eta_i} \right|^2$$

When the medium is lossy it is much more challenging to estimate the potential errors in the Fresnel reflection coefficient. One of the reasons for this is that [14, p. 96] has only derived the electric- and magnetic-field equations for the case where the medium is a vacuum. If there is conductance in other places than the antenna, Maxwell's equations will give different results. Also, the errors that arise in the Fresnel reflection coefficient are very much dependent on the true impedance. We suggest that a detailed analysis of the wave impedance errors is performed if the dielectric constant is to be estimated.

3.3.3 The estimated far field

In Table 3.1 we see that the phase difference far field doesn't limit the frequency band we can use, as every frequency, except 1200MHz, puts the far field above ground level. As we discussed in subsection 3.3.2 the wave impedance doesn't constrain the far field if the medium is lossless. This doesn't hold generally, so we will investigate the far-field for the two error margins. If the transmitted frequency is above 220 MHz, the far-field is above the ground for the 20% error model. This constrains us to the frequency band 220-1130 MHz. The 10% error margin requires a frequency of 430 MHz or higher to put the far-field above the ground.

Frequency	Phase difference	Impedance 20%	Impedance 10%
150	0.08	0.95	1.59
220	0.11	0.65	1.08
290	0.15	0.49	0.82
360	0.19	0.39	0.66
430	0.22	0.33	0.55
500	0.26	0.28	0.47
570	0.30	0.25	0.41
640	0.34	0.22	0.37
710	0.37	0.20	0.33
780	0.41	0.18	0.30
850	0.45	0.16	0.28
920	0.49	0.15	0.25
990	0.52	0.14	0.24
1060	0.56	0.13	0.22
1130	0.60	0.12	0.21
1200	0.64	0.11	0.19

Table 3.1: The second column shows the estimated far field in meters, for the phase difference model from subsection 3.3.1. The third and fourth column shows the far field for the impedance model, from subsection 3.3.2, with 20% and 10% error margin, respectively.

3.4 The antenna measurements by Comrod

3.4.1 Overview

Comrod has performed electric field measurements of the RIMFAX antenna in receive-mode. They placed the antenna on top of a rotating mast, with a coaxial cable for recording the received signal. By transmitting from another antenna, and rotating the mast, they obtained directivity patterns for several cuts of the full 3D-pattern.

Measurements were made in both the E-plane and the H-plane of the antenna, by rotating the antenna relative to the mast, like in Fig. 3.2a and Fig. 3.2b. The E-plane is defined by the electric field lines of the antenna (See Fig. 3.1), while the H-plane is in the same plane as the curl of the electric field. Horizontal polarization was used in the E-plane configuration while vertical polarization was used in the H-plane configuration.

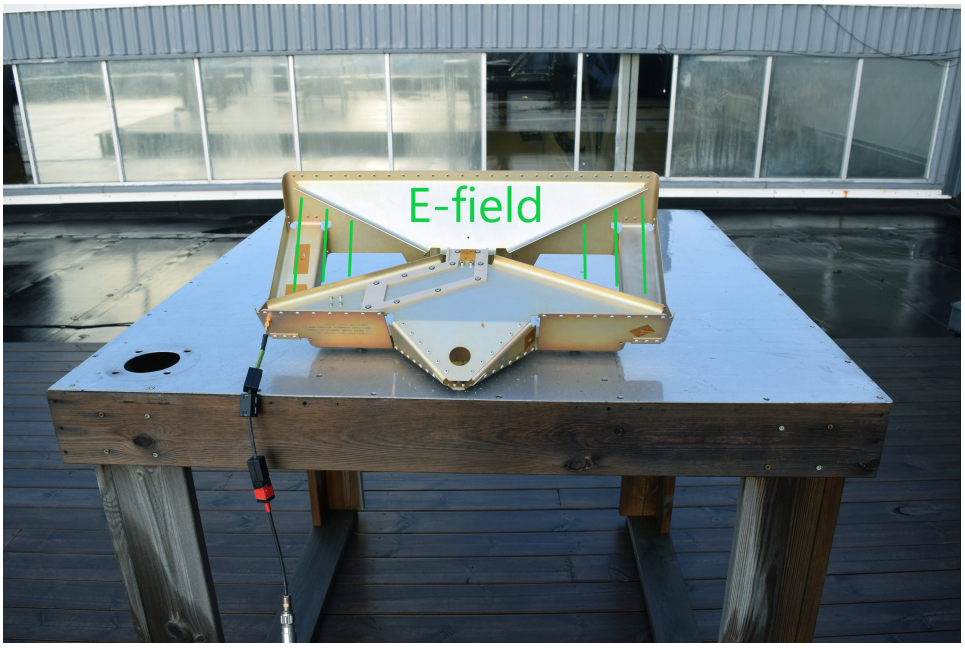

Figure 3.1: The E-plane is defined by the electric field lines of the antenna.

(a) Measurement configuration for the E-plane pattern.

(b) Measurement configuration for the H-plane pattern.

Figure 3.2: The E-plane and H-plane antenna configurations. Source: [15]

3.4.2 The coordinates of the measurements

The mast was tilted at three different angles, $-20°, 0°, +20°$ to change the axis of rotation. Tilting the mast, and rotating the antenna, produced in total six different orientations. We call these orientations Hm20, H, Hp20, Em20, E and Ep20. The p20 or m20 suffix represents the angle orthogonal to the plane specified in the prefix (H or E). For the H-plane, this angle is the β-angle from Fig. 3.3a. In the E-plane it is α from Fig. 3.3b.

The geometry of these orientations can be seen in the radiation pattern illustrated in Fig. 3.4. Most of this information was interpreted from [15] and the MATLAB code that accompanied it.

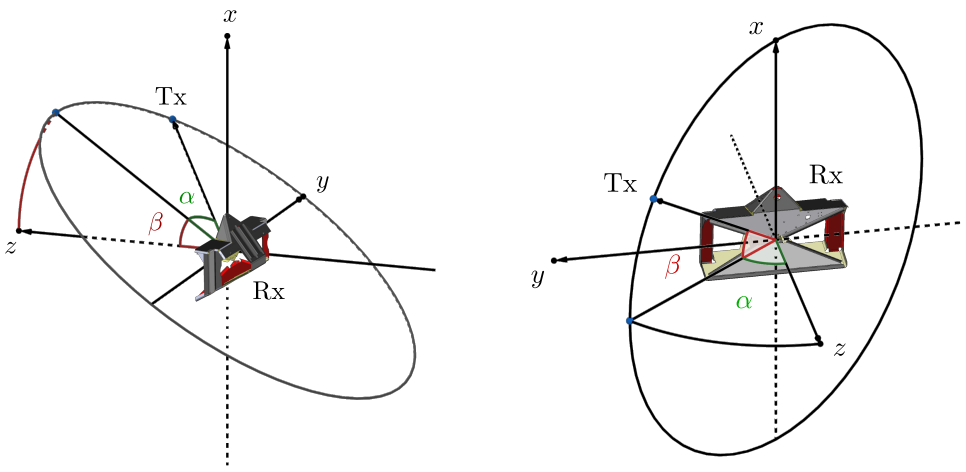

(a) YZ-plane (H-plane) coordinates.

(b) XZ-plane (E-plane) coordinates.

Figure 3.3: Tilting and rotating the mast with the receiver antenna is physically equivalent (with respect to the antennas' relative positions) to keeping the Rx-antenna in a fixed position, and moving the transmitter antenna along the circles.

3.4.3 Measurement files

The measurements were stored in files which had a layout like Fig. D.1. Each file has a specified frequency-range; 150-500 MHz or 500-1200 MHz. An overview of these frequency-ranges can be seen in Fig. D.2. The cuts of the radiation patterns are stored as complex electric field measurements, scaled such that the maximum gain is zero decibels. The relation between electric field strength and gain is presented in subsection 3.8.4. The true max gain and boresight gain has been stored in an excel file, so it is straightforward to correct the radiation patterns.

3.4.4 Geometry relative to RIMFAX and the rover

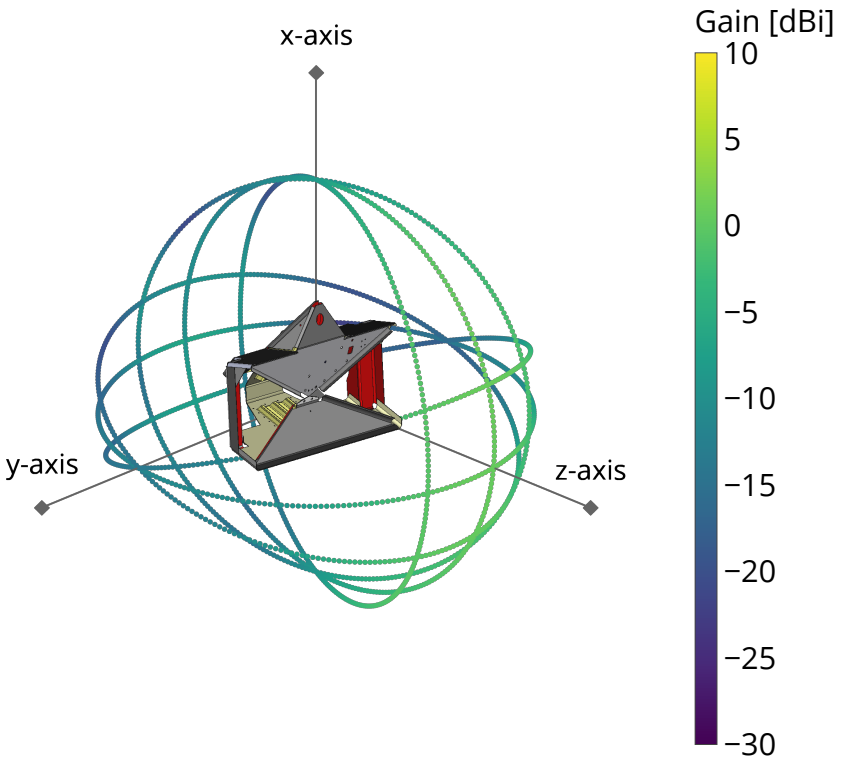

Figure 3.4: The color of each point represents the gain for that direction (yellow is higher). Each point is on the surface of a sphere with unit radius, to illustrate the spherical expansion of waves. At the center is an image of the antenna, with correct orientation relative to the coordinate system and the data.

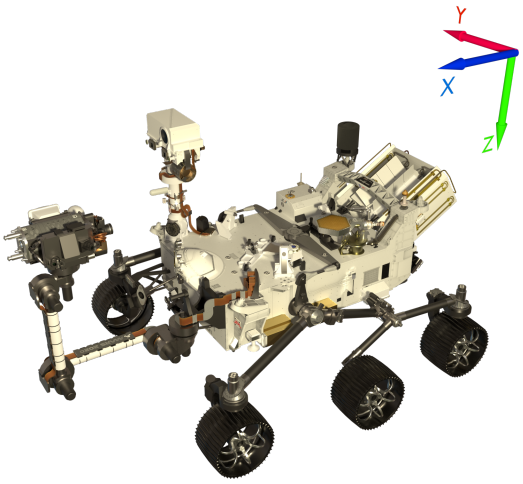

Figure 3.5: Cartesian coordinates relative to the rover. Rendered with blender, using the model that was created by *Brian Kumanchik, NASA/JPL-Caltech*.

3.5 Resampling the measurement data

Each cut of the radiation pattern has a different number of sample points (somewhere in the 300-500 region), and the angle coordinates of the end-points differ. To make plotting and debugging easier, and balance the least-squares algorithm to avoid one cut being more dominant than the others in the radiation pattern model (See subsection 3.8.7), we chose to resample all the cuts to the same angles.

Because of the high number of samples in the radiation pattern cuts, the errors introduced by resampling should be negligible in comparison with the errors introduced by SH- or SDFM-interpolation. Cubic interpolation is a natural choice, as it is already implemented in many libraries and the radiation patterns bear a closer resemblance to cubic polynomials than linear polynomials. The resampled measurements are represented as polar plots in Appendix A.

3.6 Transforming the radiation pattern

Before the measured data can be interpolated into a full 3D-pattern, we need to transform the coordinates from Fig. 3.3 into a single coordinate system that contains all the measurement points.

3.6.1 Cartesian coordinate representation

We start by representing the circles from Fig. 3.3 in Cartesian coordinates. We set the radius of the circles to 1. By studying the case of the XZ-plane we get:

$$x = sin(\beta)$$

$$y = sin(\alpha)cos(\beta)$$

$$z = cos(\alpha)cos(\beta)$$

under the constraint $|\alpha| < \frac{\pi}{2}$. In the YZ-plane we get:

$$x = sin(\beta)cos(\alpha)$$

$$y = sin(\alpha)$$

$$z = cos(\alpha)cos(\beta)$$

under the constraint $|\beta| < \frac{\pi}{2}$.

3.6.2 ISO spherical coordinates

We also need a representation in ISO-standard spherical coordinates, as it is required for the SH-interpolation from Section 3.8.

$$\begin{aligned} \phi_{iso} &= arctan\left(\frac{y}{x}\right) \\ \theta_{iso} &= arccos\left(\frac{z}{r}\right) \\ r &= 1 \end{aligned} \tag{3.3}$$

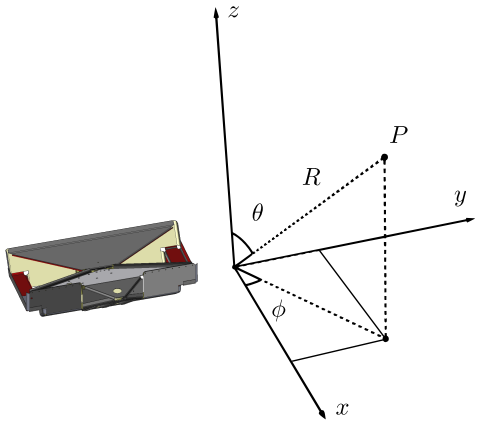

Figure 3.6: ISO spherical coordinates

3.6.3 Azimuth-Elevation spherical coordinates

A commonly used coordinate system for antenna radiation patterns is Azimuth-Elevation spherical coordinates. The transform from Cartesian coordinates is:

$$\begin{aligned} \theta_{azel} &= arcsin(x) \\ \phi_{azel} &= atan2(y,z) \\ r &= 1 \end{aligned}$$

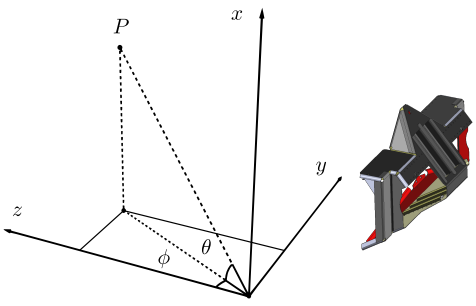

Figure 3.7: Azimuth-Elevation spherical coordinates.

3.7 The necessity of interpolation

The tests performed by Comrod produced gain-estimates for a set of discretized directions and frequencies. Discretization is inevitable, both in simulation and real-world measurements. The problem is that some mathematical operations are only defined for analytical functions. Integration is an example of this, which we need in order to evaluate the mean in Eq. 2.5.

The methods that estimate the integral of a discrete function, always applies some form of curve- or surface-fitting. The Riemann-sum uses step-functions, while the trapezoidal rule assumes a piece-wise linear behavior (See Fig. 3.8a and 3.8b). This means that the discrete version of integration always makes assumptions about how the function behaves between known points.

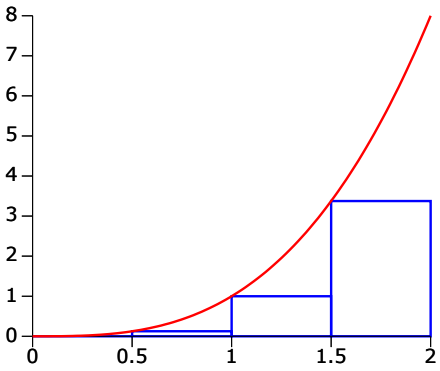

(a) Riemann integration. *Created by: Qef.*

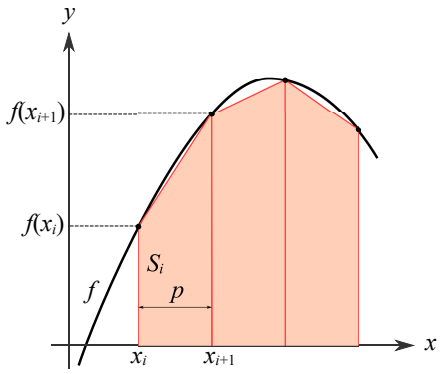

(b) Trapezoidal rule. *Created by: Cdang* (CC BY-SA 3.0).

Figure 3.8: Two methods of discrete integration.

We have chosen to use Spherical Harmonic functions to interpolate the radiation pattern spatially, while a Spectral Domain Fitting Model has been used for frequency interpolation. A discussion of two other spatial interpolation methods can be found in Section D.2.

3.8 Spherical Harmonic interpolation

3.8.1 Overview

The method we chose to perform spatial interpolation of the radiation pattern of RIMFAX was inspired by [16], and then implemented based on the work in [17]. The idea behind it is to use spherical waves as a basis for surface-fitting the measured electric field. We start with a brief overview of Maxwell's equations, as this is the theoretical origin of the method.

3.8.2 Maxwells equations

$$\nabla \times H = \frac{\partial D}{\partial t} + J \tag{3.4}$$

$$\nabla \times E = -\frac{\partial B}{\partial t} \tag{3.5}$$

$$\nabla \cdot D = \rho_v \tag{3.6}$$

$$\nabla \cdot B = 0 \tag{3.7}$$

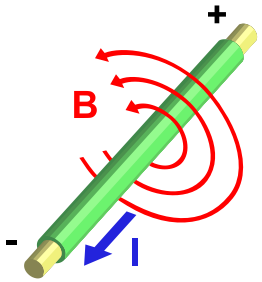

(a) The magnetic field curls around the current vector. *Created by: Stannered.* (CC BY-SA 3.0)

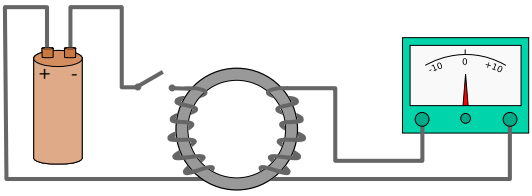

(b) Faraday's ring experiment. *Created by: Eviatar Bach.* (CC0 1.0)

3.8.3 The wave equation

Before we get to the spherical waves, we introduce the wave equation. This equation describes the behavior of electromagnetism in a vacuum, and can easily be derived from Maxwell's equations (see Section D.1). We will use the scalar version because we just want to model gain, and not the electric field vectors.

$$\nabla^2 E = \epsilon\mu \frac{\partial^2 E}{\partial t^2} \tag{3.8}$$

3.8.4 Solving the equation for spherical coordinates

According to [18, p. 427] the general solution to this equation, for spherical coordinates, is:

$$E(\vec{r},\omega) = \sum_{lm}\left[A_{lm}^{(1)}h_l^{(1)}(kr) + A_{lm}^{(2)}h_l^{(2)}(kr)\right]Y_{lm}(\theta,\phi) \tag{3.9}$$

where k is the wave number, and r,θ,ϕ are ISO-standard spherical coordinates. We observe in Eq. 3.9 that the angular dependence is separable from the radial dependence. Because of this we can simply set the radius and wave-number to constants, and reduce the bracketed expression to a coefficient.

$$\left[A_{lm}^{(1)}h_l^{(1)}(kr) + A_{lm}^{(2)}h_l^{(2)}(kr)\right] = c_{lm}$$

Under the constraints from the derivation of the wave-equation, we can expand any scalar electric field onto a basis of spherical harmonics. This is quite similar to how the Fourier series solves the heat equation. We split the sum to obtain this final representation of the solution:

$$E(\theta,\phi) = \sum_{l=0}^{\infty}\sum_{m=-l}^{l} c_{lm}Y_l^m(\theta,\phi) \tag{3.10}$$

To interpolate the electric field we just need to find the right coefficients c_{lm} that matches our measured electric field. The spherical harmonic functions are defined as,

$$Y_l^m(\theta,\phi) = \sqrt{\frac{(2l+1)(l-m)!}{4\pi(l+m)!}}P_l^m(cos\theta)e^{im\phi} \tag{3.11}$$

where P_l^m are the associated Legendre polynomials. It is a simple process to get the gain pattern when we have the electric field radiation pattern. Because a superposition of plane waves also form a general solution to the wave equation [19], we can decompose the wave front into plane waves. The radiation intensity of a particular direction is then the magnitude of the time-averaged Poynting vector [18, p. 298]:

$$U(\theta,\phi) = \langle S(\theta,\phi)\rangle = \frac{1}{2\eta}|E(\theta,\phi)|^2 \tag{3.12}$$

By using Eq. 3.1 and Eq. 3.2 we see that the electric field strength is the only directionally dependent factor in gain. We just need to find the right factor G_{adjust} so that the boresight gain is correct. Because we know the true gain at boresight, this is trivial exercise.

$$G(\theta,\phi) = |E(\theta,\phi)|^2 \cdot G_{adjust}$$

3.8.5 Truncating the series

If we are to find the spherical harmonic coefficients numerically, the series in Eq. 3.10 needs a truncation order L. The recommended truncation index is limited by the amount of measurement points, and their geometry.

Consider a radiation pattern that we have measured along n_ϕ number of circles orthogonal to the ϕ-plane. Each circle is defined for the ISO-spherical coordinates,

$$\phi \in \{\phi_i, \phi_i + \pi\} \quad \theta \in [0, \pi]$$

where $\phi_i \in [0, \pi]$ is the orientation of each circle as seen in Fig. 3.10.

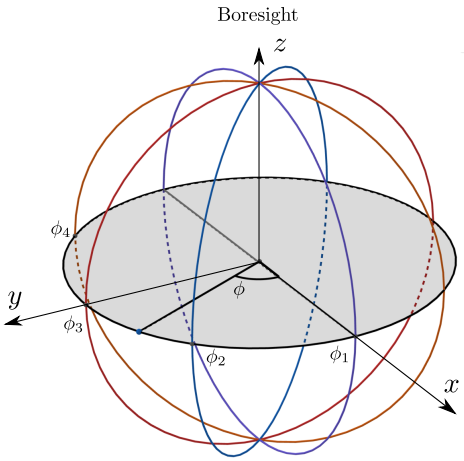

Figure 3.10: A radiation pattern measured at $n_\phi = 4$ cuts orthogonal to the ϕ-plane.

For this measurement geometry [20] suggests the optimal truncation index is (ignoring noise-induced error):

$$L_{opt,exact} = min\{n_\phi, n_\theta, \sqrt{M+1} - 1\} \tag{3.13}$$

n_θ represents the number of measurements in each constant-ϕ cut, while M is the total number of measurement points. Using only the E- and H-plane orientations, we then get $L_{opt,exact} = 2$. This should be a rough estimate of what truncation order we can expect to work. By adding the Ep20-, Em20-, Hp20- and Hm20-planes we will probably be able to go for a higher truncation order.

3.8.6 Expanding the series as a matrix equation

A method for decomposing a sparse data-set into spherical harmonics is detailed in [17]. This method expresses Eq. 3.10, for M measurement points, as a set of linear equations:

$$\boldsymbol{y} = \boldsymbol{A}\boldsymbol{x} \tag{3.14}$$

where the measurements of the electric far field are

$$\boldsymbol{y} = \begin{bmatrix} E(\theta_0, \phi_0) \\ E(\theta_1, \phi_1) \\ \vdots \\ E(\theta_M, \phi_M) \end{bmatrix} \tag{3.15}$$

Furthermore, $\boldsymbol{x}$ is defined as:

$$\boldsymbol{x} = \begin{bmatrix} k_0, & k_1, & \cdots, & k_L \end{bmatrix}^T \tag{3.16}$$

with,

$$k_l = \begin{bmatrix} c_l^{-l}, & \cdots, & c_l^0, & \cdots, & c_l^l \end{bmatrix} \tag{3.17}$$

Finally, $\boldsymbol{A}$ is defined as,

$$\boldsymbol{A} = \begin{bmatrix} \boldsymbol{Y}(0;\theta_0,\phi_0) & \boldsymbol{Y}(1;\theta_0,\phi_0) & \cdots & \boldsymbol{Y}(L;\theta_0,\phi_0) \\ \boldsymbol{Y}(0;\theta_1,\phi_1) & \boldsymbol{Y}(1;\theta_1,\phi_1) & \cdots & \boldsymbol{Y}(L;\theta_1,\phi_1) \\ \vdots & \vdots & \vdots & \vdots \\ \boldsymbol{Y}(0;\theta_M,\phi_M) & \boldsymbol{Y}(1;\theta_M,\phi_M) & \cdots & \boldsymbol{Y}(L;\theta_M,\phi_M) \end{bmatrix} \tag{3.18}$$

where $\boldsymbol{Y}$ is a row-vector:

$$\boldsymbol{Y}(l;\theta,\phi) = \begin{bmatrix} Y_l^{-l}(\theta,\phi), & \cdots, & Y_l^0(\theta,\phi), & \cdots, & Y_l^l(\theta,\phi) \end{bmatrix} \tag{3.19}$$

3.8.7 Least Squares Solver

We want to solve Eq. 3.14. As discussed in subsection 3.8.5, the optimal truncation order probably is slightly higher than $L = 2$ (not taking errors into account). The number of columns in $\boldsymbol{A}$ is $L^2 = 4$, while the number of rows is $N_{rows} \approx 300 \cdot N_{cuts} = 600$. Because of the higher number of rows, the system is over-determined and we will not get an "exact" solution to the equation. We can find approximations to the coefficients by projecting our measurement data onto the range of $\boldsymbol{A}$. In simpler terms, we ignore the behavior of the data that does not coincide with the spherical harmonic functions. A least squares solver is an algorithm that does this. It finds the $\tilde{x}$-vector that minimizes the expression,

$$||\boldsymbol{y} - \boldsymbol{A}\tilde{\boldsymbol{x}}||_2 \tag{3.20}$$

where $||u||_2$ is the euclidean 2-norm, and $\boldsymbol{y}$ and $\boldsymbol{A}$ are known. Eq. 3.18 and Eq. 3.15 clearly shows us that these can be calculated purely from the measured scalar electric field and the spherical harmonic functions.

An estimator that minimizes this norm is the Ordinary least squares (OLS) estimator,

$$\tilde{x} = (A^T A)^{-1} A^T y \tag{3.21}$$

We have from [21]: 'The Gauss–Markov theorem states that the OLS estimator has the lowest sampling variance within the class of linear unbiased estimators, if the errors in the linear regression model are

uncorrelated, have equal variances and expectation value of zero.' In essence this means that by treating the measured electric field strength as a probability distribution,

$$E(\theta_i, \phi_i) = E_{antenna}(\theta_i, \phi_i) + E_{noise}(\mu = 0, \sigma) \tag{3.22}$$

OLS will find the minimum variance estimate with respect to the deterministic behavior of the antenna. Using more data for estimating the SH-coefficients should thus improve our model.

3.8.8 Deterministic error sources

Eq. 3.22 only considers the kind of errors that arise when the experiment is performed "perfectly". If θ_i, ϕ_i are not the only parameters that change, we may get deterministic errors in the measurements. For example, the distance between the antennas may slightly change for each measurement. Furthermore, there may be objects that cause reflections which interfere on the receiver antenna. The range deviation has been partly corrected for in our model, as each cut of the radiation pattern has been normalized to boresight. However, the range deviation within each cut has not been corrected.

3.8.9 Python implementation

Eq. 3.14 was solved using a least-squares solver in Python. A function to reconstruct the radiation pattern, for any θ, ϕ-grid, using the spherical harmonic coefficients, has also been written. One implementation in cupy (CUDA-accelerated numpy) showed up to 3x perfomance increase over numpy for reconstructing the radiation pattern (See Table C.1).

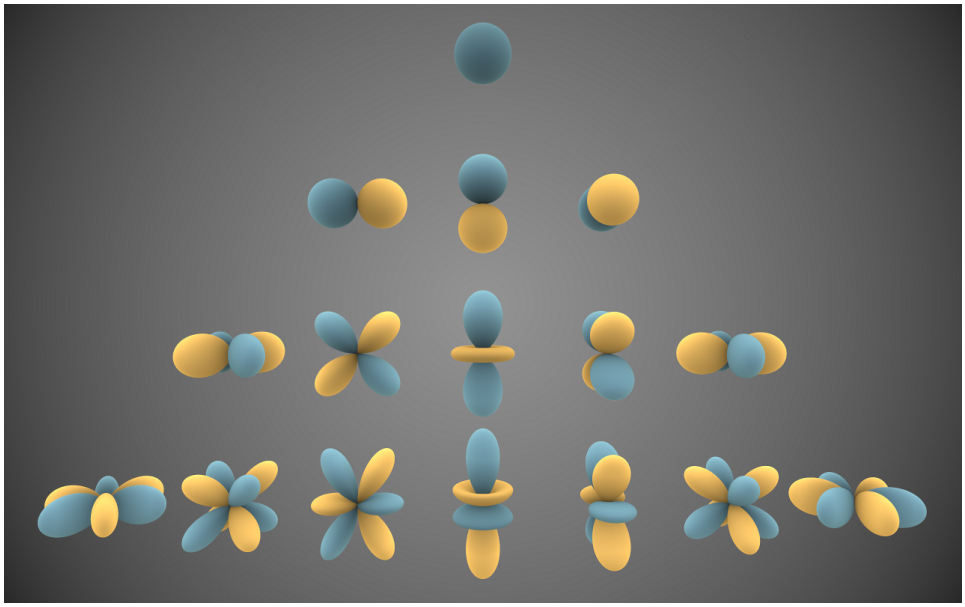

Figure 3.11: "Spherical Harmonics" by *Inigo.quilez* is licenced under CC BY-SA 3.0. The function Y_l^m is at row l and column m.

3.9 Spectral interpolation

3.9.1 Overview

The method we have chosen to interpolate the frequency behavior of the antenna is based on the Padé rational function:

$$F(s) = \frac{N_0 + N_1 s + N_2 s^2 + \cdots + N_n s^n}{D_0 + D_1 s + D_2 s^2 + \cdots + D_{d-1} s^{d-1} + s^d} \tag{3.23}$$

N_i, D_j are the filter coefficients, and $s = j\omega$ is the complex frequency. We call Eq. 3.23 a Spectral Domain Fitting Model (SDFM).

According to [22], pole-series arise as wave-equation solutions in EM and similar physical phenomena. However, the objects measured are never purely resonant, but are partly excited by sources. While this can theoretically be eliminated in the time-domain by measuring at "late-time", when the object is no longer excited by an incident field, the frequency domain cannot be so clearly separated into driven or source-free behavior. Thus, the numerator part of the function is added to approximate the effect of the non-pole term.

The rest of this chapter will present some of the research that has been done on SDFM. Then the implementation will be outlined, along with some considerations made when applying this method to the measurements data. Finally, there will be a discussion of the possible errors that may arise.

3.9.2 Research on SDFM

E. K. Miller [23] has shown that the input impedance of antennas can be interpolated with the function from Eq. 3.23.

In [24] this method has been applied at the electric field strength of the antenna. It has been used to do simultaneous spatial and frequency interpolation of radiation patterns by curve-fitting the Padé rational function in each spatial direction. The method then interpolates the filter coefficients spatially with binomial functions.

This method was further improved in [16] by separating the spatial and frequency interpolation, such that MBPE methods can be used in both domains. Multiple rational filters were used, each constructed from 3 or 4 sampling frequencies. In one case 7 sampling frequencies were used, with three 3-coefficient filters. The first filter used the first three samples, while the second filter used the middle three samples, etc. Each filter was then defined within the range of the frequency samples used to create it.

3.9.3 Why this could benefit RIMFAX

As discussed in subsection 3.9.2, SDFM interpolation can be used to interpolate the electric field in each direction. This is the type of frequency

interpolation we find most interesting, as it is a theory-based interpolation method that could further generalize the radiation pattern model. If successful, the gain of the antenna could be estimated in every possible direction and at every frequency within the measured frequency-range. Because RIMFAX is an FMCW radar it makes sense to extend the Fresnel reflection and backscattering models in chapter 2 for frequency-modulated signals. This would require that the mean is evaluated for direction and time/frequency.

3.9.4 Estimating the filter coefficients numerically

In every spatial direction the electric field, $F(s)$, has been sampled at N_f different frequencies:

$$s \in \left[s_0, s_1, \cdots, s_{Nf}\right]$$

The coefficients in Eq. 3.23 can be calculated by putting measurements from a particular direction in a set of linear equations,

$$\boldsymbol{A}\boldsymbol{x} = \boldsymbol{b} \tag{3.24}$$

where

$$\boldsymbol{b} = \begin{bmatrix} F(s_1)s_1^d \\ F(s_2)s_2^d \\ \vdots \\ F(s_{Nf})s_{Nf}^d \end{bmatrix}$$

$$\boldsymbol{x} = \begin{bmatrix} N_0 \\ N_1 \\ \vdots \\ N_n \\ D_0 \\ D_1 \\ \vdots \\ D_{d-1} \end{bmatrix}$$

$$\boldsymbol{A} = \begin{bmatrix} 1 & s_1 & \dots & s_1^n & -F(s_1) & -F(s_1)s_1 & \dots & -F(s_1)s_1^{d-1} \\ 1 & s_2 & \dots & s_2^n & -F(s_2) & -F(s_2)s_2 & \dots & -F(s_2)s_2^{d-1} \\ \vdots & \vdots & \vdots & \vdots & \vdots & \vdots & \vdots & \vdots \\ 1 & s_{Nf} & \dots & s_{Nf}^n & -F(s_{Nf}) & -F(s_{Nf})s_{Nf} & \dots & -F(s_{Nf})s_{Nf}^{d-1} \end{bmatrix}$$

3.9.5 Solving the equation

If the number of coefficients are fewer than the number of frequency samples, the equation can be solved by the OLS estimator discussed in subsection 3.8.4. A least squares solution was able to smooth noisy frequency domain data in [23], but a much higher number of frequency samples were used to estimate the filter coefficients (512 samples with BW of $\sim$ 1 GHz). This kind of spectral estimation is similar to spectral

factorization. Some experimentation with least-squares was done on the measured data of RIMFAX without success. Thus, we will try finding an exact solution, which requires $\boldsymbol{A}$ to be a square matrix. The number of filter coefficients are then constrained by the number of frequency samples N_f:

$$N_f = d + n + 1 \tag{3.25}$$

3.9.6 The method that has been implemented

The electric field measurements have been normalized to make the maximum magnitude of the radiation pattern cuts equal to 1 (See Appendix A). This was not a problem for the spatial interpolation in subsection 3.8.4, as the radiation efficiency appears as a directionally independent constant in the radiation pattern. The way we dealt with this problem in subsection 3.8.4 was to scale the interpolated radiation pattern such that the boresight gain was correct at each frequency. In this case it doesn't work because of the frequency dependence of radiation efficiency.

From Eq. 3.2 and Eq. 3.12, we see that the electric field is the only frequency dependent variable in antenna directivity. If we know what the antenna efficiency and gain is, we can calculate the magnitude of the electric field scaled by a frequency-independent constant. The phase of the electric field doesn't change when it is scaled, so we can get this directly from the scaled electric field. The electric field can then be expressed as,

$$E(j\omega) \cdot C = P(\omega)\sqrt{G(\omega)/\xi(\omega)} \tag{3.26}$$

where $P(\omega)$ is the phase of the electric field and C is a constant. A constant scaling doesn't change the pole-zero positions. Thus one could apply the same SDFM-interpolation of [24] on the right-hand side of Eq. 3.26. The gain is easily recovered by:

$$G_{interp}(\omega) = \xi(\omega)|E_{interp}(j\omega) \cdot C|^2 \tag{3.27}$$

In order to perform this interpolation we need to model the radiation efficiency. The best methods for estimating radiation efficiency require special measurement setups, such as the Wheeler cap, which was introduced in [1], or the waveguide around the antenna in [25]. According to [2, p. 83] it is possible to estimate the directivity when the antenna has a single mainlobe pointing in the z direction,

$$D \approx \frac{4\pi}{\beta_{xz}\beta_{yz}}$$

where β_{xz}, β_{yz} are the half-power beamwidths. However, [26] showed that this method had a high uncertainty varying between 15-28% for small patch antennas, while the Wheeler cap method gave an uncertainty of 2%. We also observe that our radiation pattern measurements, in Appendix A, do not have a single mainlobe at higher frequencies.

If the interpolated radiation pattern was accurate enough in all directions, it could also be used to estimate radiation efficiency, due to the fact that the mean of gain is equivalent to radiation efficiency. Before we had interpolated the radiation pattern, this was thought to be a viable option, however the results we got from this method were not realistic (see Table B.1).

Thus, as we cannot perform new measurement experiments, we have chosen to treat the radiation efficiency as constant in Eq. 3.26 and Eq. 3.27. If the difficulties related to accurate estimation of radiation efficiency had been known beforehand, another frequency interpolation method would probably have been selected. However, it might be reasonable to assume that the antenna efficiency is relatively unchanging with frequency compared to the electric field strength.

3.9.7 Deterministic error sources

As discussed in subsection 3.8.8, the distance between the antennas will probably not remain constant for all the measurements. Small changes in distance will presumably not have a big effect on the gain of the antenna. In some instances, we do still observe several decibels of difference between measurements in the same direction (see Fig. A.2e at 0°).

However, the biggest errors are likely to be found in the phase measurements of the electric field. In Table 3.2 we see large differences in the wavelengths between the frequencies used for RIMFAX. For instance, if the antenna is 10 cm out of position the electric field measurements at 1200 MHz will be shifted by a phase of 144°. At 150 MHz this distance would amount to a mere 18° of phase difference.

frequency [MHz]	150	500	1200
λ	2.0	0.60	0.25

Table 3.2: Table showing the wavelengths of different frequencies.

3.9.8 Noise-induced errors

The radiation patterns are constructed from noisy measurements, but as discussed in subsection 3.8.7, the spatial interpolation takes this into account when constructing the full radiation pattern model. Still, as long as the SH-interpolation isn't "perfect", there will be errors in the radiation pattern which propagate through the frequency interpolation. Also, the boresight gain measurements that were used to adjust the radiation pattern, varies between the E-plane and H-plane configuration (See Fig. 5.18).

Chapter 4

Characterizing the gate

4.1 Overview

4.1.1 FMCW radar

RIMFAX is a Frequency Modulated Continuous Wave (FMCW) radar, meaning it sends and receives signals continuously, and modulates the frequency of the transmitted signal. When a signal is received, it is mixed down, such that the Instantaneous Frequency (IF) can be measured. This frequency is used for range discrimination. When the radar has modulated the frequency across the whole specified bandwidth, we call this a "sweep". FFT can then be used to get the delay-response trace of the radar.

The sampling rate of the A/D converter is limited, so all ranges can not be detected at the same time. The signal that is used to demodulate the received signal can be delayed such that the IF corresponds to a different range [27]. The delay of the mixer signal is kept constant throughout the sweep.

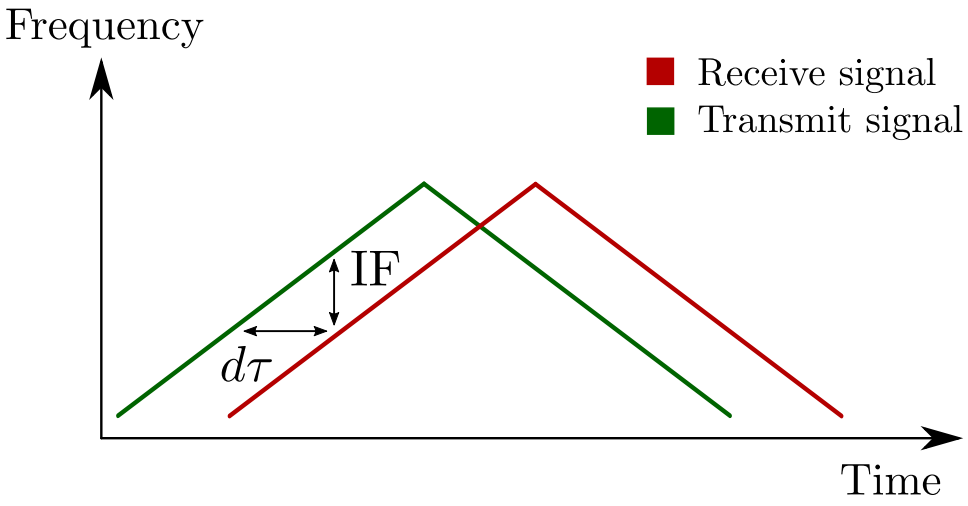

Figure 4.1: Linear Frequency Modulated Continuous Wave (LFMCW) radar for static targets. The IF corresponds to reflections with delay $d\tau$.

4.1.2 The gate

Between the signal generator and receiver is a gate, which switches access to the antenna periodically. This can remove the early strong reflections to better utilize the dynamic range of the system [28]. The switch (or gate) can be described mathematically as two rectangular periodic window functions, one for Tx and one for Rx.

Only a fraction of the signal energy passes through the two gates, depending on the range/IF of the reflections. When the received signal has been mixed down and Fourier-transformed this results in an amplitude change of the delay-response trace, which can be mathematically described as a convolution of the Tx- and Rx- gate windows [28].

$$g(t) = (g_{Tx} * g_{Rx})(t)$$

It is desirable to correct the received signal for the amplitude change $g(t)$, as this would give a more accurate image of the reflective properties of the ground. It is especially important for estimating the dielectric constant, as the power of the received signal is the deciding factor in the models from chapter 2.

The remaining part of this chapter is concerned with characterizing the gate-function $g(t)$ from measurements of the RIMFAX electronics. First, we describe the gate-configurations that have been used to obtain measurements. Then, an analysis of how the gate ideally operates is presented. Finally, the measurements are analyzed and a method to estimate the gate-function is described.

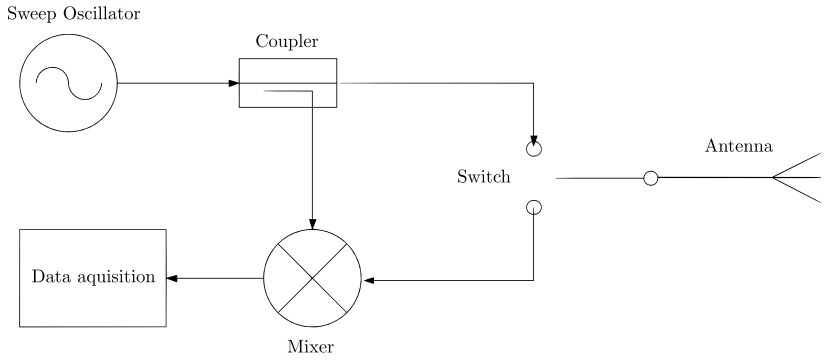

Figure 4.2: Gated FMCW radar. Source: [27]

4.2 Gate configuration

The gate of RIMFAX is constructed from three gates that separate the antenna from the transmitter and receiver (See Fig. 4.3). The gates can be configured to switch at different times, for example by delaying the Rx gate "On" after Tx has been set "Off". This is done to reduce ringing before the receiver comes on. Some of the modes used for our measurements have delayed the Rx "On" switch by 10 ns, and the antenna Rx-to-Tx switch by 10 ns (See Fig. 4.4). All the other modes have the gates configured to switch simultaneously. When we just use the word "gate", we refer to the three gates within the dashed rectangle in Fig. 4.3.

The switching rate of the entire system can be changed, but the modes we have chosen (see Table 4.1) have a gate-frequency of 12500 kHz. All the configurations uses the frequency band 150-1200 MHz, with a sweep time of $T_s = 3.125$ ms. This means the radar has a ramp-rate of $\alpha = 336$ MHz/s. We can also calculate the number of gate-cycles, $T_s \cdot F_{gate} \approx 39000$. The sampling rate, F_s, of the receiver is 97.656 kHz. The information from this section is based on [29], [30].

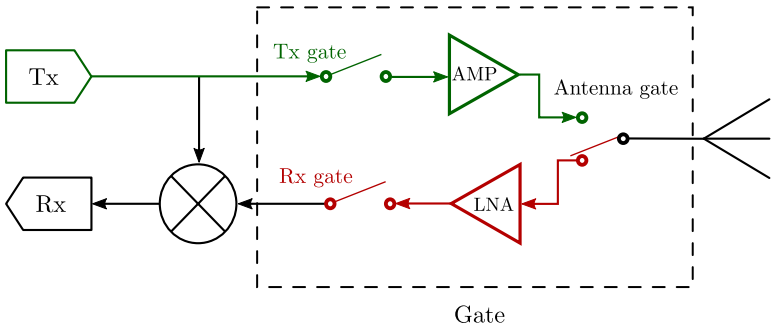

Figure 4.3: This diagram shows the actual gate-configuration of the radar. There are separate gates for the receiver and transmitter, in addition to an antenna gate. The Rx- and Tx-gates have attenuators but these are not illustrated. Source: [29]

CID #	F_{gate} [kHz]	τ_{rx2} [ns]	τ_{an1} [ns]	Tx att. [dB]	Rx att. [dB]
14	12500	0	0	31	11
16	12500	0	0	31	1
18	12500	0	0	22	0
24	12500	10	10	31	11

Table 4.1: Each row is signed with a different Configuration ID (CID), designating the mode of the gate and measurement setup. F_{gate} is the repetition frequency of the gate-function. τ_{rx2} delays the "off"-"on" switch of the Rx-gate. τ_{an1} delays the Rx-to-Tx switch of the antenna gate. The two last columns show the attenuation in Tx and Rx respectively. Source: [30]

4.3 How the gate ideally operates

4.3.1 The ideal gate-function

The following two figures show how the gate-configurations from Table 4.1 are supposed to work ideally. Fig. 4.4 shows the operation of the three gates with CID 24. Fig. 4.5 displays the ideal gate-functions for CID 24 (delayed) and CID 14, 16, 18 (simultaneous).

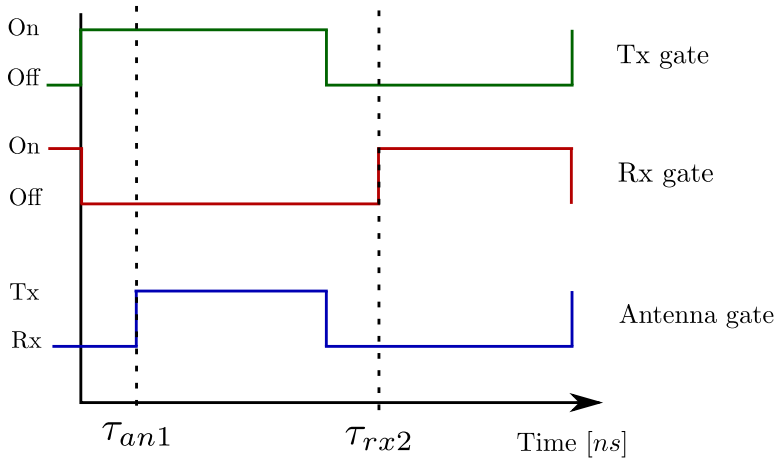

Figure 4.4: The Rx gate is delayed by 10 ns, relative to Tx "Off". The antenna gate is delayed by 10 ns relative to Tx "On".

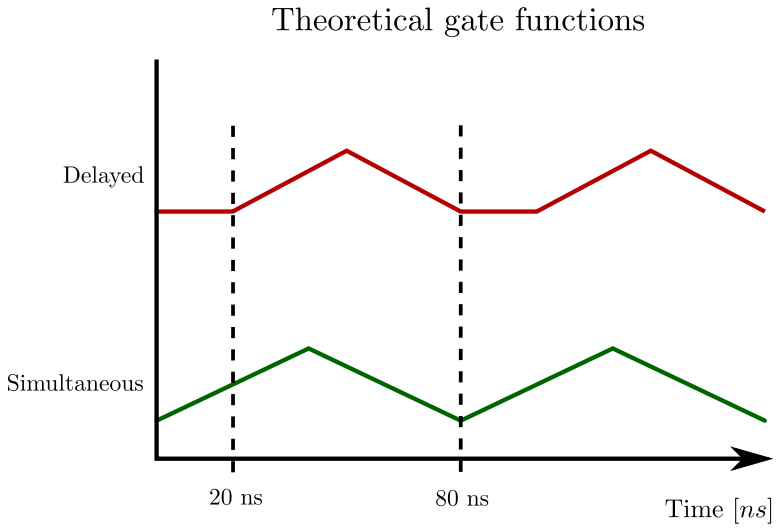

Figure 4.5: The lower graph shows the theoretical gate-function $g(t)$ when all the gates switch simultaneously. The upper graph displays the same function when the Rx-gate and antenna gate have been delayed.

4.3.2 The gate-windows in the frequency domain

For the moment we make the assumption that all the electronics works ideally. Under this assumption the gate can be modeled as a rectangular pulse wave, representing the Tx- and Rx- windows together. The pulse width, W, is determined by the range to the object observed, which corresponds to the IF. We call this pulse-wave the "total gating window".

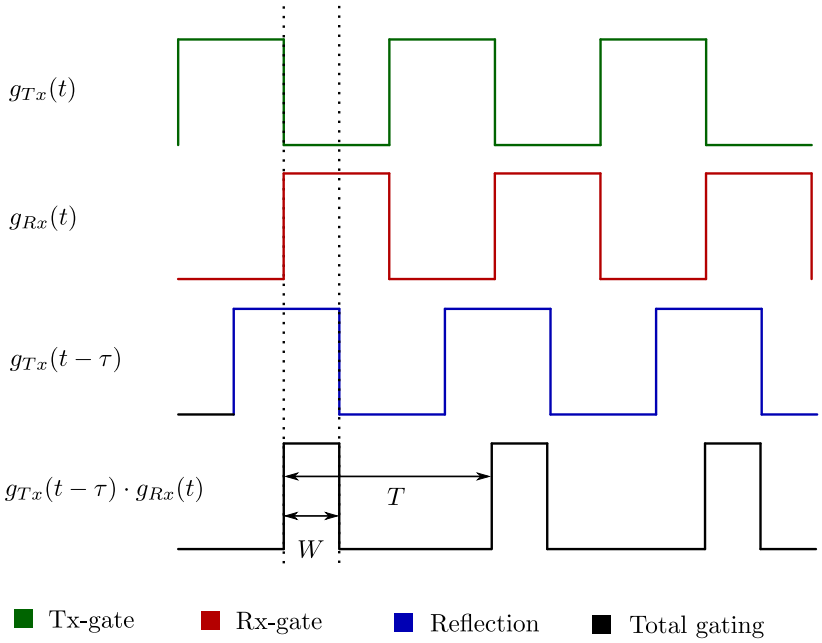

Figure 4.6: The total windowing function applied at a reflection at a certain range.

The limited sweep time can be seen as a rectangular window for the total gating window. The effects of the total gating window and the sweep window are best analyzed in the frequency domain. The fourier coefficients of the total gating window are,

$$a_n = 2\frac{W}{T} sinc(n\pi\frac{W}{T})$$

where $1/T = F_{gate}$ is the gate-frequency. The frequency of the harmonics that the gate produces are integer multiples of F_{gate}. Because $F_s << F_{gate}$, these harmonics cannot be detected unless the mixer signal is delayed.

In the frequency domain the Fourier coefficients of the gating window are convolved with the continuous sinc-function of the rectangular window of the sweep. Each harmonic has sidelobes which depend on the length of the sweep. The sidelobes of the harmonics do not have a big impact on the measured IF, because of the number of gate-cycles and the spectral distance between them. Other reflectors are a bigger issue and these are discussed in the next subsection.

4.3.3 A simulation of the gate

We have simulated the gate to analyze how reflectors behave in ideal circumstances. The total gating window from Fig. 4.6 has been used as a window on two sinusoids, which represent reflectors with different IF. The gate has been configured with the same gate-frequency and sweep time as the real modes, which are described in Section 4.2.

A window has then been applied before taking the FFT to get range-discrimination. As one would expect, the Chebyshev window produces a wider mainlobe and lower sidelobes. We also see that the reflectors from Fig. 4.7b distort each other due to sidelobe interference. For the measurements that will be discussed later, there are a discrete number of reflectors. For this application, the lower sidelobes of the Chebyshev window could provide more accurate measurements of reflection strength as long as the mainlobes do not interfere. The code for the simulation has been written in MATLAB and can be found in Appendix C.

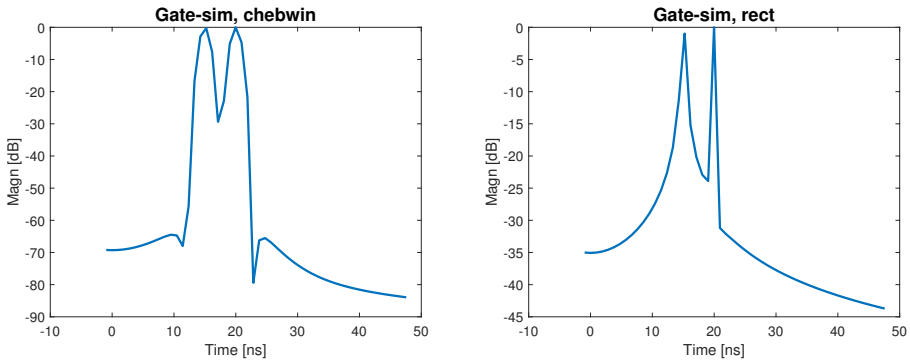

(a) Reflectors with Chebyshev-window. (b) Reflectors with Rect-window.

Figure 4.7: A simulation of two identical reflectors, 5 ns apart, with the same pulse-width. The number of gate-cycles were the same as all the configurations in Table 4.1. The gate-function which has been used is a square-wave for both of the reflectors. Note that in reality the pulse-waves of the reflectors would have different widths, but this would only increase the sidelobe influence on the weaker reflection.

4.4 Measurements of the gate

4.4.1 A description of the measurements

The Norwegian Defence Research Establishment (FFI) have made measurement in order to characterize the RIMFAX electronic box. They generated radar traces with the Engineering Qualification Model (EQM) of the electronic box connected to a network of cables, replacing the antenna in Fig. 4.2. These cables were shorted to ground at the ends, so they appear as reflectors in the time-domain. This setup is illustrated in Fig. 4.8a. We refer to the measurements made in this setup as the "gated signal".

FFI also measured S_{11} of the cable network with a Vector Network Analyzer (VNA). When the data is transformed to the time-domain, we get the impulse response of the cable reflectors. This setup is illustrated in Fig. 4.8b. We will refer to the signal measured in this setup as the "direct signal".

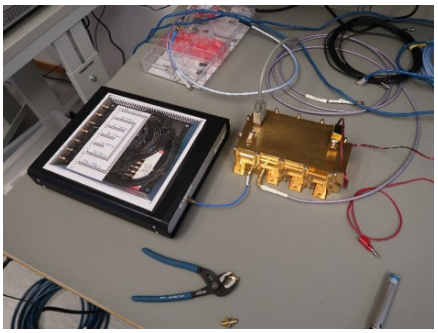

(a) Measurements done with the EQM electronic box connected to the reflectors.

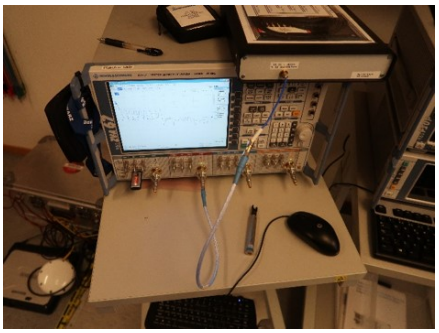

(b) Measurements done with the reflectors connected to the VNA.

Figure 4.8: Measurement setup

The cable that connects the EQM to the cable network in Fig. 4.8a was then swapped for a longer cable. This delayed the reflections, such that both the rise and fall of the gate-function could be measured. The cable was also swapped in the measurement setup from Fig. 4.8b. Four different cable lengths were used.

4.4.2 Analyzing the measurement setup

All the cables used in the measurement can be seen as transmission lines, with a certain characteristic impedance. If a short impulse is sent through the coaxial cable, we can model the time-domain response with a planar wave. This wave will propagate through the cable until the characteristic impedance changes, such as at a connector, or at a ground interface. A wave will then reflect, with an amplitude which depends on the impedance of the two mediums.

Because the cables are of different lengths but have the same character-

istic impedance, the reflections will return at different times through the receiver. There might be other impedance mismatches in the circuit, which are different in the two setups. For example, we might have stronger S_{22} on the antenna gate than we have on the VNA.

To minimize these other reflections, we will extract only the peaks of the cable reflections from the direct signal and take the corresponding ones from the gated signal. To remove the effects of the cable network, the direct signal peaks are subtracted. The other reflections are irrelevant as long as they do not interfere with the peaks of the shorted cable reflections. This is because the estimated gate-function will be normalized, such that only the relative reflective properties of the shorted cables matter.

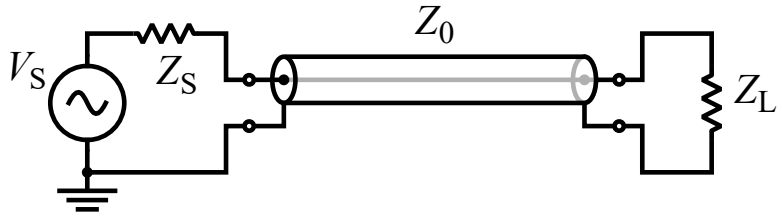

Figure 4.9: Coaxial cable. If the end is shorted, $Z_L = 0$, there is an impedance mismatch and a reflection will occur. Created by: *Omegatron* (CC BY-SA 3.0).

4.4.3 Signal processing of the measured data

This subsection describes the DSP algorithm used to estimate the gate-function.

The direct signal is stored as a complex signal, while the gated signal only contains the real part of the original signal. Because of this, the real part of the direct signal is extracted such that both signals are processed the same way. Then Chebyshev windows are applied on both functions to reduce sidelobes, as we discussed in subsection 4.3.3.

IFFT is performed on the positive-frequency direct signal in order to obtain the envelope in the time-domain. The same is done for the positive-time gated signal to get the envelope of the delay-response trace. The positive-time samples are extracted, and a time-shift is applied on the gated signal, in order to align the peaks of the reflectors. The peaks are found in the direct signal and the corresponding peaks are extracted from the gated signal. The decibel values of the direct signal peaks are subtracted from the gated signal peaks.

The result is a sampled gate-function, with a sample rate corresponding to the physical distance between the reflectors. A flowchart of the DSP-algorithm is displayed in Fig. 4.10.

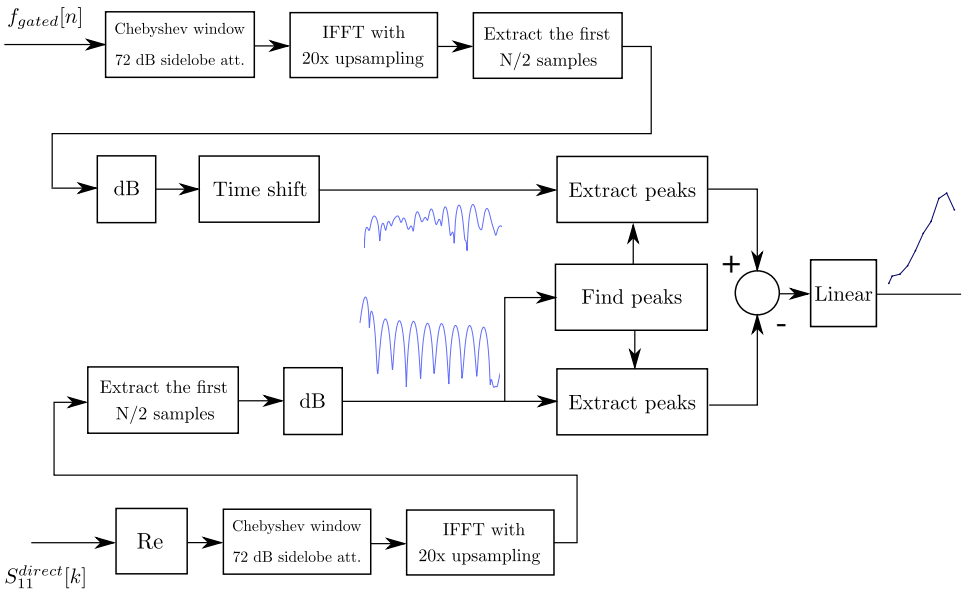

Figure 4.10: DSP flowchart of the gate-function estimator.

Chapter 5

Results

5.1 Spherical Harmonic interpolation

5.1.1 Chart choices

We have decided to use 3 types of chart to display the model. The first is a polar plot that compares the input data to the model's predictions (See Fig. 5.4). The second is a 3D-plot of the radiation pattern, that maps each direction to its spherical coordinates, with the radial axis representing gain. The gain is also mapped onto a colorbar (See Fig. 5.2). Finally, we have chosen to represent our model in Azimuth-Elevation coordinates, restricted to $\pm 90^{\circ}$ on both axes. This is displayed as an image, with the gain mapped to a colorbar (See Fig. 5.3).

The first chart type was selected because it makes it easy to evaluate to which degree the SH-functions can describe the measured data. The second was selected because its geometry bears a close relationship to how the antenna radiates waves in the real world. The third type gives a more precise image of how the model predicts radiation in the forward direction. We will also use the charts from Appendix A to understand the important spatial/frequency features of the real radiation pattern.

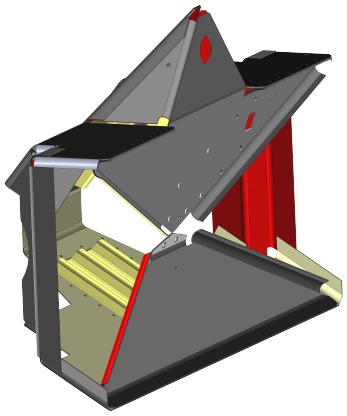

Figure 5.1: The antenna orientation of the following 3D-plots.

5.1.2 Parameter choices

In Fig. D.2 we see that there are measurements for 21 unique frequencies. For a single frequency and truncation order, we want to display 8 charts, spanning two pages. If we were to display these charts for all the frequencies, we would end up with 42 pages at a single truncation order. Because of this we have limited ourselves to three frequencies. At 150 MHz and 500 MHz the measured data has a low-order behavior. Gain changes smoothly in the spatial domain, which should make it easier for the low-order SH-functions to approximate the pattern. At 1130 MHz the radiation pattern has a higher order behavior. There are more lobes and dips in the pattern, and the patterns change radically for different antenna orientations (See E, Ep20 and Em20 in Fig. A.4, compared to Fig. A.3). We have also chosen to use three different truncation orders at 500 MHz; 2, 3 and 5. This was done to illustrate the convergence of the interpolation to the measurement data and to show the effects of the higher-order functions in the full radiation pattern.

5.1.3 The results

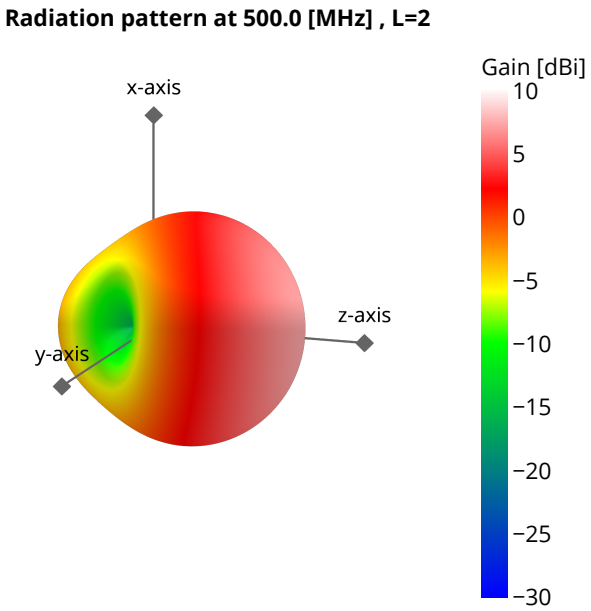

Figure 5.2: Antenna radiation pattern model, interpolated using spherical harmonics at order $L = 2$. The radius corresponds to gain [dB], with -30 dB representing zero radius.

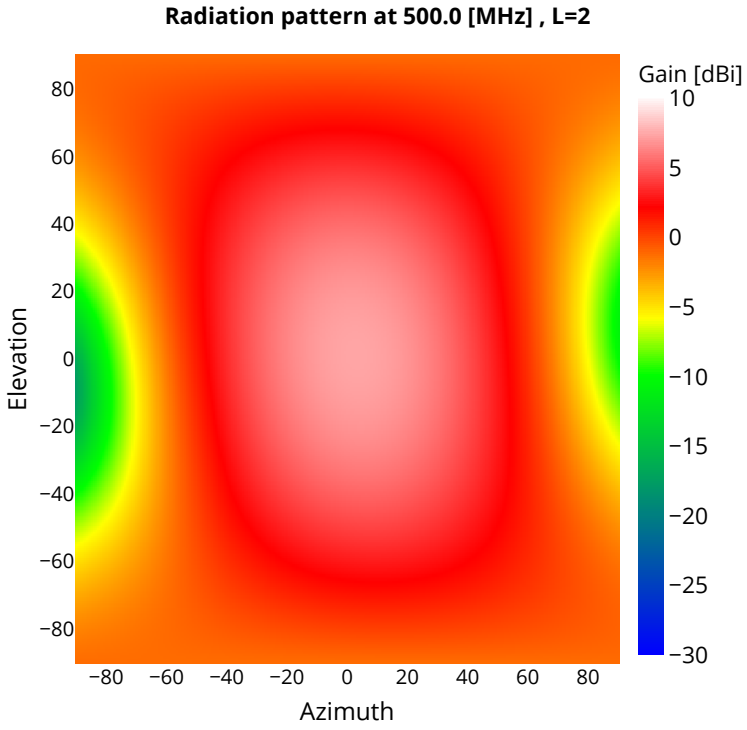

Figure 5.3: Antenna radiation pattern model in azimuth and elevation coordinates, interpolated using spherical harmonics at order $L = 2$.

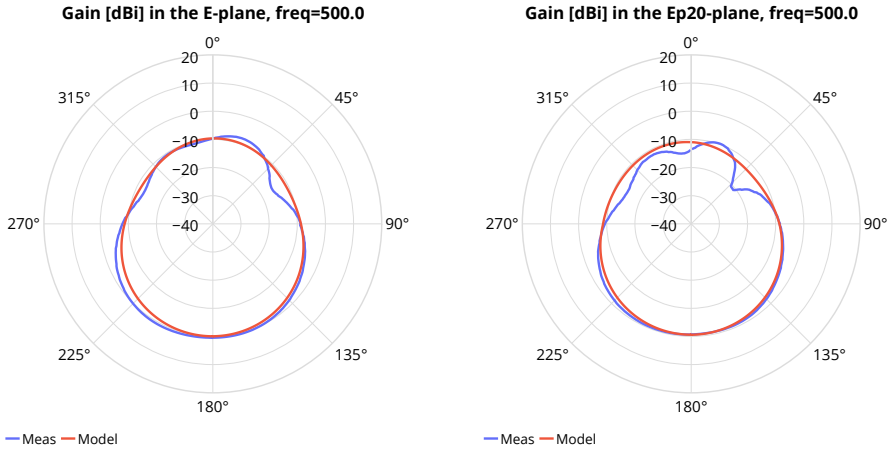

(a)

(b)

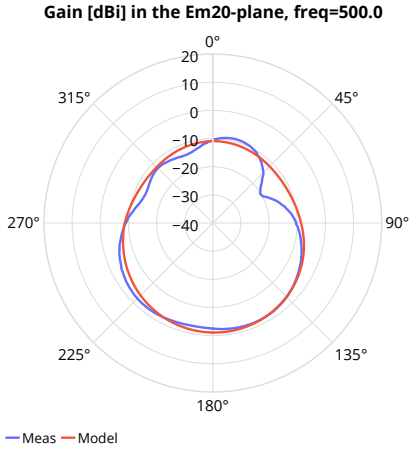

(c)

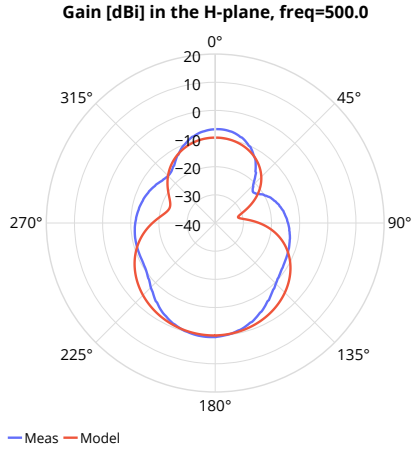

(d)

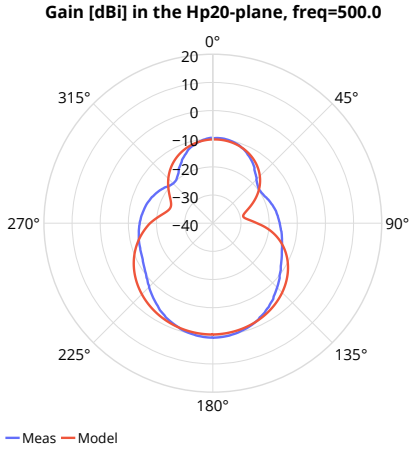

(e)

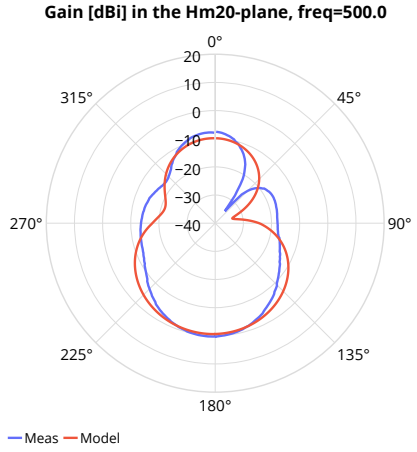

(f)

Figure 5.4: These plots display comparisons between the spherical harmonic model and the input data, at 500 MHz. The order of the model is $L = 2$. Each subfigure charts the gain for a different plane.

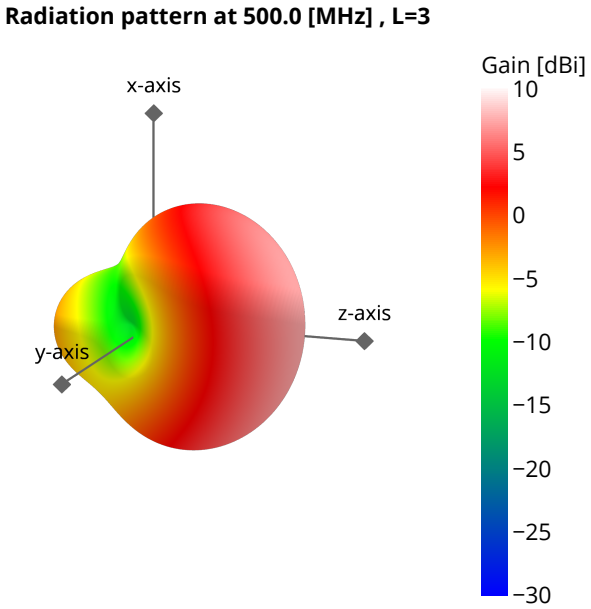

Figure 5.5: Antenna radiation pattern model, interpolated using spherical harmonics at order $L = 3$. The radius corresponds to gain [dB], with -30 dB representing zero radius.

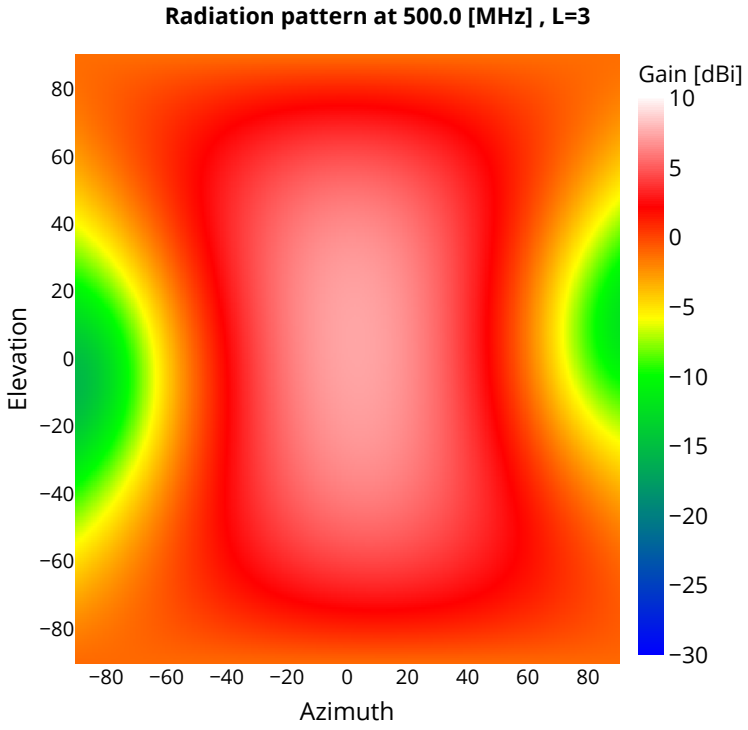

Figure 5.6: Antenna radiation pattern model in azimuth and elevation coordinates, interpolated using spherical harmonics at order $L = 3$.

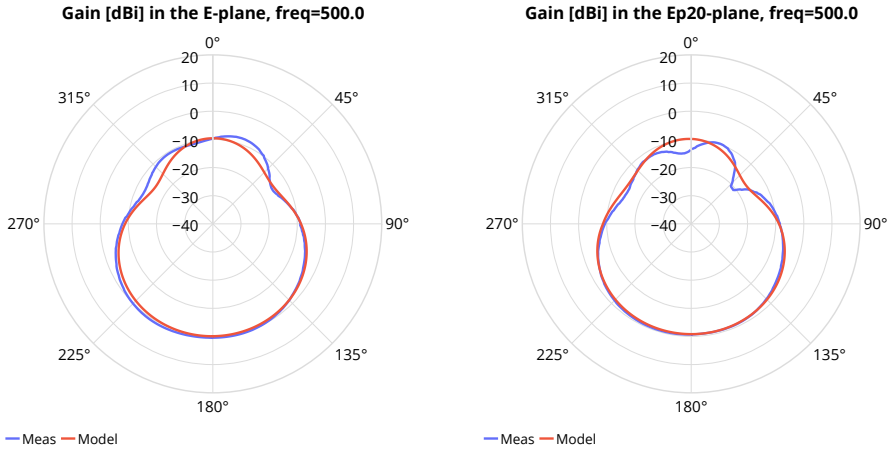

(a)

(b)

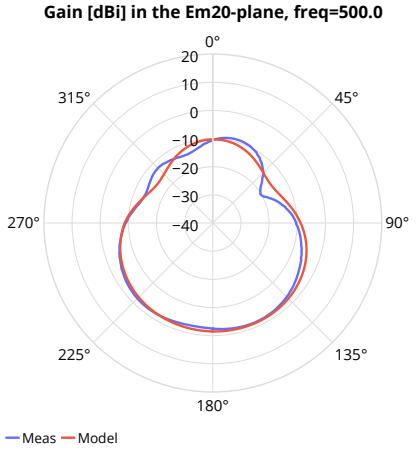

(c)

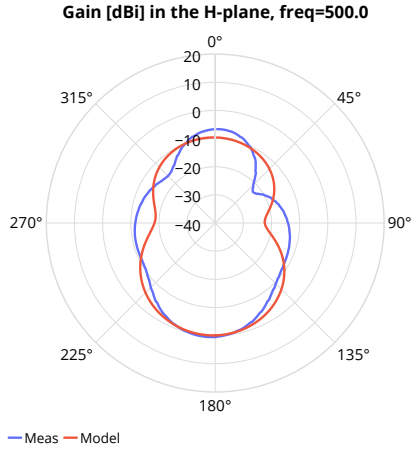

(d)

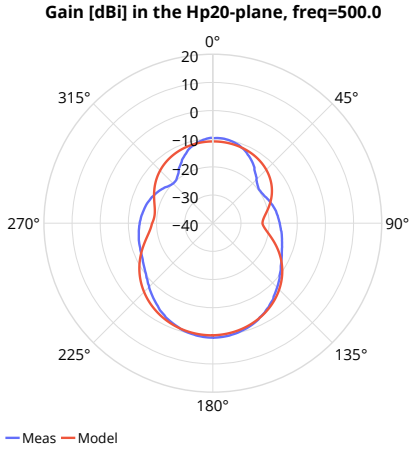

(e)

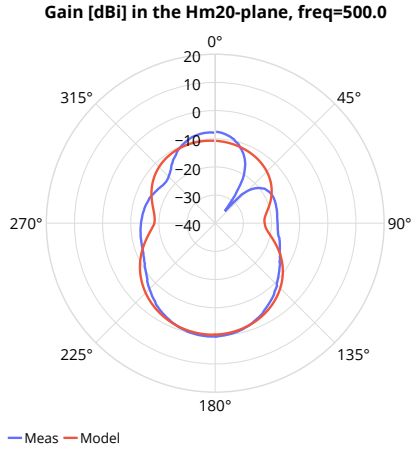

(f)

Figure 5.7: These plots display comparisons between the spherical harmonic model and the input data, at 500 MHz. The order of the model is $L = 3$. Each subfigure charts the gain for a different plane.

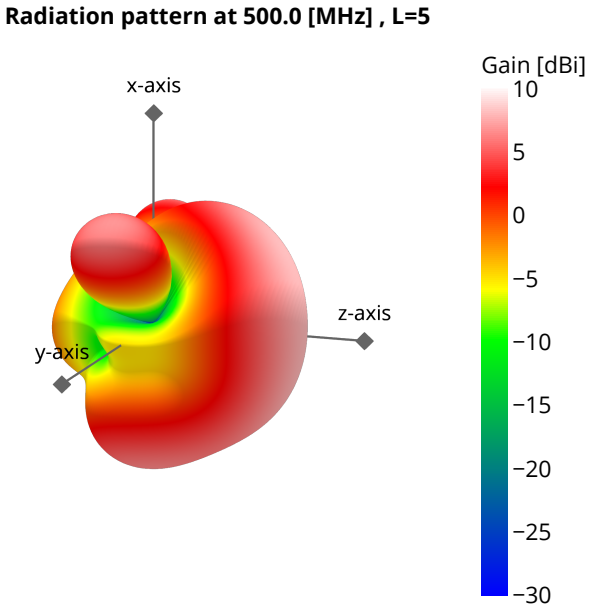

Figure 5.8: Antenna radiation pattern model, interpolated using spherical harmonics at order $L = 5$. The radius corresponds to gain [dB], with -30 dB representing zero radius.

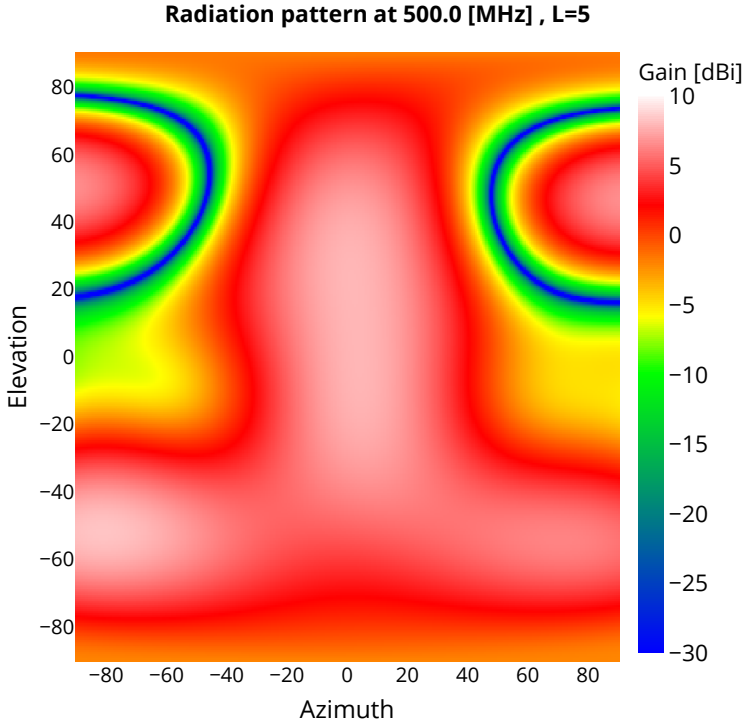

Figure 5.9: Antenna radiation pattern model in azimuth and elevation coordinates, interpolated using spherical harmonics at order $L = 5$.

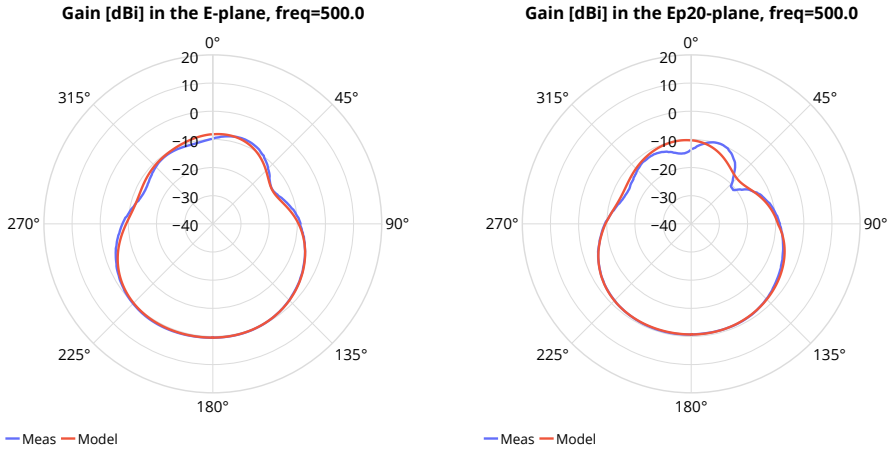

(a)

(b)

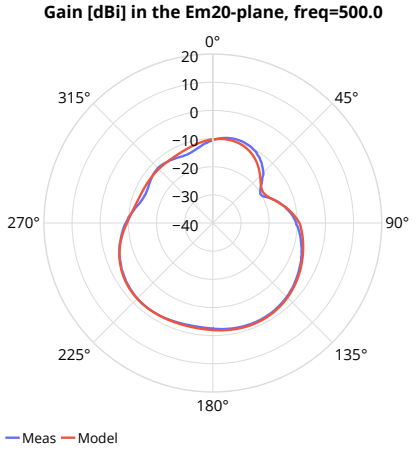

(c)

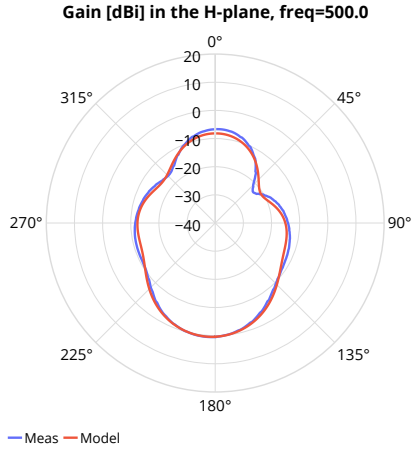

(d)

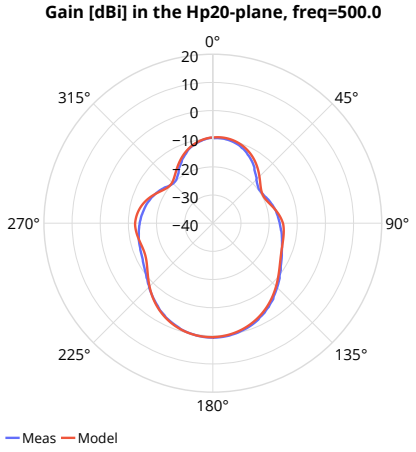

(e)

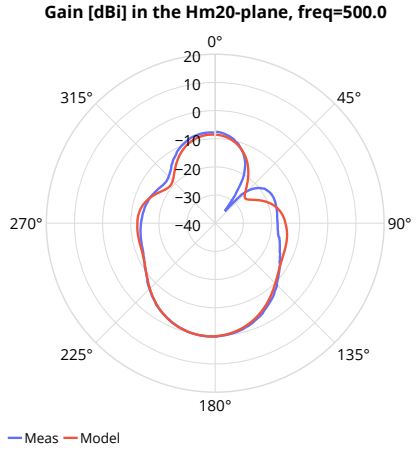

(f)

Figure 5.10: These plots display comparisons between the spherical harmonic model and the input data, at 500 MHz. The order of the model is $L = 5$. Each subfigure charts the gain for a different plane.

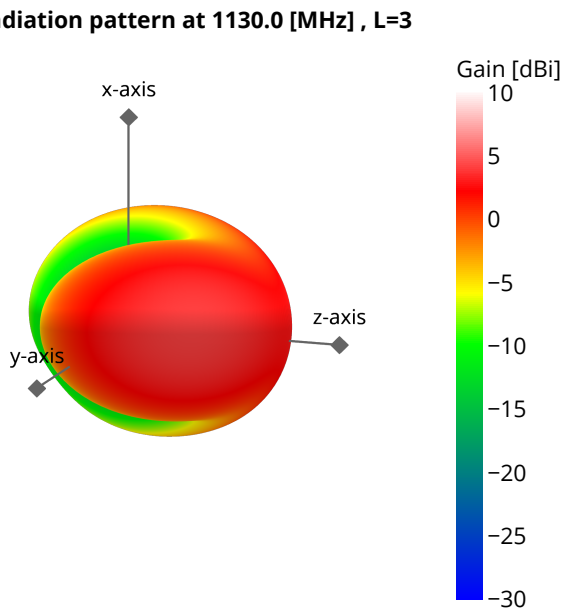

Figure 5.11: Antenna radiation pattern model, interpolated using spherical harmonics at order $L = 3$. The radius corresponds to gain [dB], with -30 dB representing zero radius.

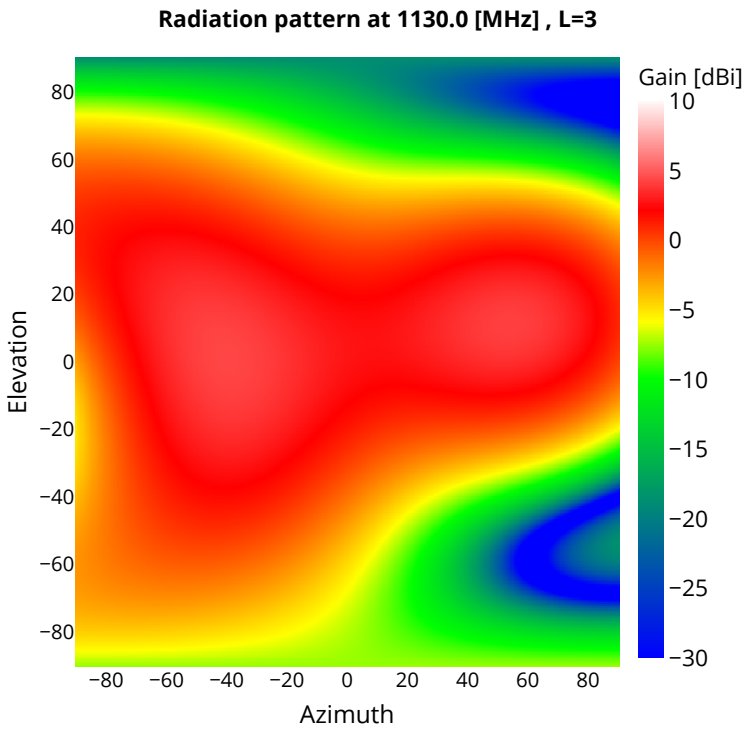

Figure 5.12: Antenna radiation pattern model in azimuth and elevation coordinates, interpolated using spherical harmonics at order $L = 3$.

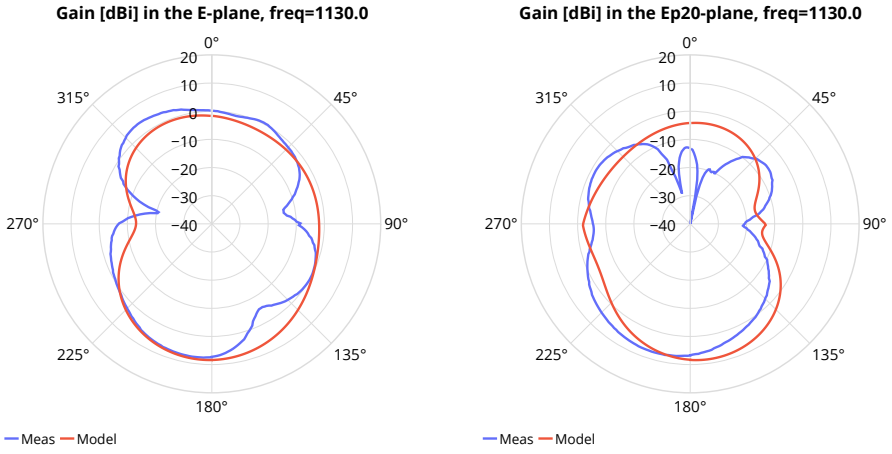

(a)

(b)

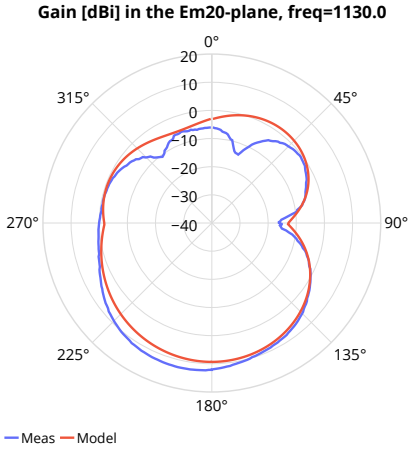

(c)

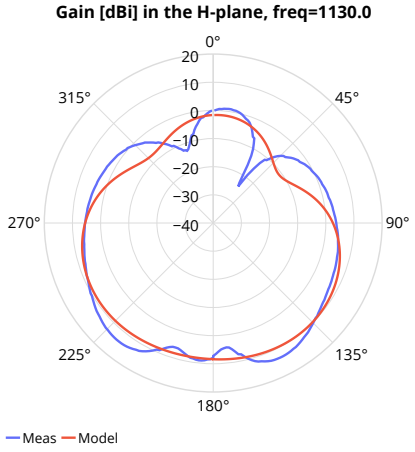

(d)

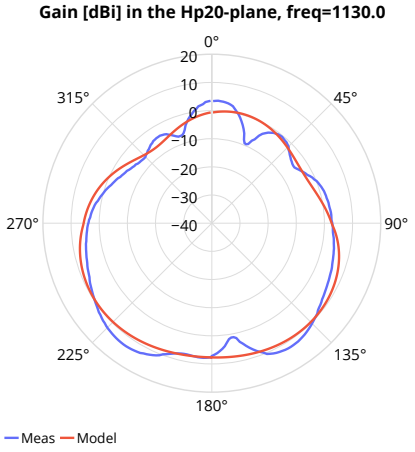

(e)

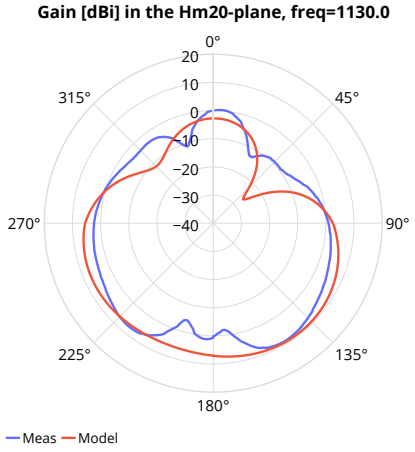

(f)

Figure 5.13: These plots display comparisons between the spherical harmonic model and the input data, at 1130 MHz. The order of the model is $L = 3$. Each subfigure charts the gain for a different plane.

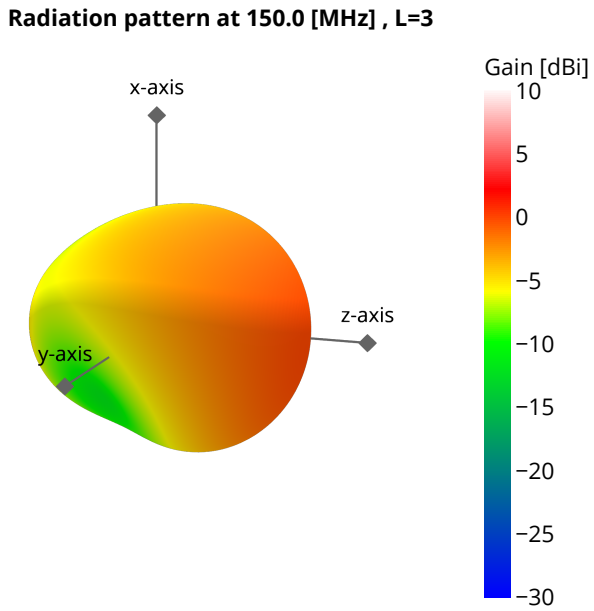

Figure 5.14: Antenna radiation pattern model, interpolated using spherical harmonics at order $L = 3$. The radius corresponds to gain [dB], with -30 dB representing zero radius.

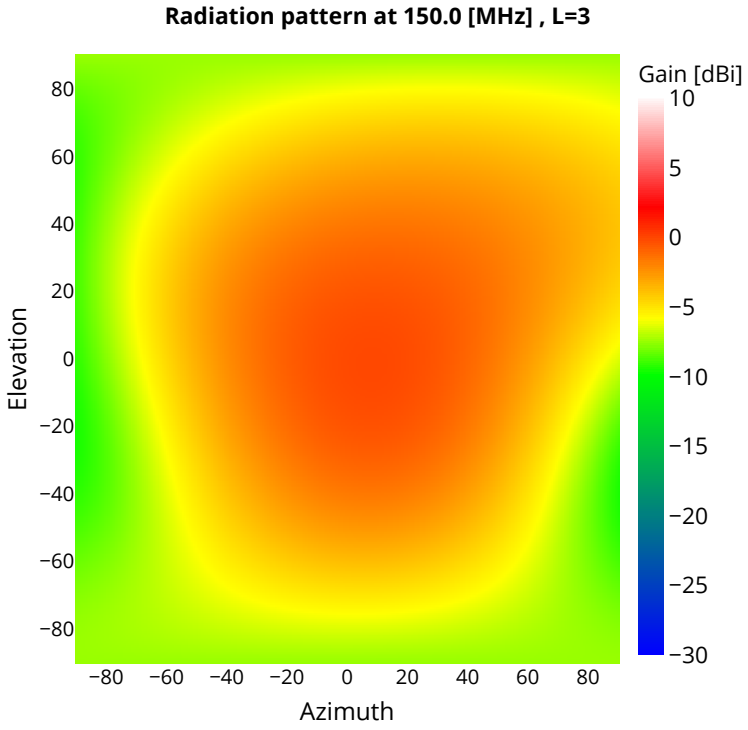

Figure 5.15: Antenna radiation pattern model in azimuth and elevation coordinates, interpolated using spherical harmonics at order $L = 3$.

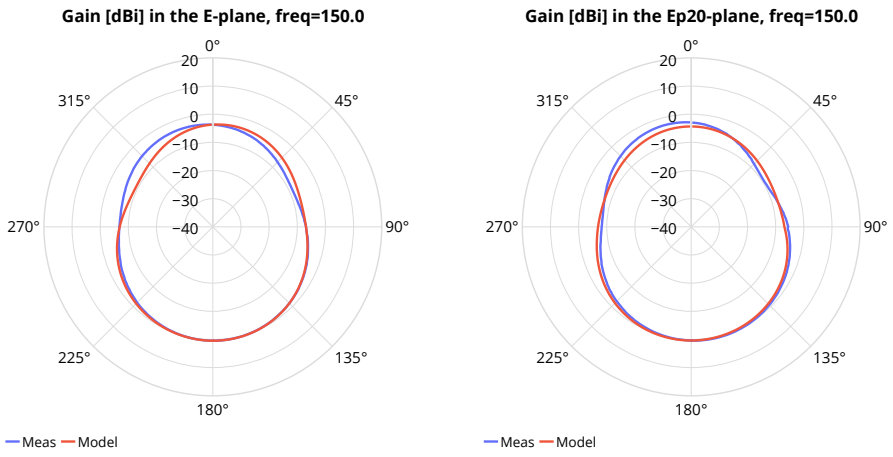

(a)

(b)

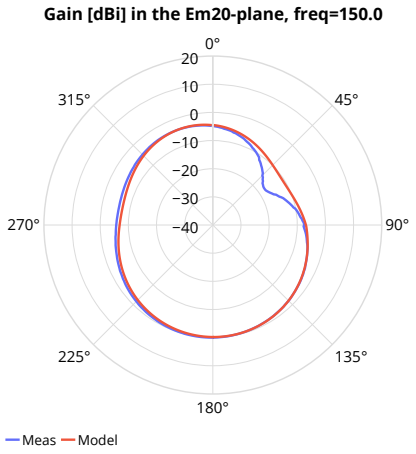

(c)

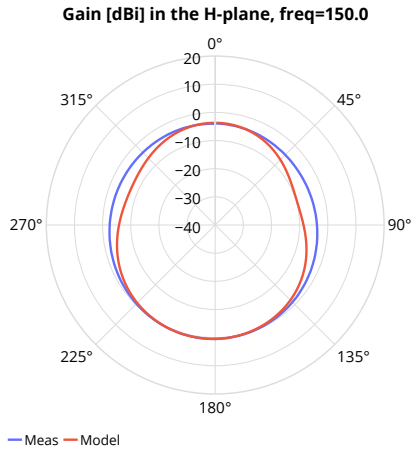

(d)

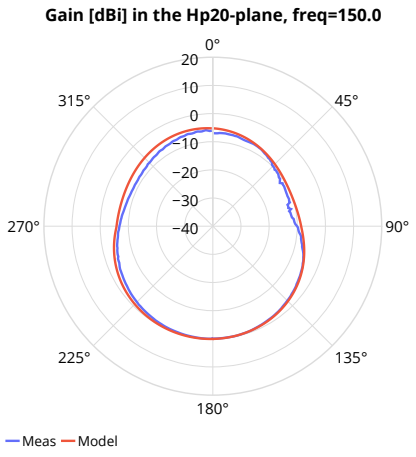

(e)

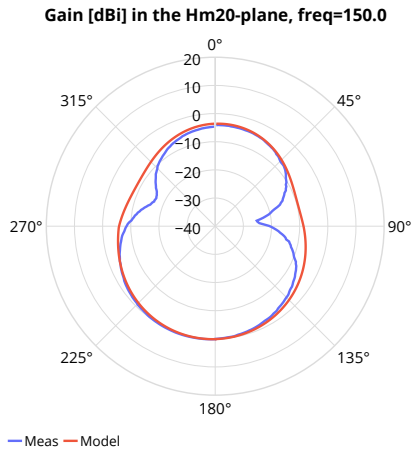

(f)

Figure 5.16: These plots display comparisons between the spherical harmonic model and the input data, at 150 MHz. The order of the model is $L = 3$. Each subfigure charts the gain for a different plane.

5.2 Frequency interpolation

5.2.1 Chart choices

The charts in this section display the frequency interpolated gain, along with measurement data. Four models based on SDFM interpolation are charted, in addition to a model that uses cubic interpolation. The red dots from the charts designate measurements of the antenna in the E-plane orientation (See Fig. 3.2a). The green dots represent the measurements from the H-plane orientation.

5.2.2 Parameter choices

The frequency interpolation has been performed on boresight gain measurements. These measurements were made in both the E-plane and H-plane orientation. The H-plane has vertical wave polarization, which has a Fresnel reflection coefficient that is much greater at higher incidence angles than horizontal polarization (See [2, Fig. 2-19]). This can cause stronger constructive/destructive interference on the receiver antenna. This is an undesirable effect, as it makes the gain measurements dependent on the specific surroundings of the measurement setup. The interpolation has therefore been performed on the measurements in the E-plane. The 4dB difference at 365MHz might be a consequence of destructive interference, although more data would be needed to be sure.

The interpolation was performed with rational filters that had different numbers of poles and zeros. Four results have been charted, two with phase and two without phase. These four charts were selected out of all possible combinations of n (zeros) and d (poles) such that $N_f = d + n + 1$ (See subsection 3.9.5). From the results with phase, we picked two charts that seemed representative of what the interpolated gain generally looked like for different numbers of poles and zeros. From the results without phase we have charted two of the most reasonable-looking results.

5.2.3 The results

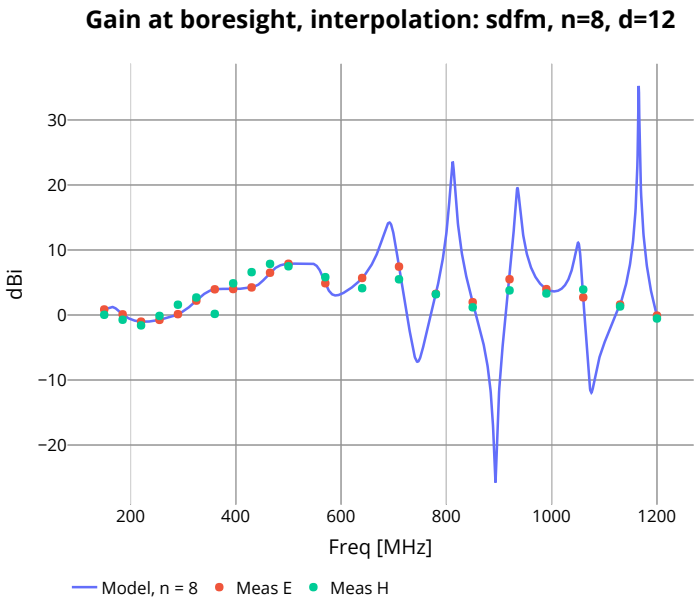

(a) SDFM interpolation with 8 zeros and 12 poles.

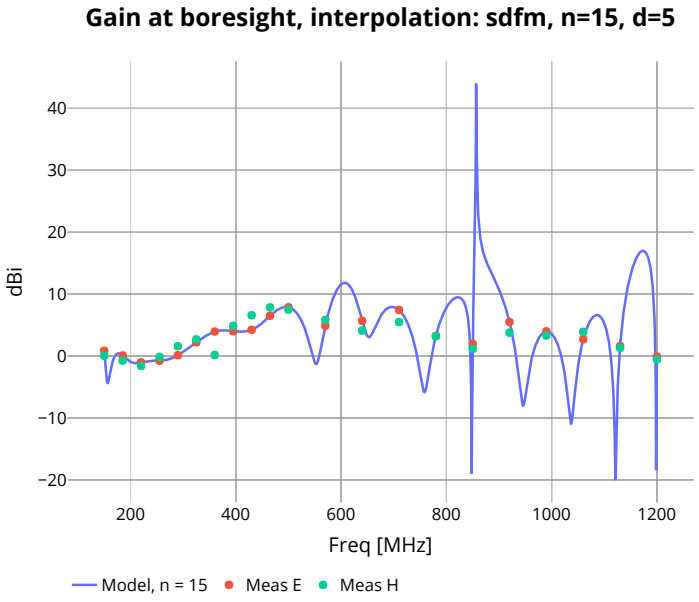

(b) SDFM interpolation with 15 zeros and 5 poles.

Figure 5.17: SDFM interpolation with phase.

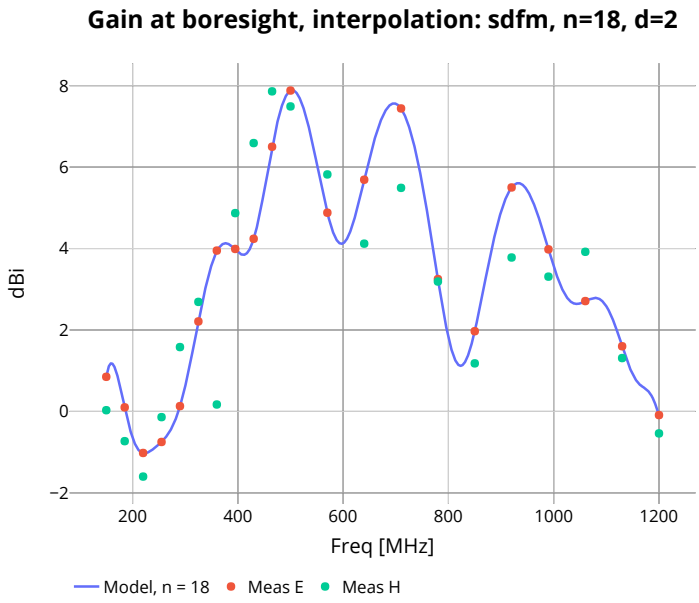

Figure 5.18: SDFM interpolation of the red measurements, with a 18-zero, 2-pole rational filter.

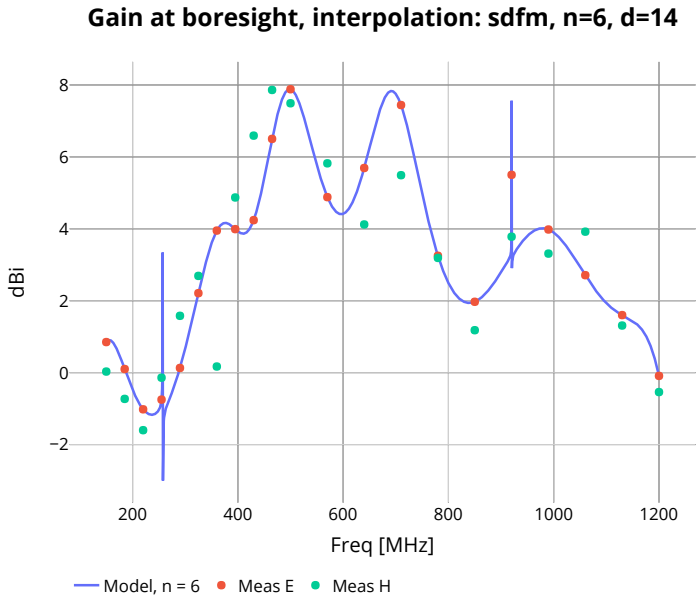

Figure 5.19: SDFM interpolation of the red measurements, with a 6-zero, 14-pole rational filter.

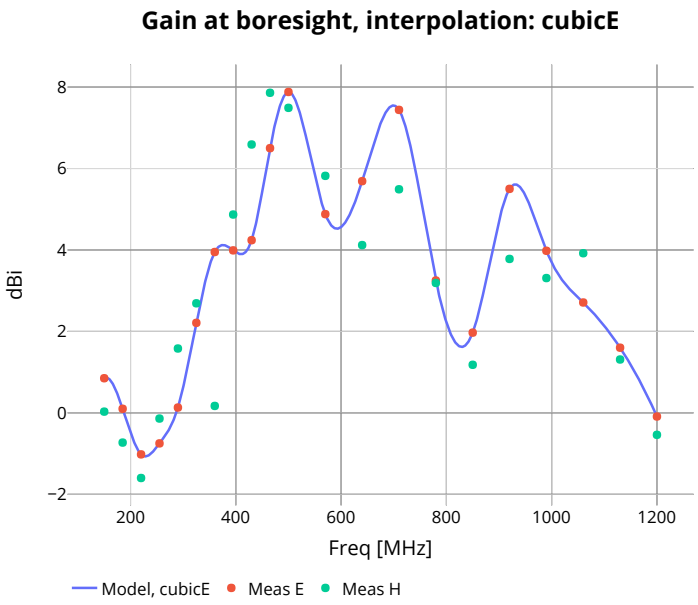

Figure 5.20: Cubic interpolation of the red measurements.

5.3 Characterizing the gate

5.3.1 Chart choices

In this section we have chosen to use three different charts. The first shows the direct signal and gated signal. The two others display the estimated gate function in linear and dB respectively. The peaks of the direct signal reflections have been marked with pink dots, and the corresponding times of the gated signal are marked with purple dots. Dashed lines have been drawn between these dots to illustrate their connection. The light colored lines represents the gated signals, while the dark colored lines represents the direct signals.

Signals from two different measurement setups are shown. The blue lines are signals representing the measurement setup with a short cable connected to the reflectors, while the green lines represents the signals with an added 5m cable.

The two charts showing the estimated gate-function use separate colors for the signals with different cable lengths. This was done so we can analyze the two measurement setups separately. A theoretical gate-function was added on top, which has its peak set to the maximum value of the measured gate function. It's worth mentioning that we might not have sampled the true peak of the gate-function. If this is the case, the theoretical function we have charted will be slightly wrong relative to the estimated one.

5.3.2 Parameter choices

The RIMFAX electronics has many configurations which specifies what kind of gating shall be applied. These are listed in Table 4.1. We have chosen to display results for Configuration ID 14, 16, 18 and 24. The peak of the theoretical and estimated gate function has been set to -3dB, as this identifies that the maximum received power for this gated system is half of what an equivalent Continuous Wave system could provide.

5.3.3 The results

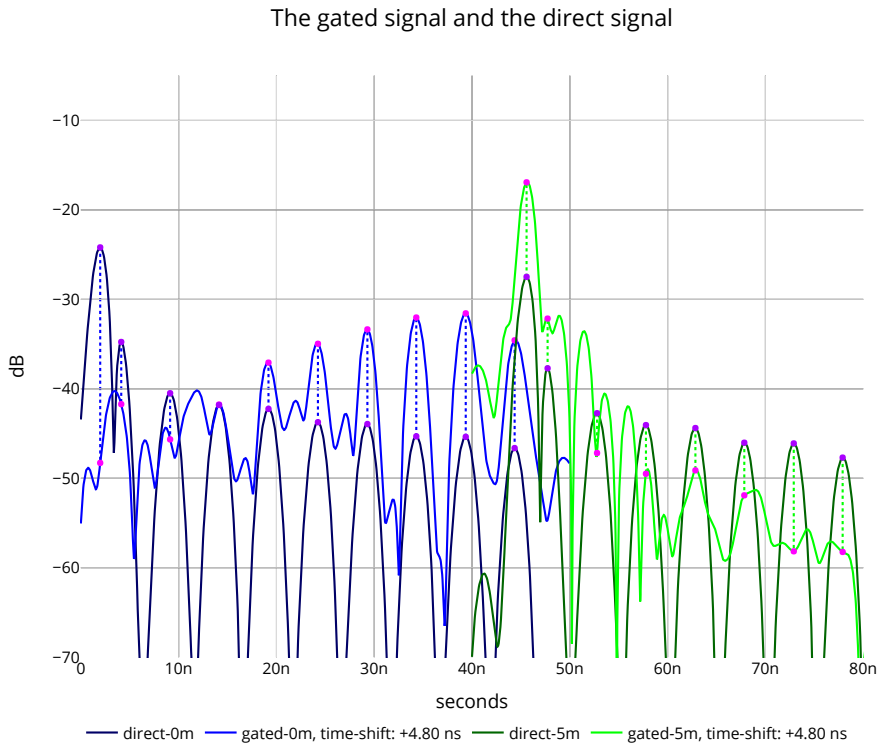

(a) The light blue and light green is the gated signal measured with two different cable lengths. The dark blue and dark green traces are the measurements of the direct signal, with the same cables. The gated signal is in dBFS, while the direct signal is simply the reflection coefficient in dB.

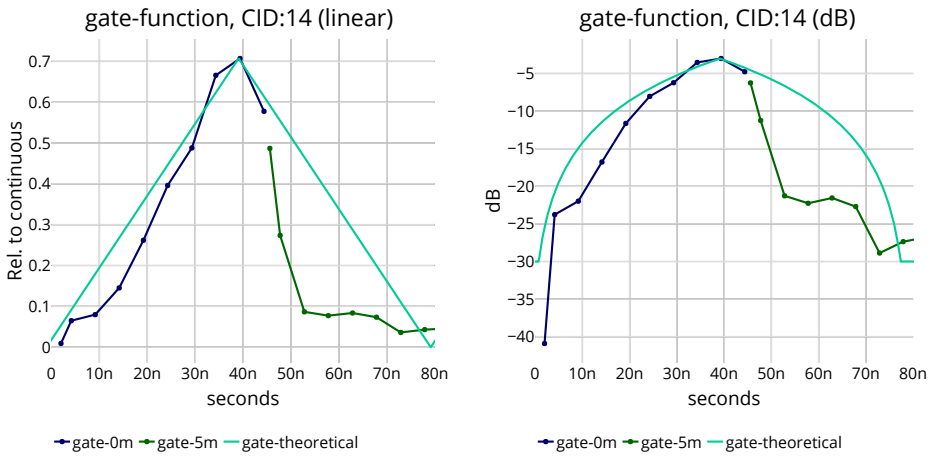

(b) Gate in linear

(c) Gate in decibels

Figure 5.21: Gate function for CID=14

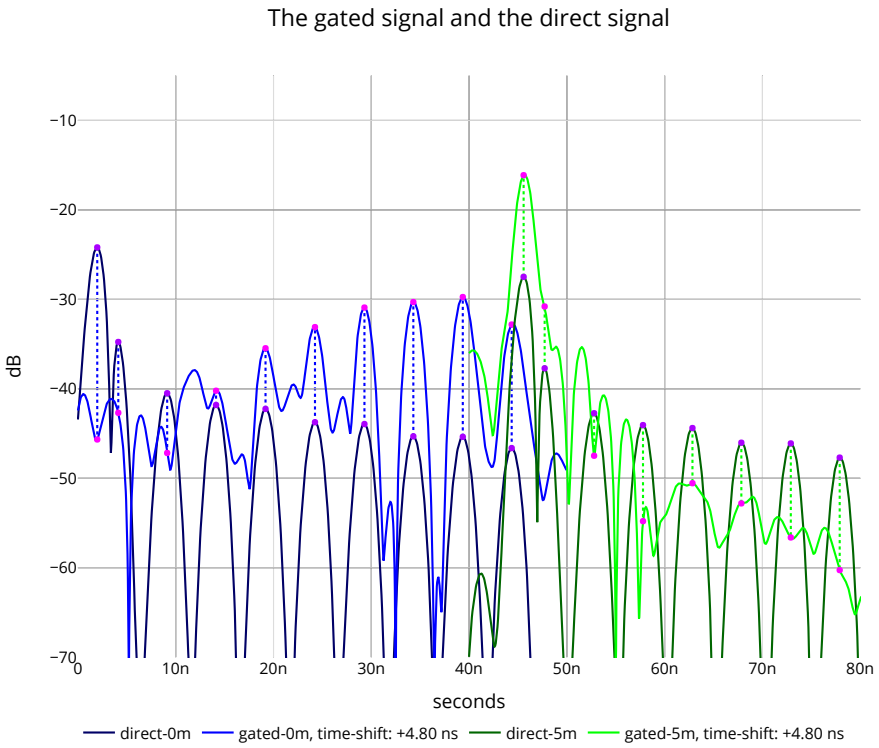

(a) The light blue and light green is the gated signal measured with two different cable lengths. The dark blue and dark green traces are the measurements of the direct signal, with the same cables. The gated signal is in dBFS, while the direct signal is simply the reflection coefficient in dB.

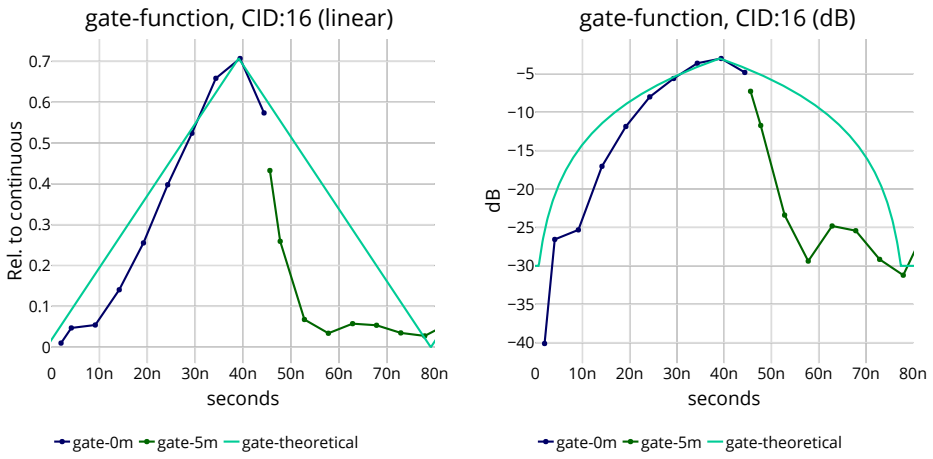

(b) Gate in linear

(c) Gate in decibels

Figure 5.22: Gate function for CID=16

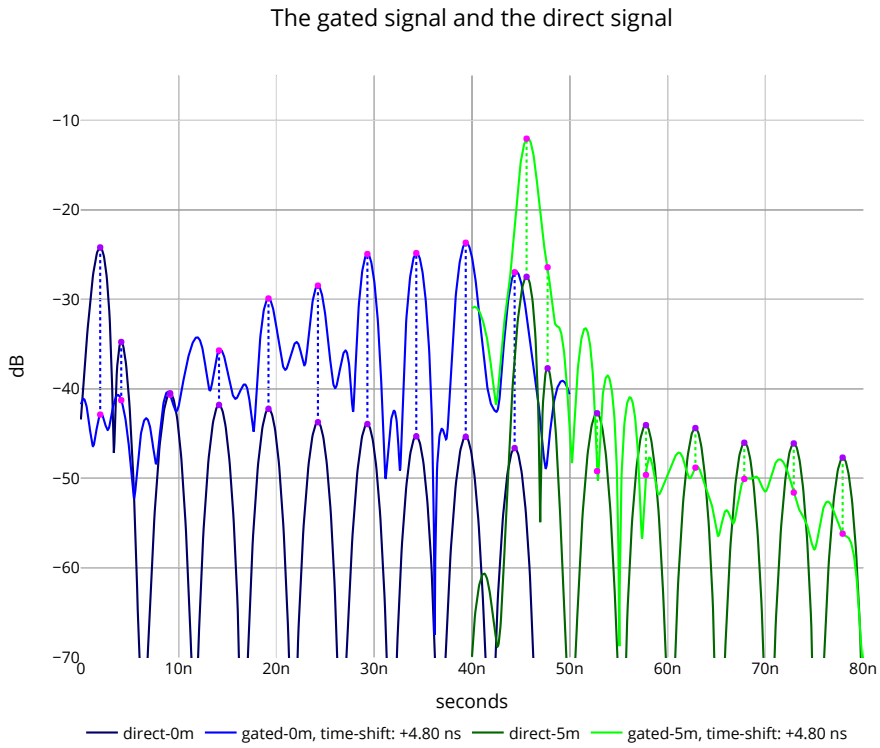

(a) The light blue and light green is the gated signal measured with two different cable lengths. The dark blue and dark green traces are the measurements of the direct signal, with the same cables. The gated signal is in dBFS, while the direct signal is simply the reflection coefficient in dB.

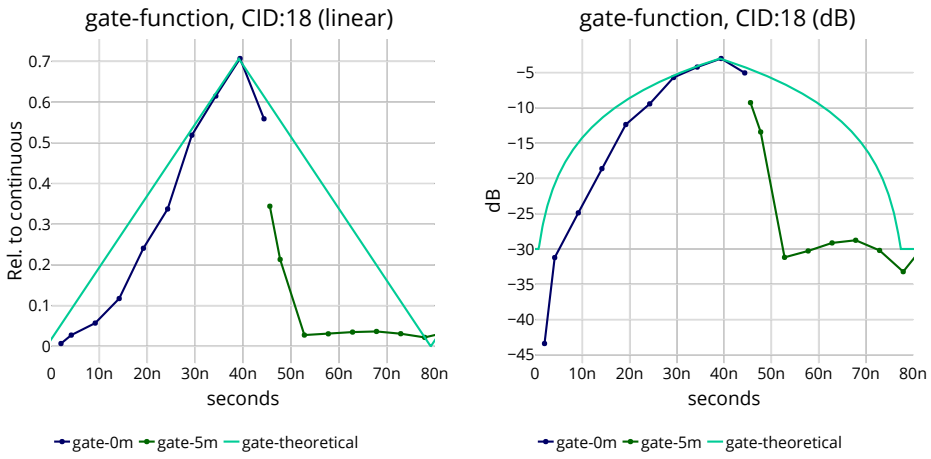

(b) Gate in linear

(c) Gate in decibels

Figure 5.23: Gate function for CID=18

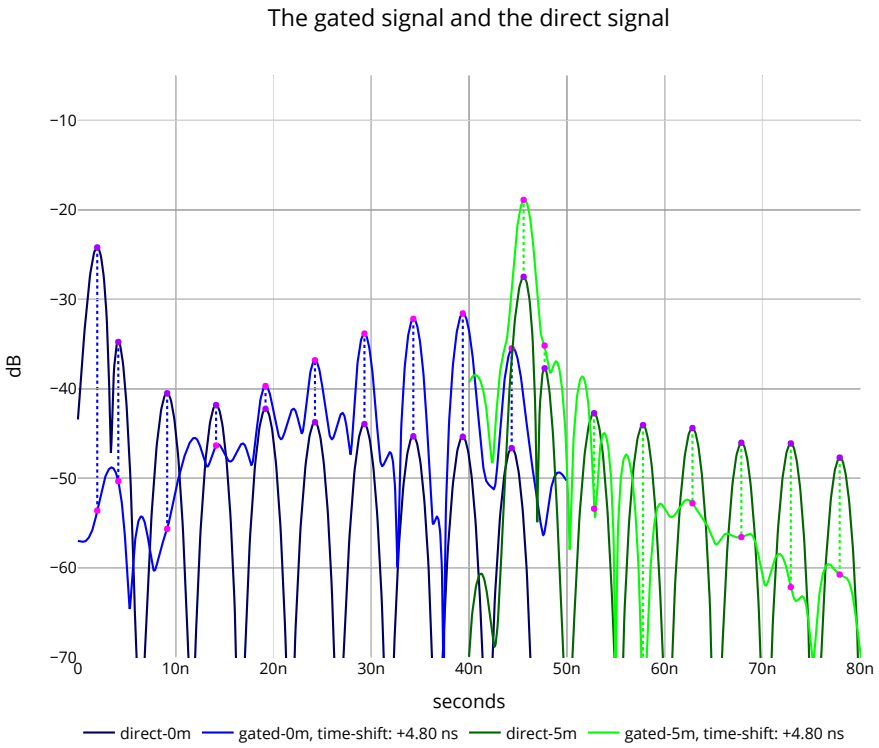

(a) The light blue and light green is the gated signal measured with two different cable lengths. The dark blue and dark green traces are the measurements of the direct signal, with the same cables. The gated signal is in dBFS, while the direct signal is simply the reflection coefficient in dB.

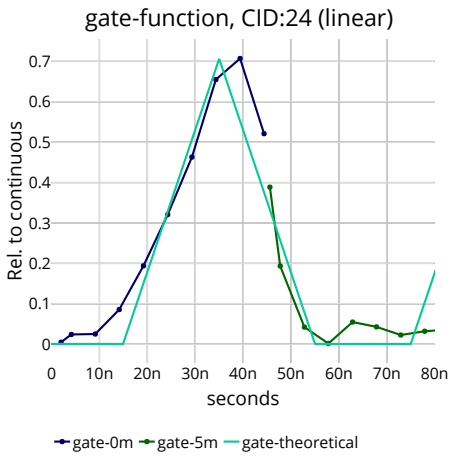

(b) Gate in linear

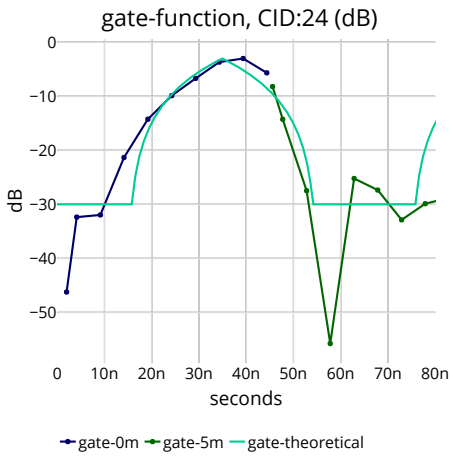

(c) Gate in decibels

Figure 5.24: Gate function for CID=24

Chapter 6

Discussion

6.1 Overview

In this chapter we first present a method to evaluate the results from the Spherical Harmonic interpolation. This method is applied and discussed at three different frequencies. The same process has been repeated for every frequency in our measured radiation patterns, and the performance of the interpolation has been graded (see Table 6.1).

The next part lays out a discussion of the SDFM interpolation with and without phase information. A few suggestions for improving the frequency characterization of the antenna are then presented.

The third part of the discussion is concerned with the gate-function. Gate-function estimates from four different gate configurations are compared and discussed in relation to their theoretical counterpart.

Finally we present our suggestions for estimating the dielectric constant, in light of the interpolation results and the gate-function estimates.

6.2 Spherical Harmonic interpolation

6.2.1 Evaluating the accuracy of the interpolation

We do not know the true gain pattern, so we cannot calculate the exact error of our model. If a more uniform distribution of data-points of the radiation pattern was sampled, one could randomly extract points to not use as input to the interpolation algorithm. Then an MSE of the model's predictions could be estimated. Unfortunately, the antenna was rotated on just six different axes. It would therefore only be misguiding to estimate an MSE from these measurements.

However, we can still assess some degree of accuracy of the model, under certain assumptions. We have chosen to chart the model's predictions on top of the measured data, which is the input of the algorithm generat-

ing the model. Similarities between these does not by itself indicate that the model has good accuracy, but it does reveal that the data is well described by the functions.

The projection of measured data onto the SH-functions is an example of dimensionality reduction, which is essentially what we do when we abstract out information. It is the attempt to find a pattern, a simpler way of representing the information we are processing. For example, when we view the image in Fig. 6.1, we abstract out the 3d-object of a staircase. This works locally, for each turn of the staircase, but it clearly doesn't work for the whole figure. We must be careful when trying to evaluate the accuracy of our model. The true gain of the antenna is known for just a few cuts of the radiation pattern, and these were used to create the model. To evaluate whether our model is accurate in general, we need to do so under two assumptions:

1. The "nulls" can be roughly located from the measured radiation patterns.
2. The data has a dominant behavior of spherical waves.

We have also chosen three sectors of the interpolated radiation pattern for which we will evaluate its accuracy.

A) $\theta_{azel}, \phi_{azel} \in (90°, 270°)$

B) $\theta_{azel}, \phi_{azel} \in (135°, 225°)$

C) $\theta_{azel}, \phi_{azel} \in (160°, 200°)$

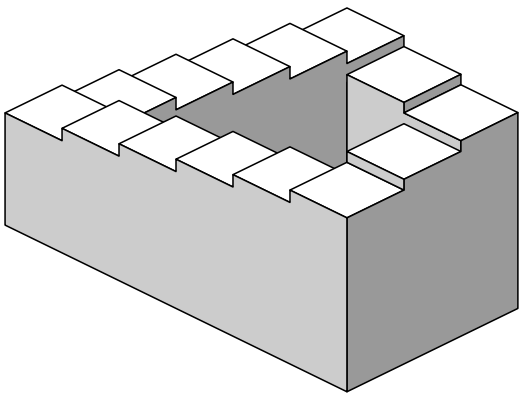

Figure 6.1: The Penrose stairs is an impossible object created by Lionel Penrose and his son Roger Penrose. *Credits: Sakurambo*.

6.2.2 The shape of the dips

We can localize the nulls by characterizing the dips in the radiation pattern. By comparing the lowest dips in Fig. A.1c, Fig. A.1d,Fig. A.1f and Fig. A.2d,

we can get an idea of the shape of the dips. Generally we see that the dip gets steeper as you get closer to its lowest point, and the -10dB level seems to be approximately 22.5°, or more, away from the bottom. If we assume the dips are approximately symmetric around their lowest point, we can get an idea of how far away the nulls are by looking at the gain level at any point. If the gain is above -10dB, we should expect that the null is more than 22.5° away from this point.

6.2.3 At 500 MHz

The location of the nulls

From the E,Ep20 and Em20 planes in Fig. A.2 and Fig. A.3 we see that the nulls in the E-plane move when the frequency changes. They never seem to move into sector A until the frequency reaches 710MHz. In the H-plane of Fig. A.2, the null on the right-hand side seems to move backward, as the frequency increases. On the left-hand side of the chart we observe that the null at 360 MHz also seems to move backward as the frequency reaches 430MHz. In all the charts of Fig. A.2, it seems clear that the radiation pattern becomes of lower order as the frequency approaches 500 MHz. However, there still seems to be nulls within sector A, as the Hm20 chart at 465MHz show us. Due to the general tendency of lower order behavior and the nulls moving backward as the frequency increases, in addition to there being no nulls within sector B in any of the charts, it seems fair to assume they are not within the sector B.

Assumption: Nulls are outside sector B.

Analyzing the model

We start by inspecting Fig. 5.4. Even at $L = 2$ the spherical harmonic functions seem to capture the most important behaviors in the E, Ep20 and Em20 planes. The mainlobe is much narrower in the H-plane, which explains why the low-order spherical harmonic functions are less able to capture the general pattern of the measurements. Still, the differences seem to be quite minimal within sector C. The small differences in the comparison plots and the low-order behavior observed in Fig. 5.3, seem to indicate relatively good performance for sector C.

When the truncation order is increased to $L = 3$, we observe that the model has a narrower backlobe (See Fig. 5.5 compared to Fig. 5.2). This is clearly closer to the truth, judging by the comparison in Fig. 5.7 (E,Ep20,Em20). The model also seem to perform better than $L = 2$ in sector B, with a maximum difference of about 2dB between the model and measurements. We still see a low-order behavior in Fig. 5.6, so it seems appropriate to use the model for sector B.

By increasing the truncation order to $L = 5$, we observe that the model

converges well to the measurements in Fig. 5.10. This supports our assumption that the data has a dominant behavior of spherical waves. However, we do see signs of overfitting, judging by the two lobes in Fig. 5.8. Because the lobes are quite far from the coordinates of the measurements, it seems likely they are simply a bi-product of the least-squares algorithm misusing the higher-order functions. The interpolated radiation pattern at all the other frequencies have used a limited truncation order of $L = 3$ to avoid this issue.

6.2.4 At 1130 MHz

The location of the nulls

As the frequency increases, we get a more and more complex radiation pattern. For example, at 920 MHz a dip appears in the radiation pattern at around 160° (See Fig. A.4f). At 1130 and 1200 MHz, the pattern forms a tiny lobe in the forward direction. The dips observed in these figures indicate that there are nulls within sector C for all frequencies between 920 MHz and 1200 MHz.

Assumption: Nulls are within sector C.

Analyzing the model

By observing Fig. 5.13, we generally see that the SH-interpolation performs much worse than at 500 MHz, due to the increased complexity of the radiation pattern at this frequency. Higher order SH-functions are clearly needed to describe the tiny forward lobe, and the radical changes between the $\pm$20-planes.

The difference between model and measurement is consistently high in sector C. In Fig. 5.13f, we see a difference of up to 10 dB. Because the SH-functions do not seem to capture important features of the radiation pattern, even at boresight, the model should be classified as unsuccessful at this frequency.

6.2.5 At 150 MHz

The location of the nulls

By observing the Em20 plane in Fig. A.1, we see a dip at $\approx 45°$, which cannot be detected in the E and Ep20 planes. The dip seems to be around -18 dB at its lowest point. We use the dip on the red graph in the Hm20 plane as reference for what the radiation pattern looks in close proximity of a null. The -18 dB point is around 20° away from the bottom of the lowest point. It should be kept in mind that this is a different frequency, but by comparing the red and purple dips from the Hm20 plane we see that the dip is quite similar for close frequencies. It therefore seems reasonable to assume that the dip in Fig. A.1c is somewhere around 20° away, which

keeps it out of sector A. Using a similar analysis on the dip in the Hm20-plane, at around 90°, we cannot be sure that this null is outside sector A. It should, however, be a fair distance from sector B.

Assumption: Nulls are outside sector B.

Analyzing the model

In Fig. 5.16 we see small differences within sector B for all charts. The maximum difference seems to be around 2 dB, at 135° in Hm20-plane. The model is likely to be accurate within sector B, as long as our assumption about the nulls' location is correct. In sector C, there is virtually no difference between model and measurements.

6.2.6 Summary

A similar analysis to these have been carried out on the other frequencies for which we have interpolated the radiation pattern. The interpolation has been rated with numbers ranging from 0 to 3, where 3 is best and 0 is worst (see Table 6.1). These should not be seen as absolute evaluations of the interpolation, but only to rank the inter-frequency results relative to each other. None of the models produced good results within sector A. Two frequency bands; 150-220 MHz and 465-570 MHz gave relatively good results within sector B. All the interpolated models with frequencies ranging from 150-780 MHz, except 255 and 290 MHz, gave acceptable results within sector C.

6.2.7 How the interpolation could be improved

The big limiting factor to the interpolation algorithm is data. As discussed in subsection 6.2.3, lobes appeared in the interpolated radiation pattern. Even though we had better correspondence between model and measurements for a truncation order of $L = 5$, the lobes are likely not present in the true radiation pattern. Thus, we seem to have reached a limit for how accurate our model can become with current measurements.

If a more accurate and more general model of the radiation pattern is desired, the measurement process should be changed so that a more uniform distribution of angular coordinates are sampled. For example, one might employ the "igloo" sampling scheme from [17].

Frequency [MHz]	Nulls absent	Grading in B	Grading in C
150	B	3	3
185	A	3	3
220	B	2	2
255	B	0	0
290	B	0	0
325	B	1	2
360	C	0	1
395	C	0	2
430	C	0	1
465	B	2	3
500	B	2	3
570	B	2	3
640	B	0	2
710	B	0	1
780	C	0	1
850	C	0	0
920		0	0
990		0	0
1060		0	0
1130		0	0
1200		0	0

Table 6.1: This table shows the results after having went through the same evaluation procedure as subsection 6.2.3 for each frequency. The second column shows the largest sector for which nulls are presumed to be absent. The grading of the interpolated radiation pattern in sector B and C are in the succeeding two columns.

6.3 Frequency interpolation

6.3.1 SDFM with phase

The two charts displaying frequency interpolation with phase, from Fig. 5.17, look unreasonable. Removing the phase seems to improve the interpolation, so we will investigate some of the reasons why the phase may cause this behavior. The cables between transmitter/receiver and the antennas has the effect of a linear-phase filter on the measured signal. If this has not been corrected for in the measurements, the poles and zeros will not be placed correctly. A change in distance between the antennas has the same effect on the phase that these cables have. However, the distance between the antennas fluctuates, while the cable lengths remain the same. The phase is more sensitive to distance perturbations at higher frequencies, due to the reduced wavelength. At 1200 MHz a mere 12.5 cm change in distance would cause a 180° phase-shift. This might explain why the interpolated gain seems to get more unrealistic behavior as the frequency increases.

6.3.2 SDFM without phase

When the interpolation is performed without phase, the results look more reasonable, as can be seen in both Fig. 5.18 and Fig. 5.19. Fig. 5.19 has two instabilities, where the one at 920 MHz is especially out of order. Fig. 5.18, on the other hand, seems to grasp the general behavior of the frequency measurements quite well. The cubic interpolation in Fig. 5.20 gives a similar general behavior. One difference is the almost linear curve through the 5 rightmost points, which might be more realistic than the added peak in the SDFM-interpolated curve. We also see that the valleys at 600 and 800 MHz are deeper in the SDFM interpolated curve. This is a natural feature of the zeros in rational filters.

6.3.3 Summary

We have seen that the phase had a deteriorating effect on the SDFM interpolation, and that removing it gave at least one quite reasonable-looking result. Before we conclude our evaluation of the SDFM interpolation, there are two things we must remember. First, the radiation efficiency will in reality not be a constant, as we have assumed (see subsection 3.9.6). Secondly, the phase is important for placing the poles and zeros correctly. These two facts delegitimizes the method as an MBPE approach. Thus, we can not use this method to interpolate every direction of the radiation pattern with our current measurements. If interpolation of the boresight gain is desired, cubic interpolation should be a more reliable option.

6.3.4 Improving the SDFM interpolation method

The most important step to improving SDFM interpolation is to do more measurement experiments. We suggest using a cavity based method,

such as the one in [31] to estimate efficiency. Smaller frequency steps between gain measurements could also be beneficial for interpolating the gain/frequency behavior. If the amount of samples is adequate, a least-squares approach could be used. A piece-wise interpolation scheme, like the one in [16], would perhaps be the easiest to apply on radiation patterns, as the number of poles and zeros is fixed.

6.4 The gate-function

6.4.1 Comparing the peaks of the reflectors

In this section we discuss charts of the direct signal and gated signal and relate them to the estimated gate-function. We start by looking at Fig. 5.21. In the two blue graphs we see that the peaks of the gated signal is right on top of the direct signal from the fourth peak and on.

With the added cable, the green gated signal has a more unclear pattern. The first peak is right on top of the direct signal, but from then on we observe a pattern which does not resemble the direct signal. Observe the valleys that go down below -60 dB, at around 50 and 55 ns. Between them we see something that looks very much like the two first reflectors, but dampened. To the right of the 55 ns valley, this pattern is repeated. This might be a consequence of impedance mismatch, perhaps at the connector between the added cable and the short cable. If this is the case, reflections might go back and forth between the connector and the RIMFAX electronic box, which reflects much stronger than the VNA. This can cause the same reflectors to appear multiple times in the time-domain signal. These layered reflections might also cancel each other. This may be what has happened at the third peak of the green direct signal, which overlaps with a valley in the gated signal. A similar pattern of the the first two reflectors can be seen in Fig. 5.22a and Fig. 5.23a. Because of this, the second part of the estimated gate-function cannot be used, unless new experiments are done. A more thorough analysis could be done if other windowing functions were used, but we already know from the analysis in subsection 4.3.3 that the sidelobes alone are not strong enough to produce these effects.

6.4.2 The estimated gate-function

In Fig. 5.21b the estimated gate-function starts off slower than the theoretical model. This might be caused by the electric properties of the gate. Near the top of the estimated gate-function it overshoots the theoretical one. It is worth mentioning that the peak value of the true gate-function might not have been sampled. If this is the case, the estimated function may actually not overshoot the theoretical one.

The configurations in Fig. 5.22 and Fig. 5.23 have a different attenuation (see Table 4.1), and this seems to change the estimated gate-function somewhat. The most noticeable change is the linear behavior near the top in

Fig. 5.23b. The measurement setup used to generate this gate-function estimate had a lower attenuation in both Rx and Tx. This suggests a non-linear behavior somewhere in the gate. It might even be that the gate-function changes based on the amplitude of the received signal.

However, the estimated gate-functions correlate better with each other than with the theoretical one. The slower ascent of the estimated gate-functions can be explained by the electronics being non-ideal. Thus, we would suggest that this behavior is indicative of how the gate physically works, and is not just induced by the measurement setup. This is supported by the observation that the peaks of the direct signal and the gated signal overlap well from the 4th peak and on.

The estimated gate-function from Fig. 5.24 looks remarkably similar to those discussed above, even though the theoretical functions from Fig. 4.5 are quite distinct. We will compare it to the estimated gate-function with CID 14, as this mode has the same Rx- and Tx-attenuation. By observing the gate-functions at 20-30 ns, we generally see that CID 24 is "slimmer". CID 24 also has lower decibel values around 0-10 ns. These observations are signs that the Rx-gate switches "on" later for CID 24. One reason for why the gate-functions are not as distinct as Fig. 4.5 might be that the Rx-, Tx- and antenna-gates do not switch simultaneously. In Fig. 4.4 we see that the antenna gate switches earlier than the Rx-gate, which might cause some proportion of the signal to be "leaked" to the receiver before the Rx-gate is "on".

6.4.3 Summary

When the gates switch simultaneously, the estimated and theoretical gate-functions have distinct features which may be caused by electrical properties of the gate. This suggests that there should be room for improving received signal correction by employing an estimated gate-function. We observed less differences than expected when the gates were configured to switch at different times. A new experiment could confirm/deny our proposition that this might be caused by leakage through the Rx-gate. Before the estimated gate-function is used to correct the received signal, we suggest to do measurements of the gate in several other configurations. It is important that the non-linear properties are further characterized, such that we may know how much the gate-function varies with signal amplitude.

6.5 Estimating the dielectric constant

In subsection 3.3.3, we showed that the far field model that accepted 10% error in wave impedance put the far field above the ground for frequencies higher than 430 MHz. The phase difference model sets the far field above the ground for frequencies lower than 1130 MHz. Because of this, we

suggest two different approaches for estimating the dielectric constant:

1. Use the frequency band 465-780 MHz with the Fresnel reflection model from Section 2.3.

2. Use the frequency band 465-570 MHz, and apply the I2EM model from Section 2.4 on a surface that is within sector B.

The first approach will probably produce results which are just marginally better than the normal incidence model from Section 2.2, as the gain isn't changing very much in sector C. The second, however, might be a significant improvement if a proper roughness estimate of the surface is used. The radiation pattern cuts fall off by up to 10dB, relative to boresight, at the 225° and 135° polar angles (see Fig. 5.7). These effects are not taken into account with the simple forward gain model from Section 2.2. Thus, even if the model does not perfectly overlap with the measurements, it might still better predict the relative received/transmitted power than the forward gain estimate of Fresnel transmission. Depending on whether the transmit medium is lossy, a narrower frequency band might be advisable.

Because SDFM interpolation cannot be theoretically justified on our radiation pattern measurements, we instead suggest using nearest-neighbour interpolation of SH-interpolated radiation patterns, as the near-frequency radiation patterns look quite similar. The mean can then be estimated, both along frequency and spatial dimensions.

In our discussion of the gate-function we found that there should be potential for improving received signal correction by using an estimated gate-function rather than the simple theoretical model. Measured signal amplitude is the deciding factor in the equation of Fresnel reflection, so it should be especially important for estimating the dielectric constant.

Chapter 7

Conclusion and future works

7.1 Conclusion

In subsection 1.1.3 we stated the overarching goal of our thesis: 'Laying the groundwork for measuring the dielectric constant of the surface layers on Mars'. The second step of the procedure was to characterize the spatial and frequency behavior of the antenna gain. We have seen that spherical harmonic functions were able to describe the measured data well at certain frequencies, when the radiation pattern was of low order. The best results appeared around frequencies 150-220 MHz and 465-570 MHz.

The frequency interpolation did not provide useful results. The lack of radiation efficiency measurements means the SDFM interpolation could not be implemented as a true MBPE interpolation scheme. Not having accurate phase measurements further delegitimatizes the interpolation as an MBPE approach. Thus, interpolating each direction of the radiation pattern can not be said to have the same theoretical rigour as the application in [16].

The third step of the procedure was to correct the received signal for the gate-function. We have seen that the estimated gate-function is similar to what one would expect from theory, while still having features that distinguishes it from the theoretical gate-function. This shows potential for improving received signal correction by using the estimated one. Delaying the antenna- and Rx-gates did not seem to change the estimated gate function much, and we speculated whether this was caused by leakage in the Rx-gate.

In Section 6.5 we suggested two approaches for estimating the dielectric constant, which due to far-field considerations applied frequency bands at the middle of the frequency spectrum. We proposed to use a nearest-neighbour selection of which SH-interpolated radiation pattern to use at a particular frequency.

7.2 Future works

The Spherical Harmonic interpolation we used in this thesis is arguably the best method to interpolate our measurements, due to its theoretical origin and its ability to surface-fit an arbitrary set of coordinates. Still, it would be interesting to compare it to other methods, like the "summing method". The only way to improve our interpolation method is to get more measurements, but this would be a complex and tedious task. It would be necessary to have an automated measurement setup which could measure the radiation pattern quite uniformly. We would perhaps employ the "igloo" sampling scheme from [17].

The frequency interpolation also necessitates more measurements for improval. The first thing we would want to do is to estimate the radiation efficiency. We would then use a cavity based method, like the one in [31]. Secondly, we would try to estimate the electric field with properly calibrated phase. Finally, we would measure the boresight gain with small frequency steps. This would give us the ability to evaluate the performance of SDFM interpolation with different number of samples as input.

More insight into the gate-function would also be desirable. We have already expressed that the estimated gate-function has features which distinguishes it from the theoretically "ideal" gate-function. By doing more measurement experiments with different configurations and different cable reflectors, it would perhaps be possible to characterize the non-linear properties of the gate-function. If the second part of the gate-function needs to be estimated, it would be important to find the cause of the undesired reflections which were discussed in subsection 6.4.1.

In subsection 1.1.3, we stated the fourth step of the procedure to estimate the dielectric constant: 'Extracting the surface reflection'. This needs to be done to estimate the dielectric constant. To extract the surface reflection, we need to find the surface in the radar traces. This could perhaps be done with image analysis techniques on radar images, like the one in Fig. 1.5.

Appendix A

Comrod measurements

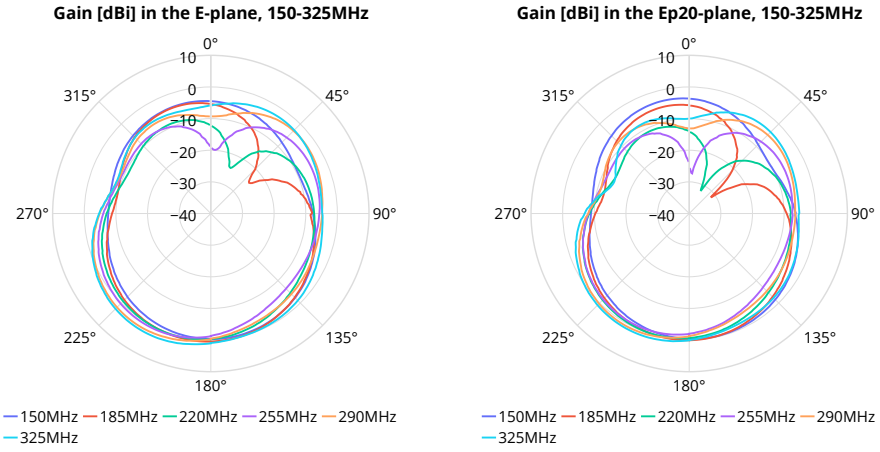

(a)

(b)

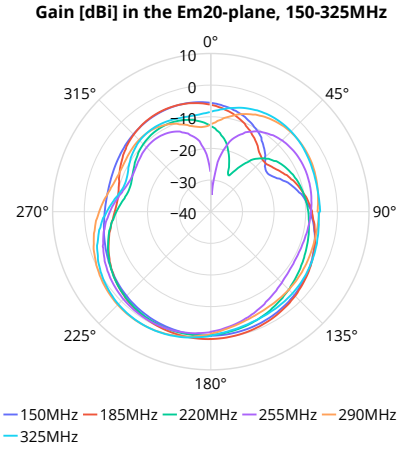

(c)

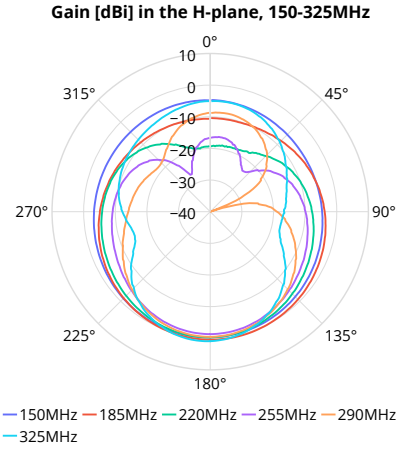

(d)

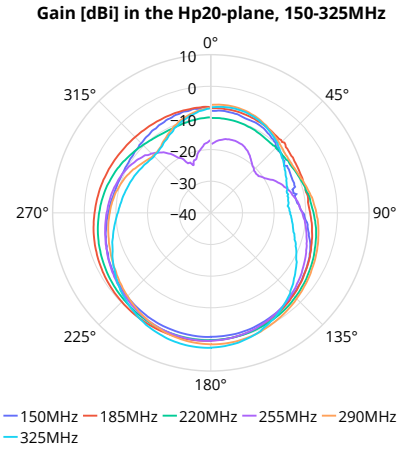

(e)

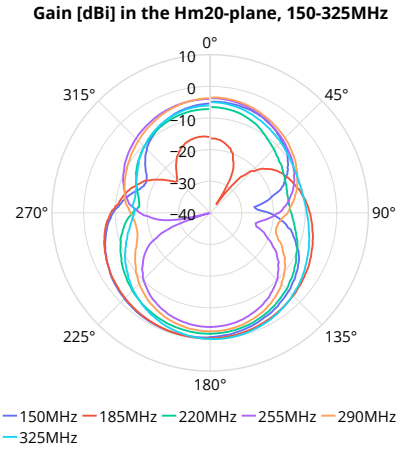

(f)

Figure A.1: These plots show the gain across all 6 cuts of the radiation pattern for the frequency range 150-325MHz. Rx: Radar Imager for Mars' Subsurface Experiment (RIMFAX), Tx: LPDA antenna. The mast height of rimfax was $\approx 4m$ in the H-plane measurements and $\approx 0.82m$ in the E-plane.

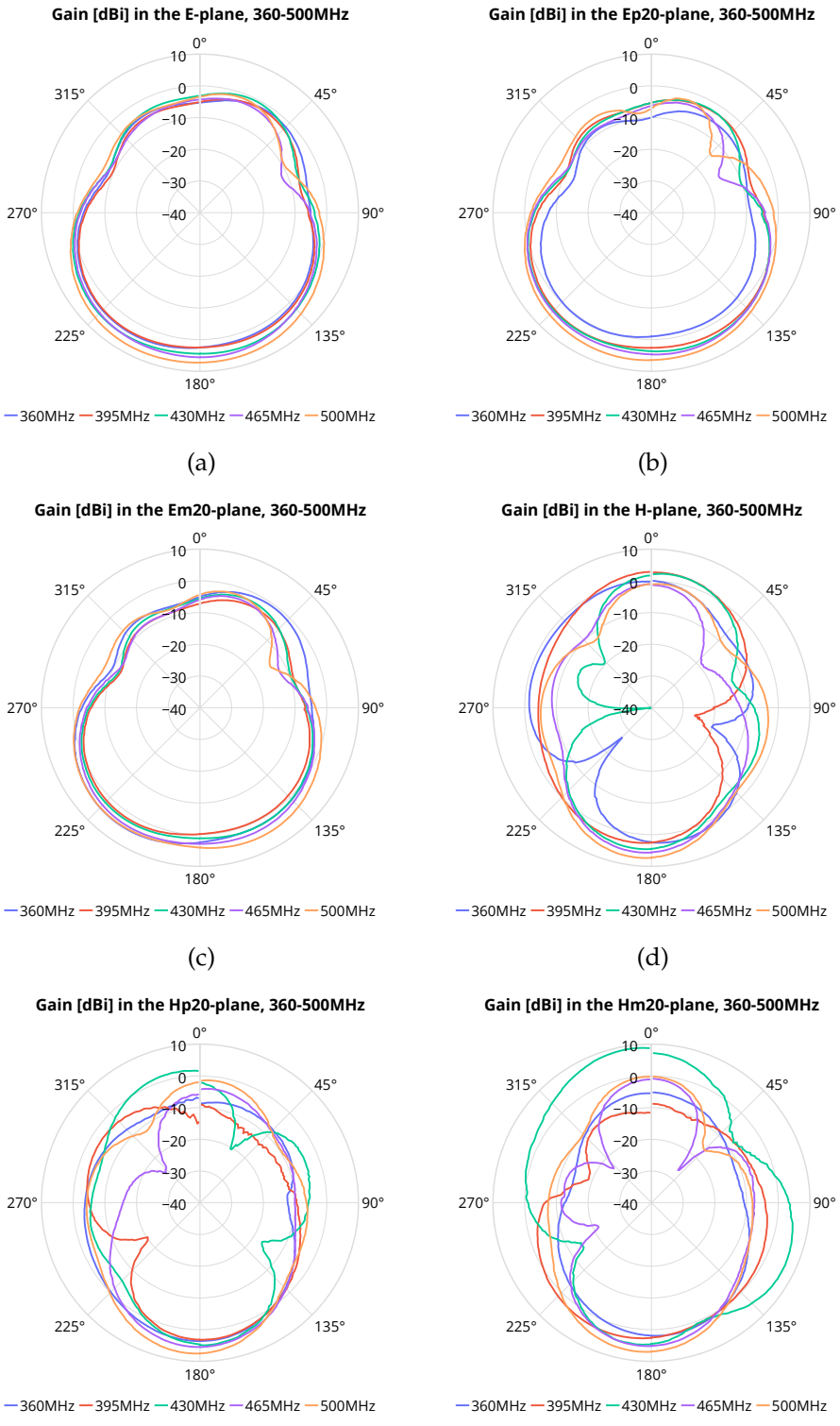

Figure A.2: These plots show the gain across all 6 cuts of the radiation pattern for the frequency range 360-500MHz. Rx: RIMFAX, Tx: LPDA antenna. The mast height of rimfax was $\approx 4m$ in the H-plane measurements and $\approx 0.82m$ in the E-plane.

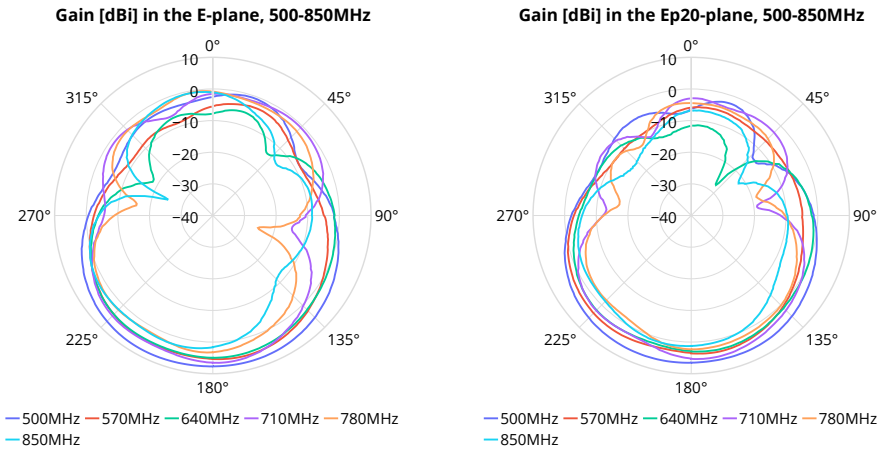

(a)

(b)

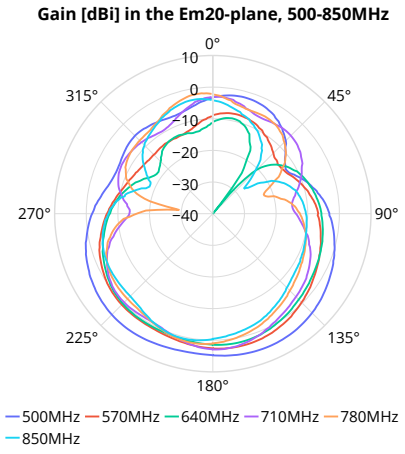

(c)

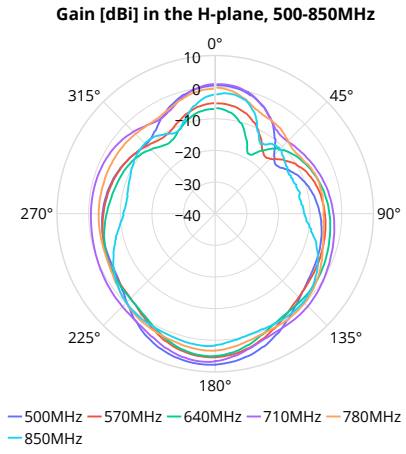

(d)

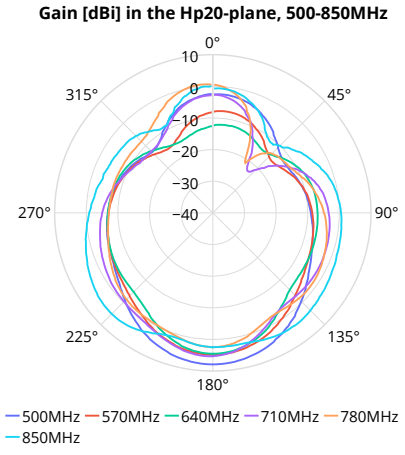

(e)

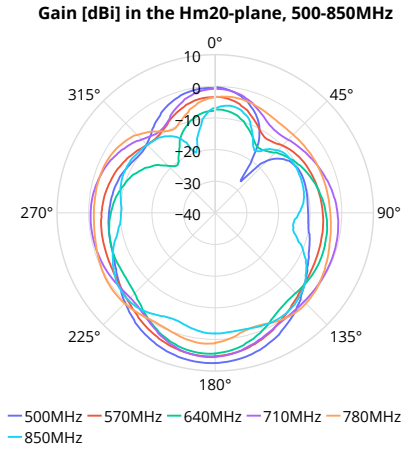

(f)

Figure A.3: These plots show the gain across all 6 cuts of the radiation pattern for the frequency range 500-850MHz. Rx: RIMFAX, Tx: LPDA antenna. The mast height of rimfax was $\approx$ 0.58m in the H-plane measurements and $\approx$ 0.28m in the E-plane.

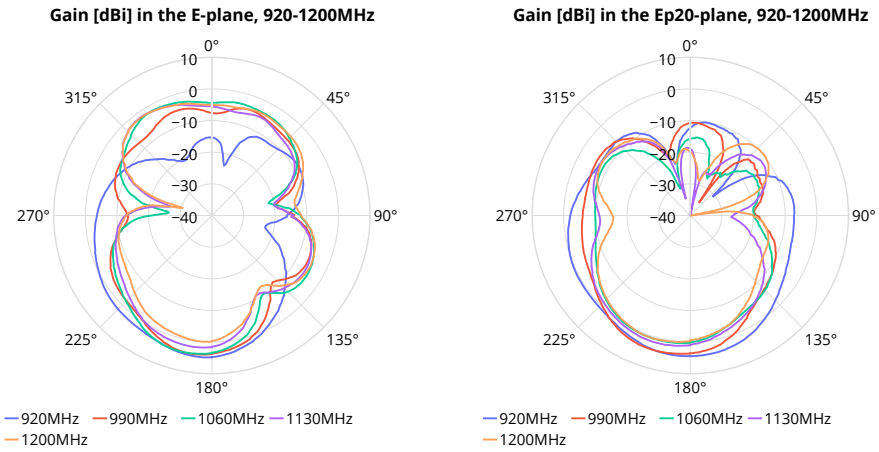

(a)

(b)

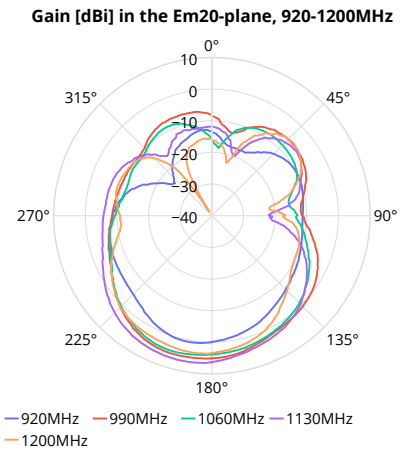

(c)

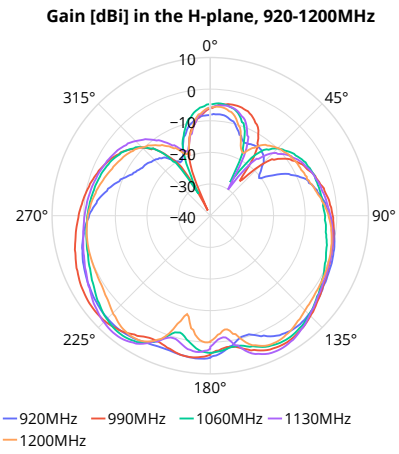

(d)

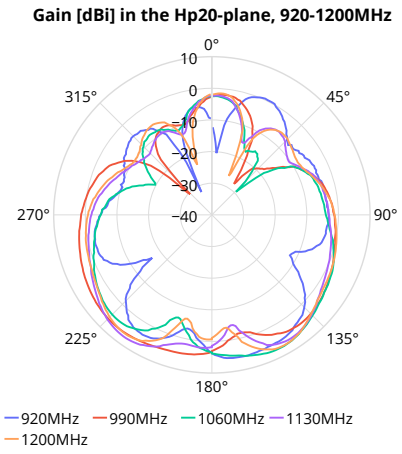

(e)

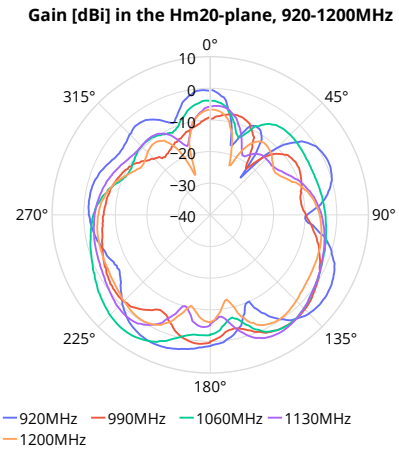

(f)

Figure A.4: These plots show the gain across all 6 cuts of the radiation pattern for the frequency range 920-1200MHz. Rx: RIMFAX, Tx: LPDA antenna. The mast height of rimfax was $\approx$ $0.58m$ in the H-plane measurements and $\approx 0.28m$ in the E-plane.

Appendix B

Spherical Harmonic charts

Frequency [MHz]	Efficiency (ξ)
150	0.754
185	0.561
220	0.404
255	0.444
290	0.603
325	0.918
360	1.41
395	1.45
430	1.55
465	1.90
500	2.67
500	2.28
570	1.27
640	1.44
710	2.30
780	1.08
850	0.874
920	1.46
990	1.26
1060	0.919
1130	0.884
1200	0.631

Table B.1: Estimates of the mean gain from the interpolated radiation pattern model (efficiency). Note that the efficiency will in reality always be less than one.

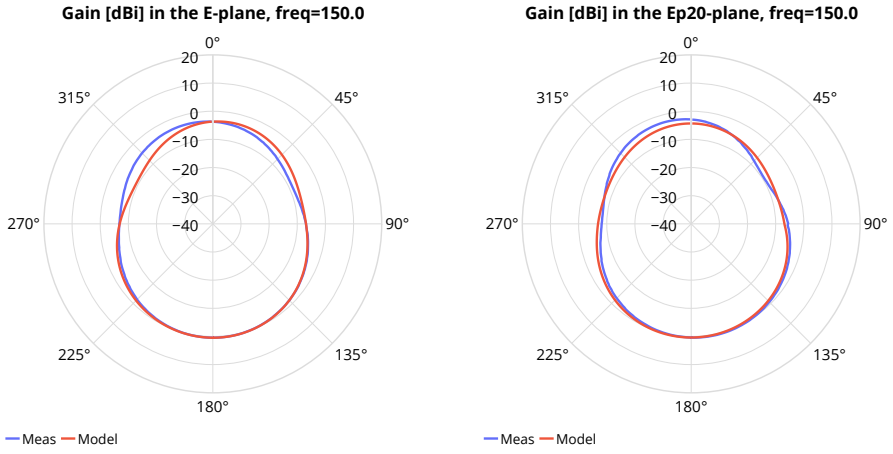

(a)

(b)

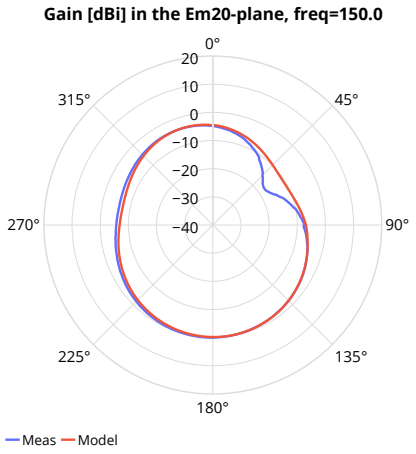

(c)

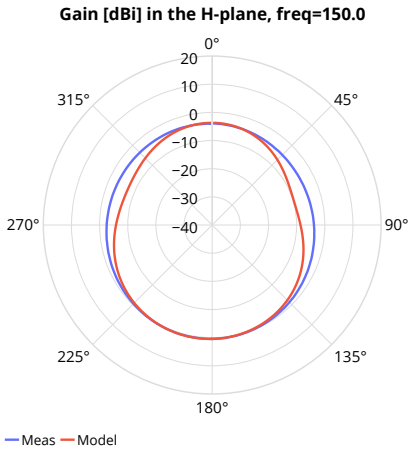

(d)

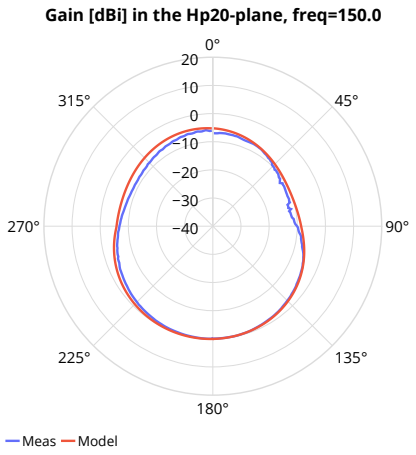

(e)

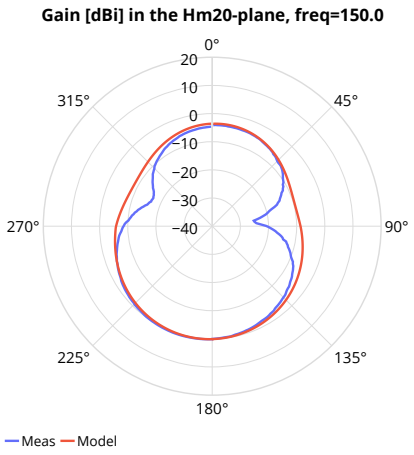

(f)

Figure B.1: These plots display comparisons between the spherical harmonic model and the input data, at 150 MHz. The order of the model is $L = 3$. Each subfigure charts the gain for a different plane.

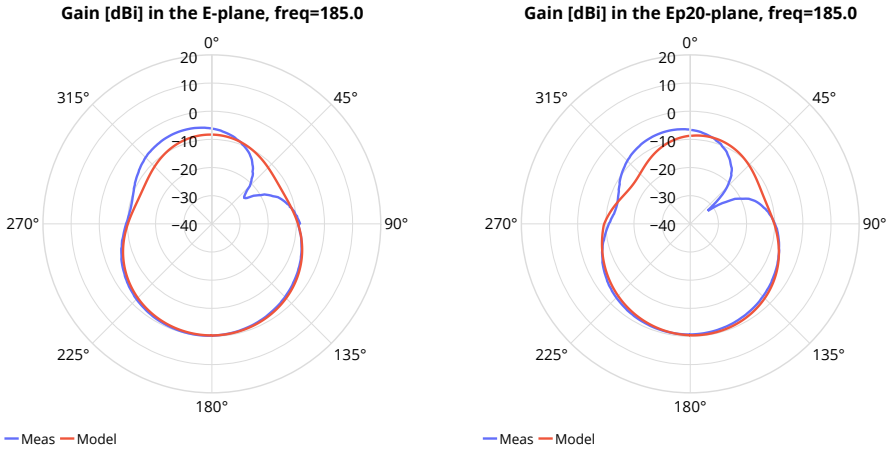

(a)

(b)

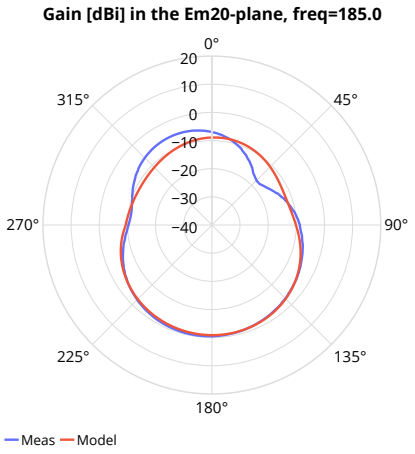

(c)

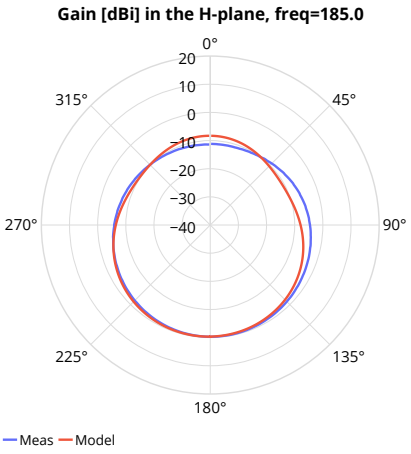

(d)

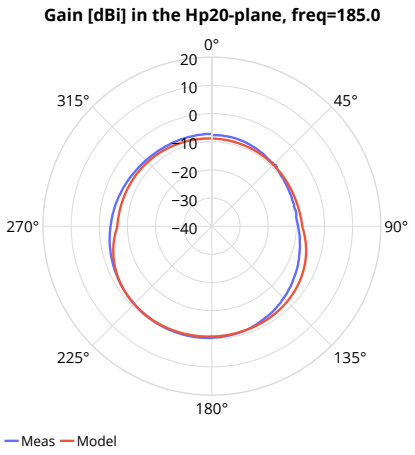

(e)

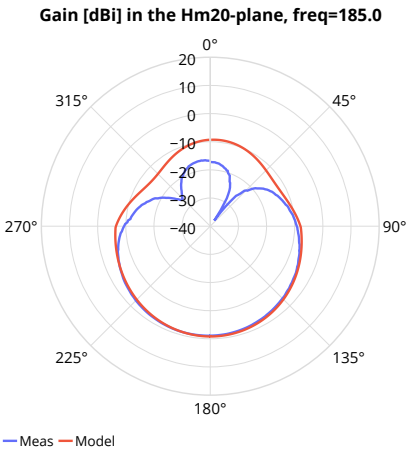

(f)

Figure B.2: These plots display comparisons between the spherical harmonic model and the input data, at 185 MHz. The order of the model is $L = 3$. Each subfigure charts the gain for a different plane.

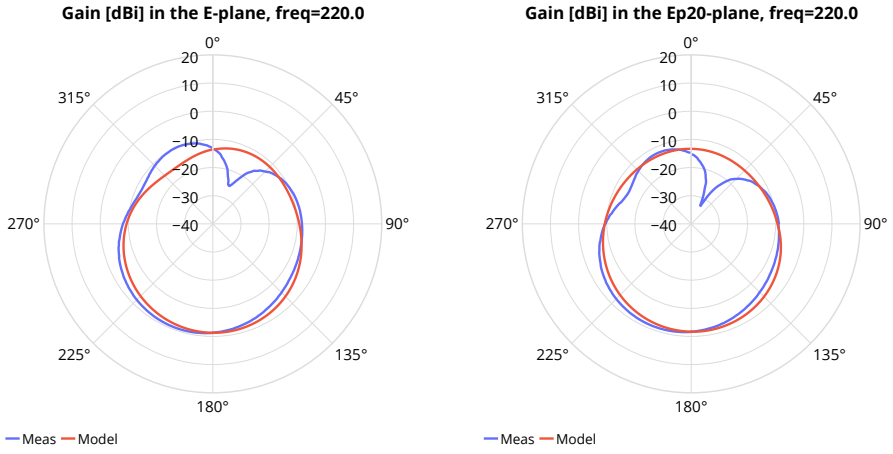

(a)

(b)

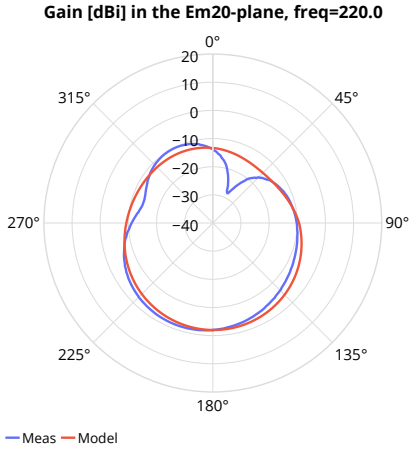

(c)

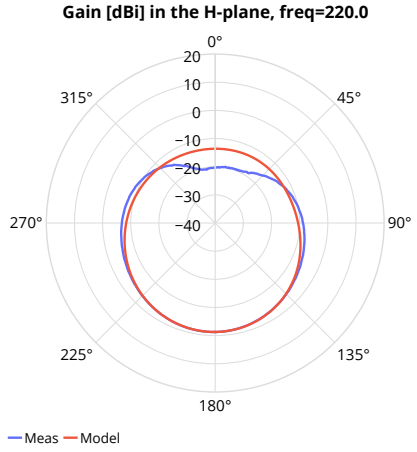

(d)

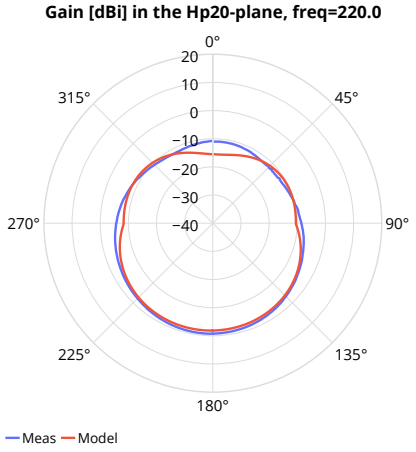

(e)

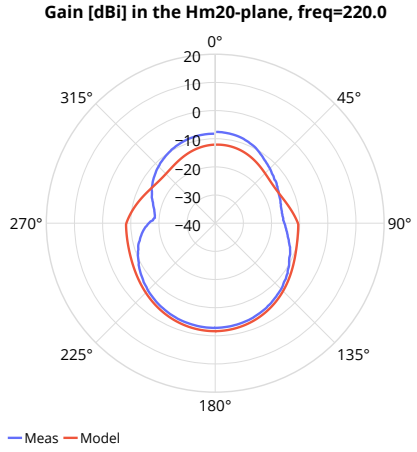

(f)

Figure B.3: These plots display comparisons between the spherical harmonic model and the input data, at 220 MHz. The order of the model is $L = 3$. Each subfigure charts the gain for a different plane.

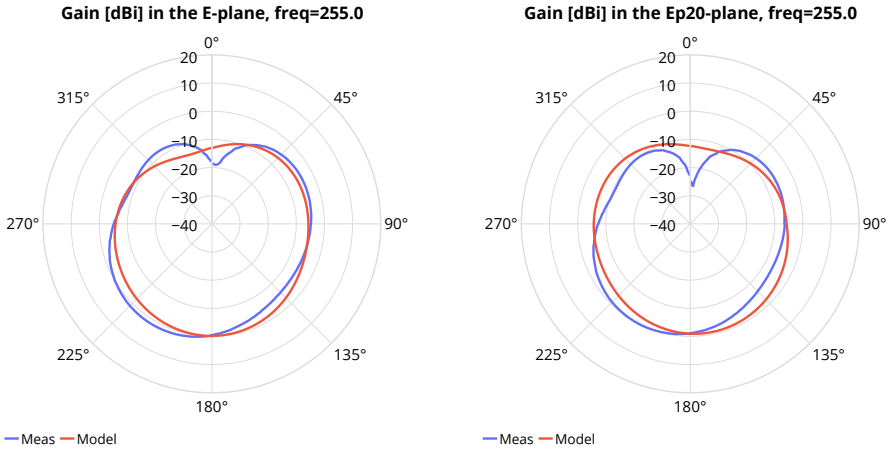

(a) (b)

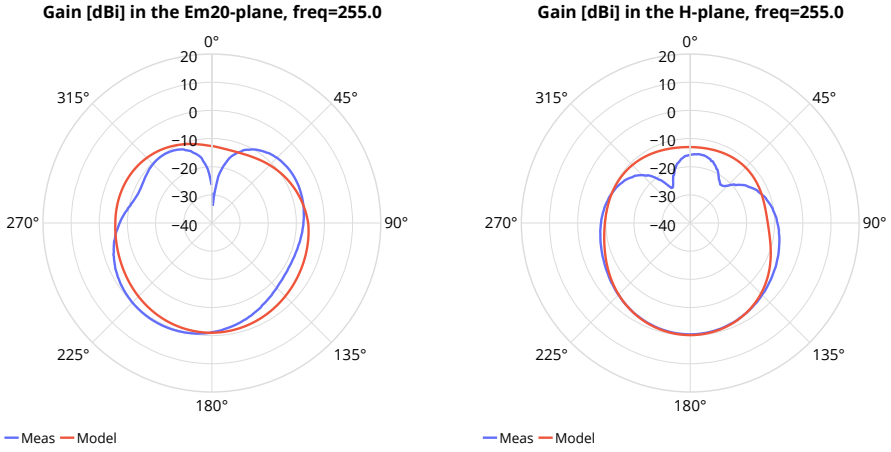

(c) (d)

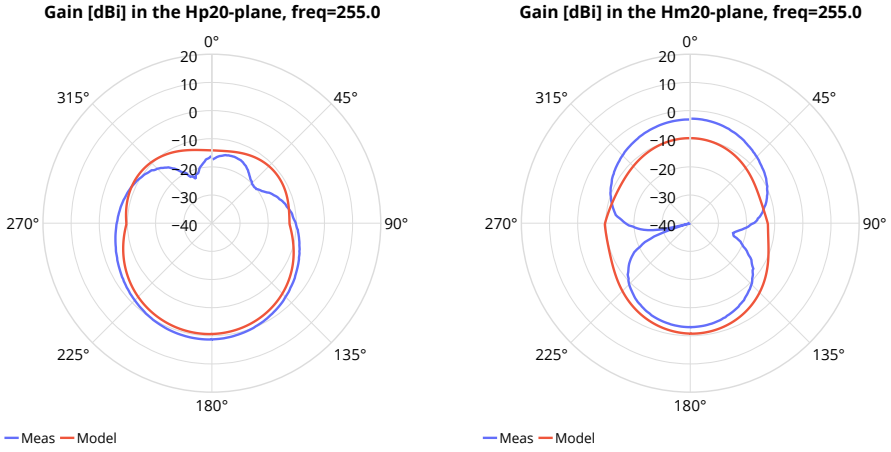

(e) (f)

Figure B.4: These plots display comparisons between the spherical harmonic model and the input data, at 255 MHz. The order of the model is $L = 3$. Each subfigure charts the gain for a different plane.

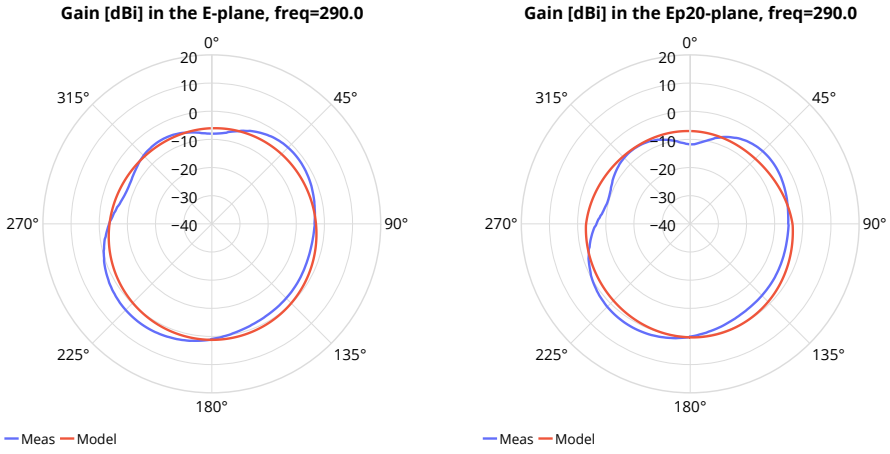

(a)

(b)

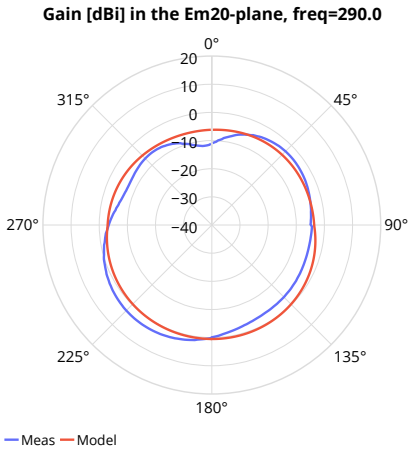

(c)

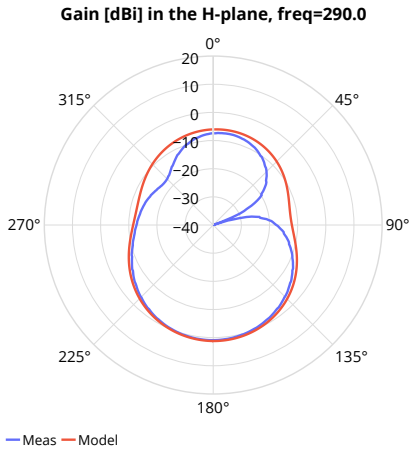

(d)

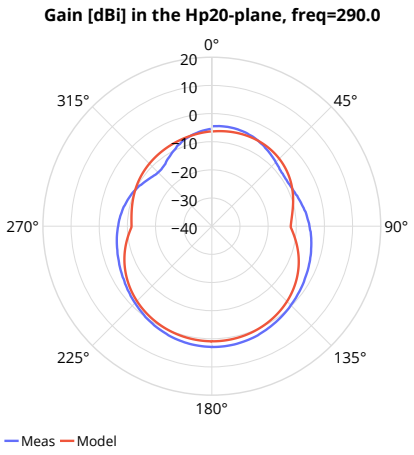

(e)

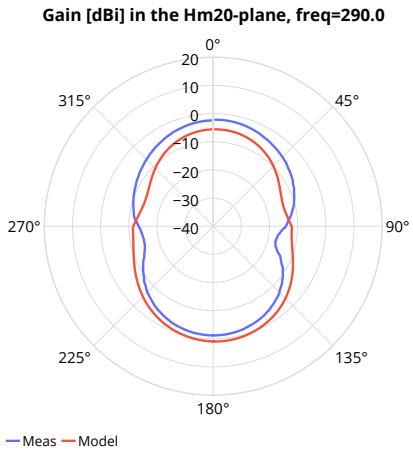

(f)

Figure B.5: These plots display comparisons between the spherical harmonic model and the input data, at 290 MHz. The order of the model is $L = 3$. Each subfigure charts the gain for a different plane.

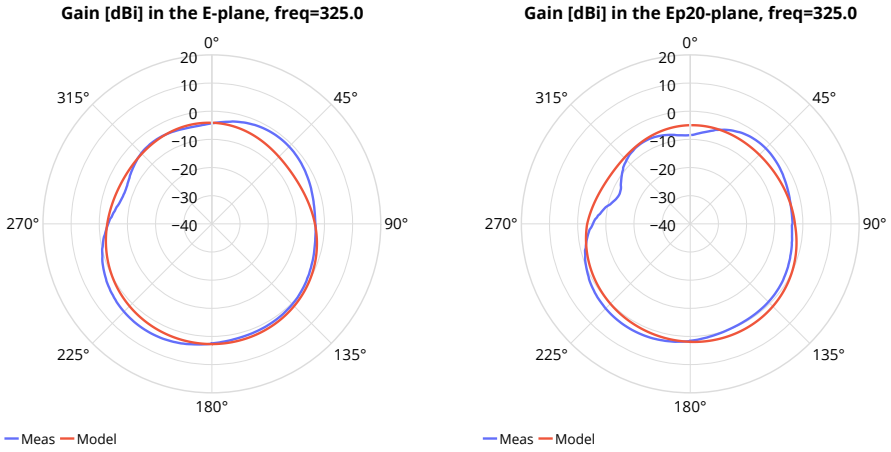

(a)

(b)

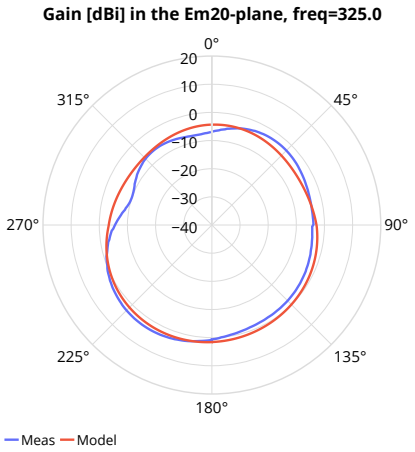

(c)

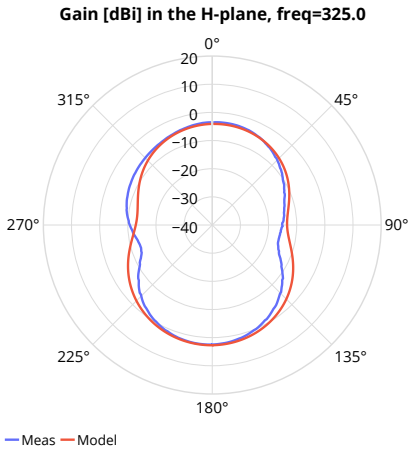

(d)

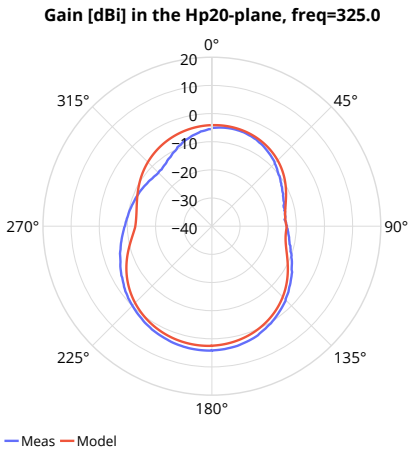

(e)

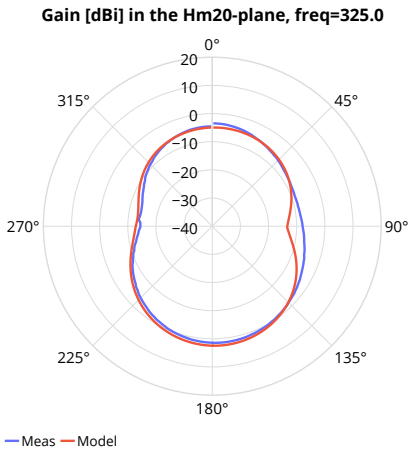

(f)

Figure B.6: These plots display comparisons between the spherical harmonic model and the input data, at 325 MHz. The order of the model is $L = 3$. Each subfigure charts the gain for a different plane.

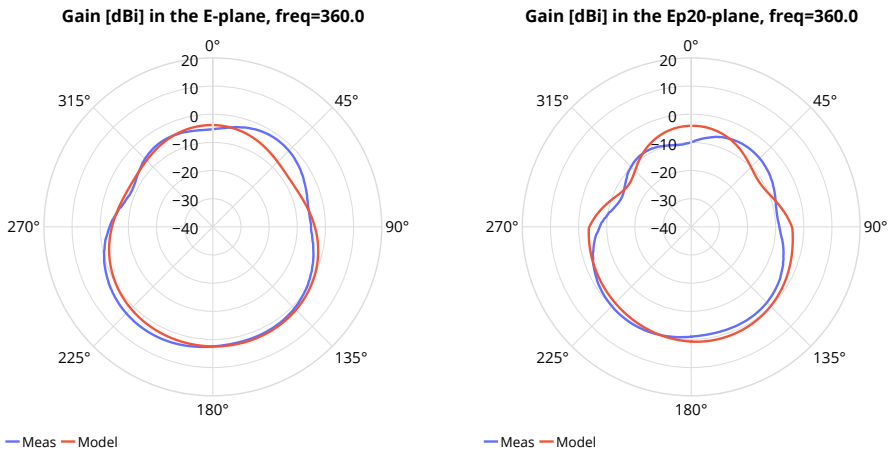

(a)

(b)

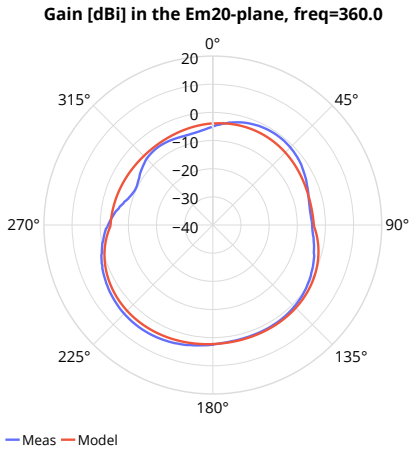

(c)

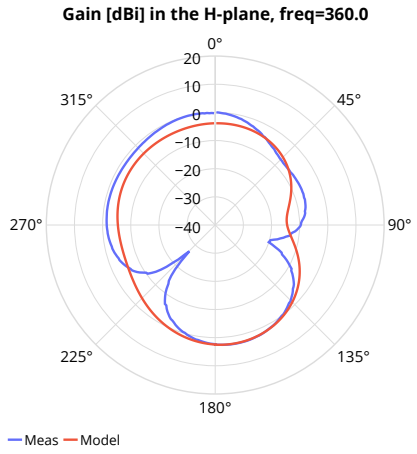

(d)

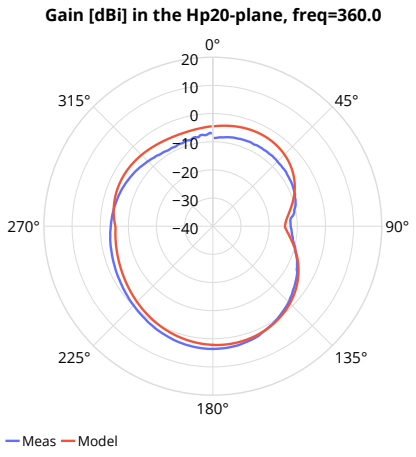

(e)

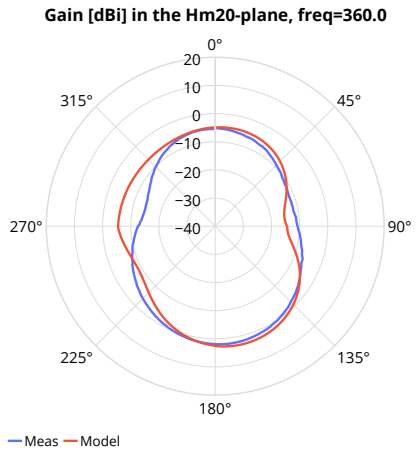

(f)

Figure B.7: These plots display comparisons between the spherical harmonic model and the input data, at 360 MHz. The order of the model is $L = 3$. Each subfigure charts the gain for a different plane.

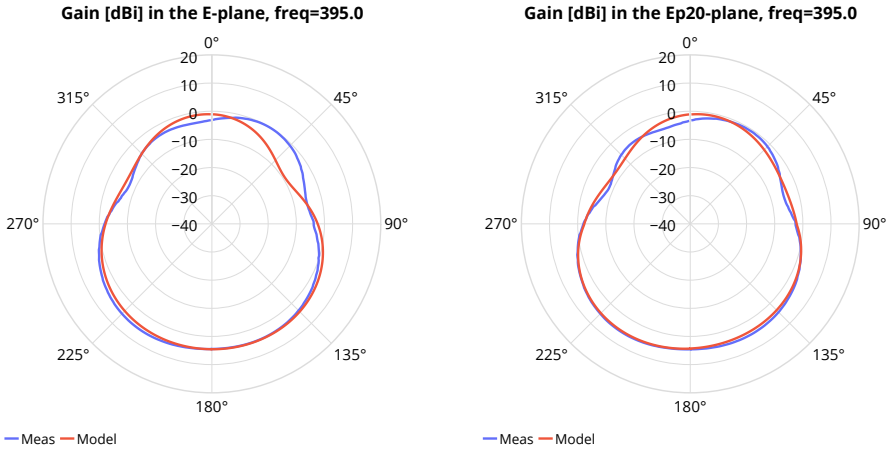

(a) (b)

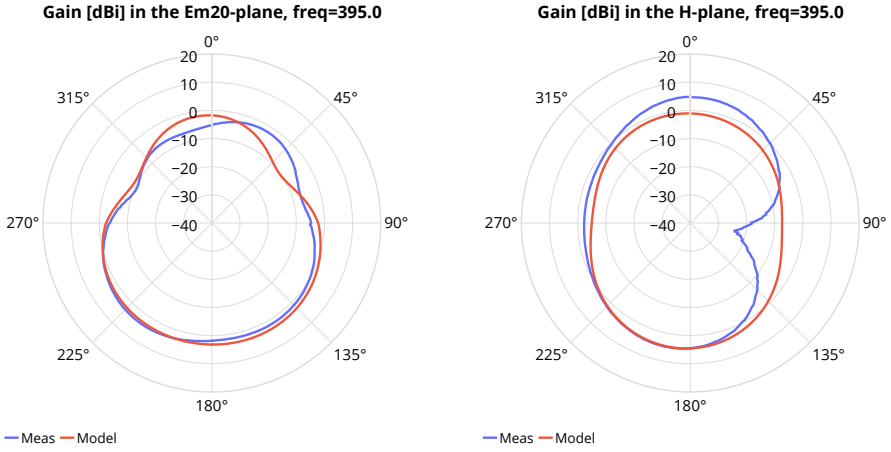

(c) (d)

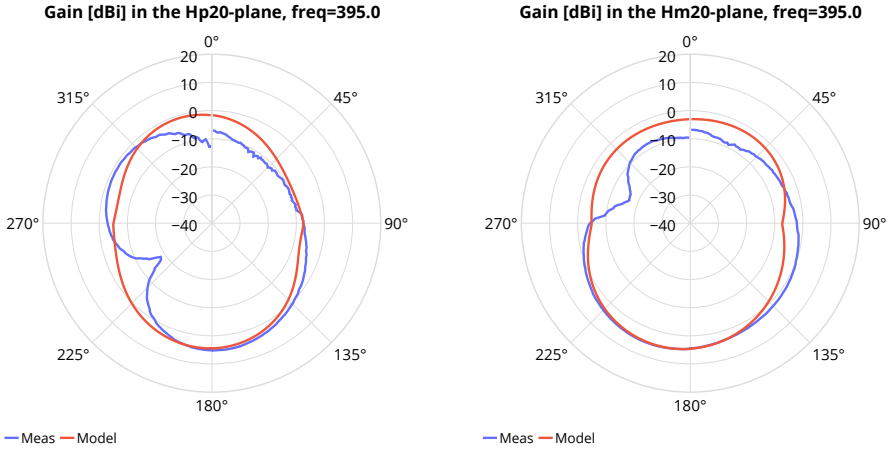

(e) (f)

Figure B.8: These plots display comparisons between the spherical harmonic model and the input data, at 395 MHz. The order of the model is $L = 3$. Each subfigure charts the gain for a different plane.

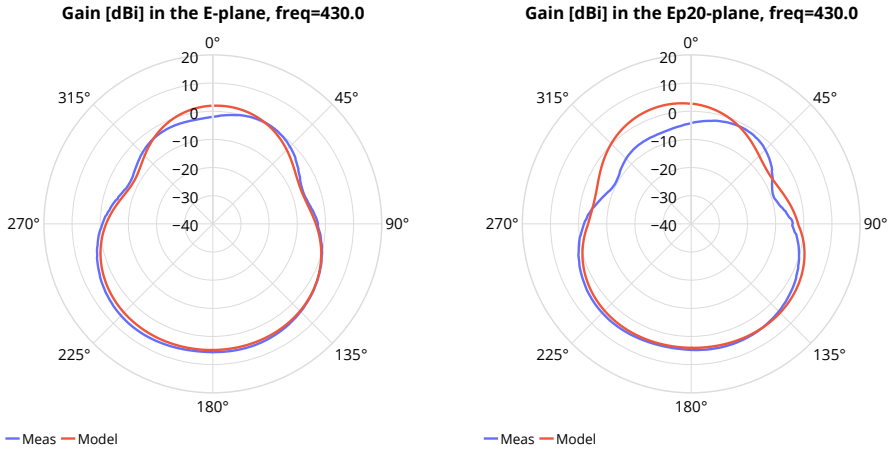

(a)

(b)

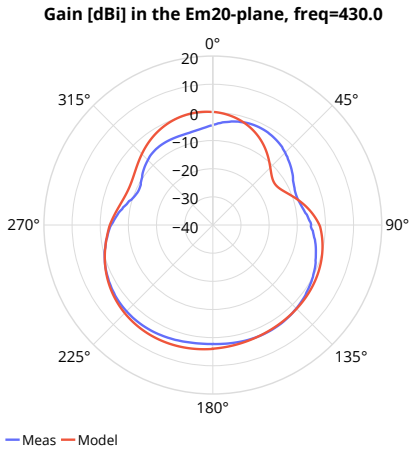

(c)

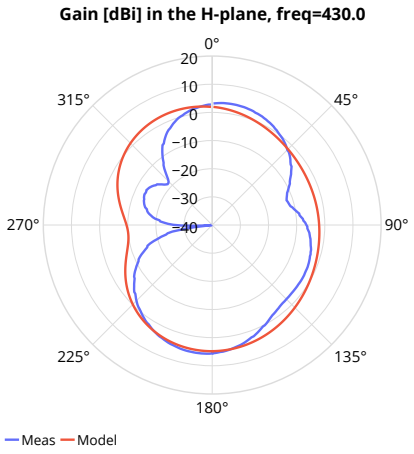

(d)

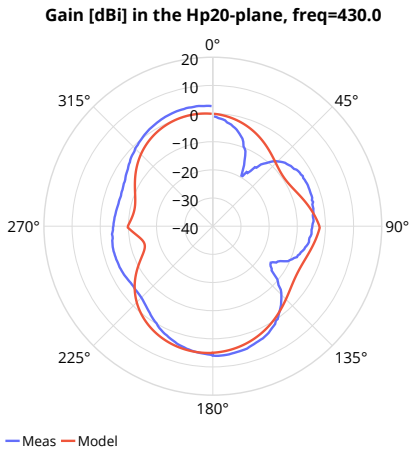

(e)

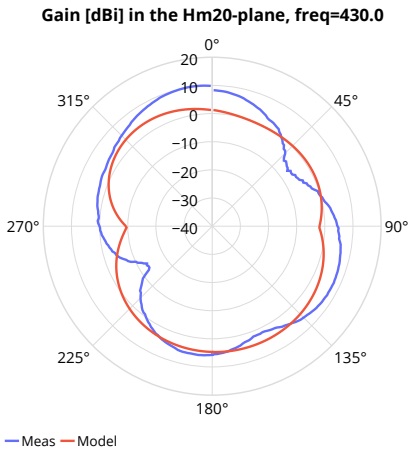

(f)

Figure B.9: These plots display comparisons between the spherical harmonic model and the input data, at 430 MHz. The order of the model is $L = 3$. Each subfigure charts the gain for a different plane.

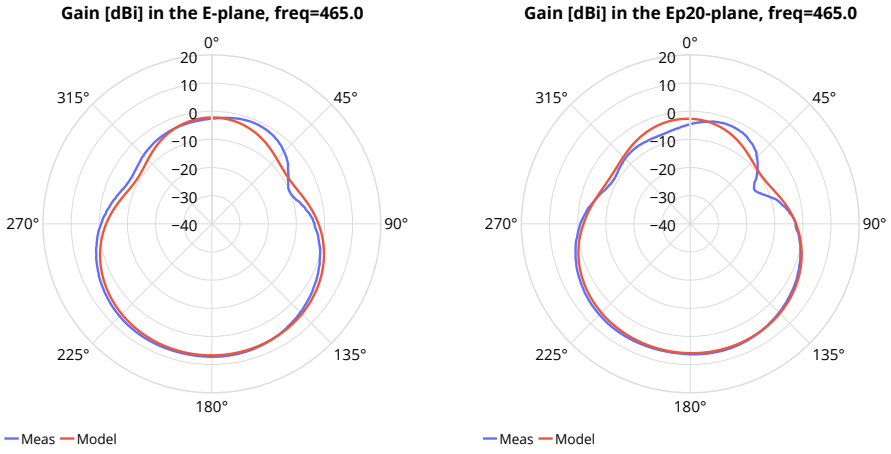

(a) (b)

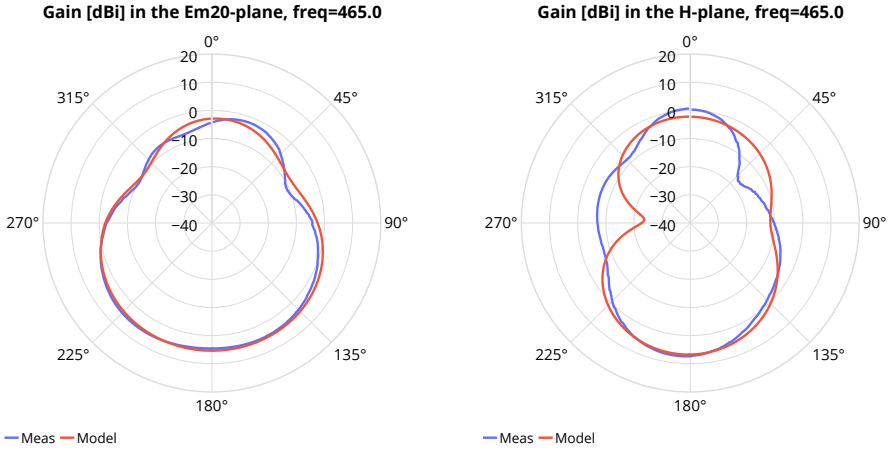

(c) (d)

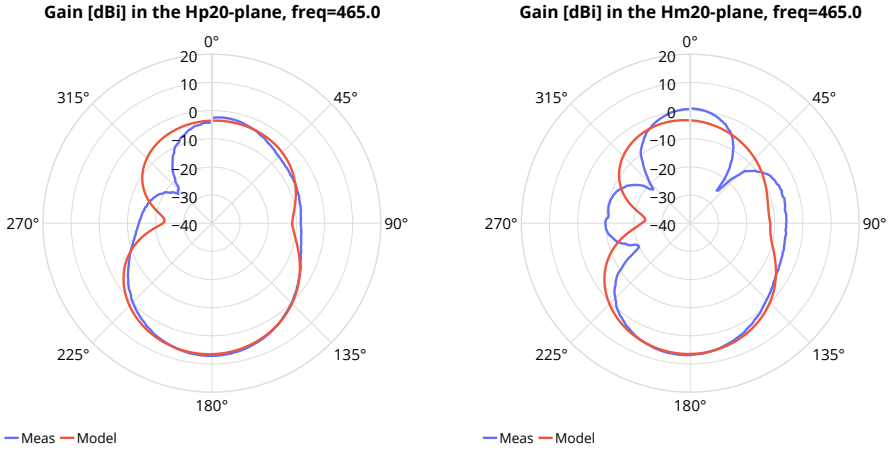

(e) (f)

Figure B.10: These plots display comparisons between the spherical harmonic model and the input data, at 465 MHz. The order of the model is $L = 3$. Each subfigure charts the gain for a different plane.

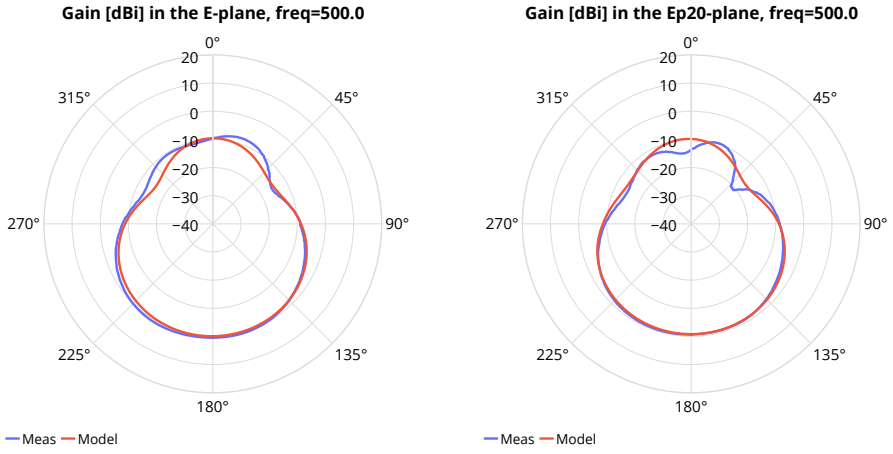

(a)

(b)

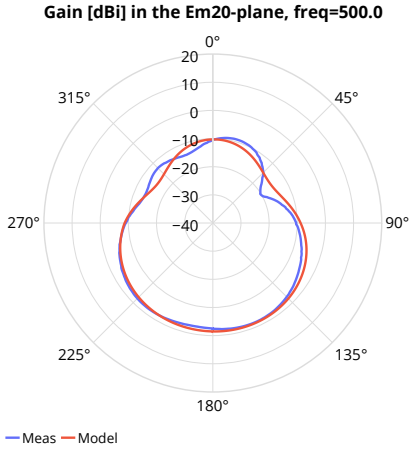

(c)

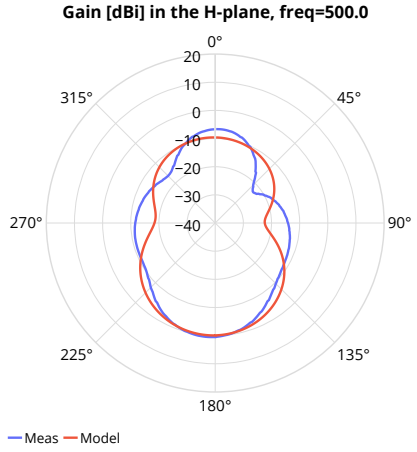

(d)

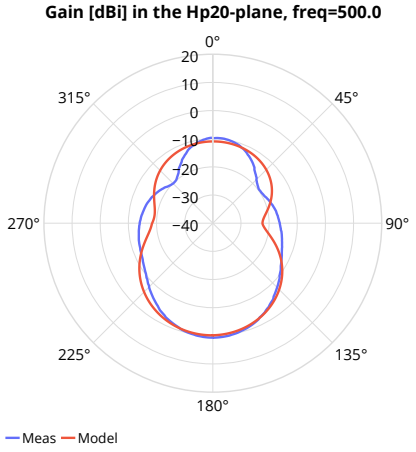

(e)

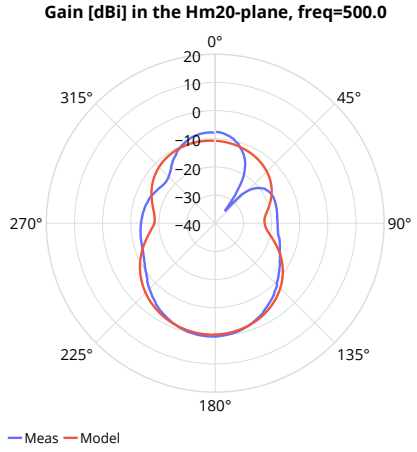

(f)

Figure B.11: These plots display comparisons between the spherical harmonic model and the input data, at 500 MHz. The order of the model is $L = 3$. Each subfigure charts the gain for a different plane.

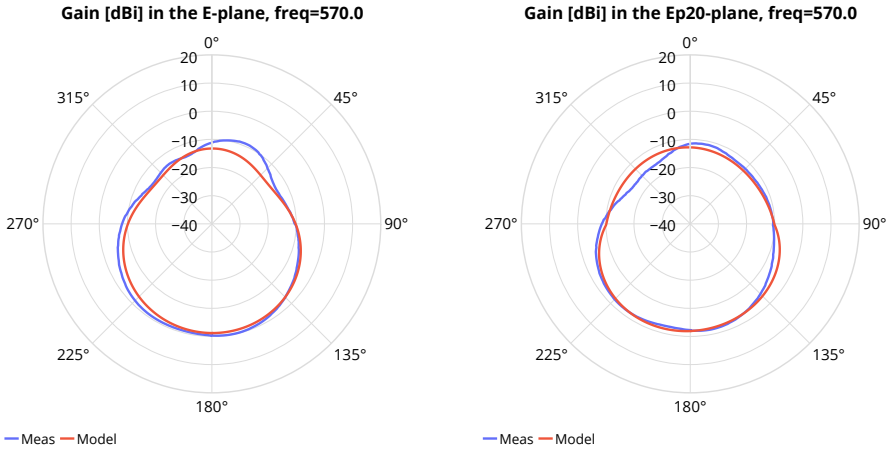

(a)

(b)

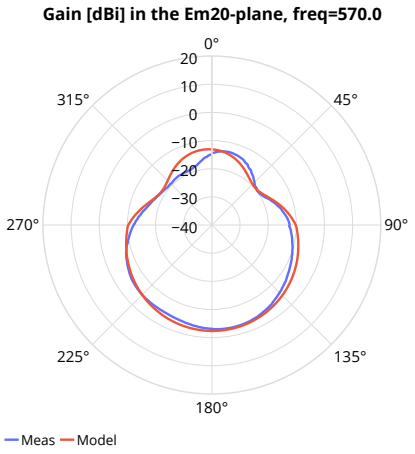

(c)

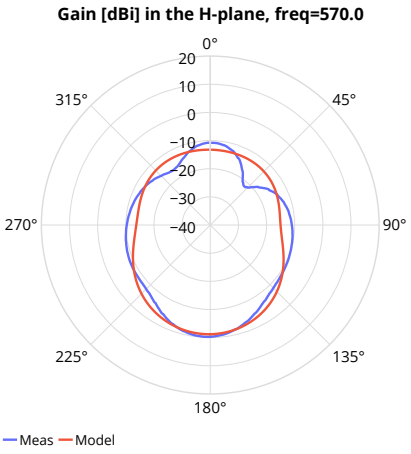

(d)

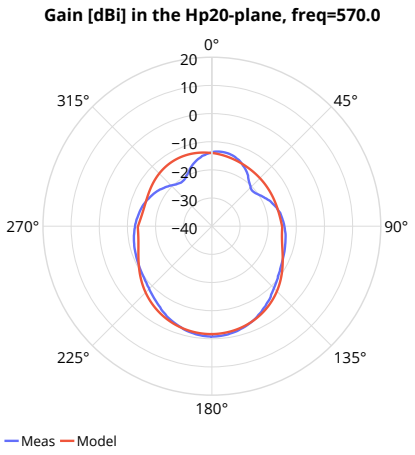

(e)

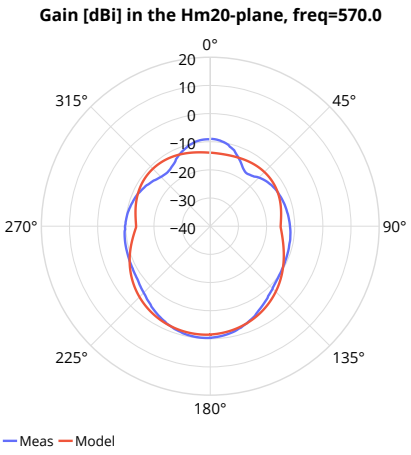

(f)

Figure B.12: These plots display comparisons between the spherical harmonic model and the input data, at 570 MHz. The order of the model is $L = 3$. Each subfigure charts the gain for a different plane.

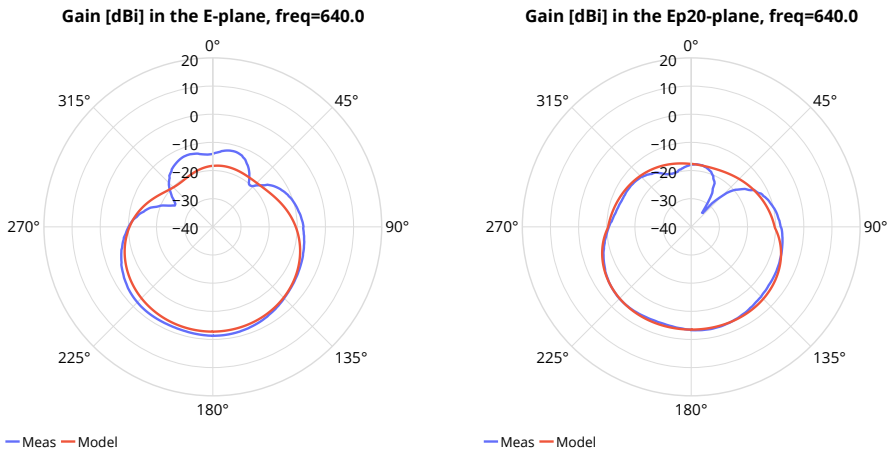

(a)

(b)

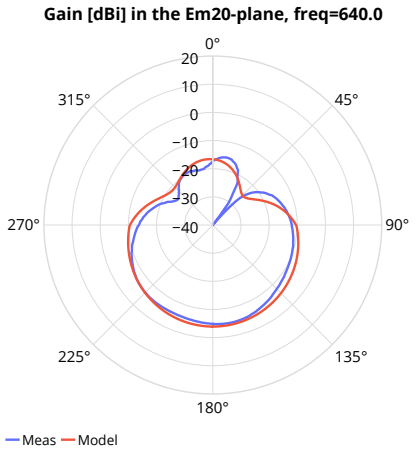

(c)

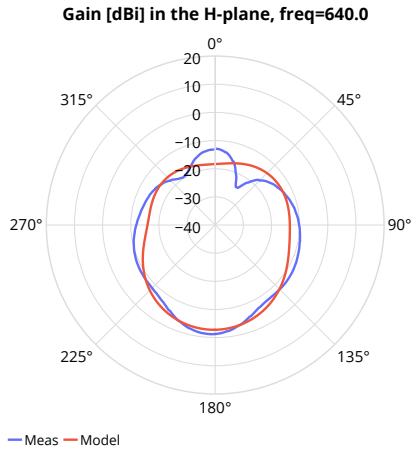

(d)

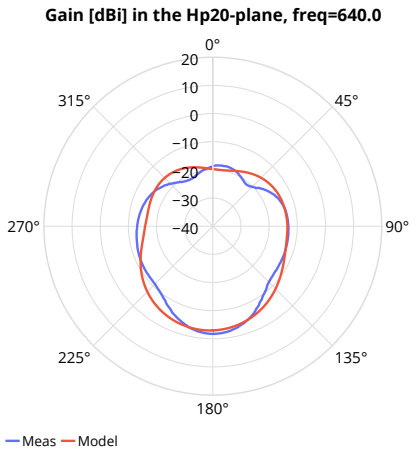

(e)

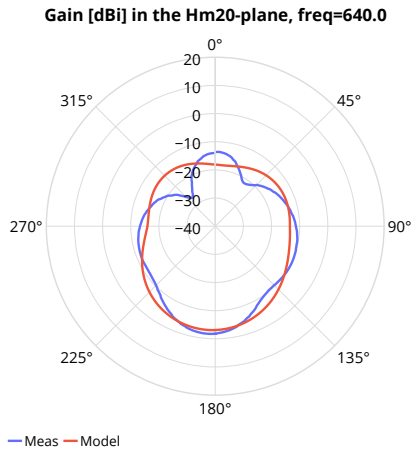

(f)

Figure B.13: These plots display comparisons between the spherical harmonic model and the input data, at 640 MHz. The order of the model is $L = 3$. Each subfigure charts the gain for a different plane.

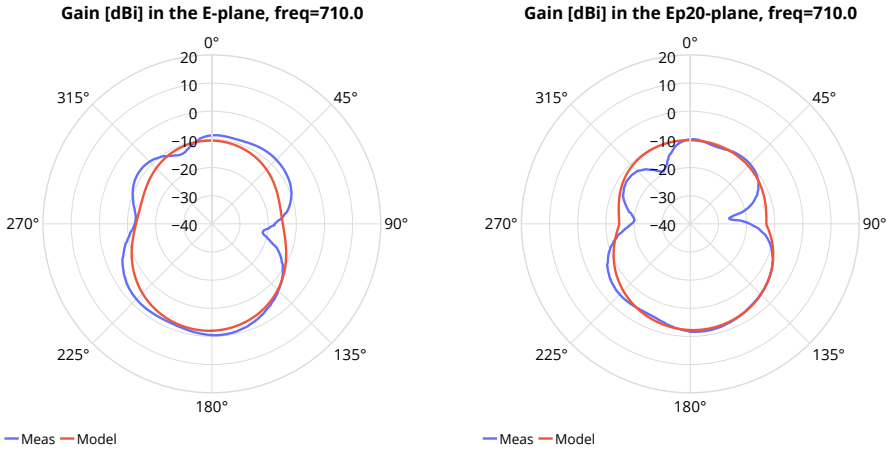

(a)

(b)

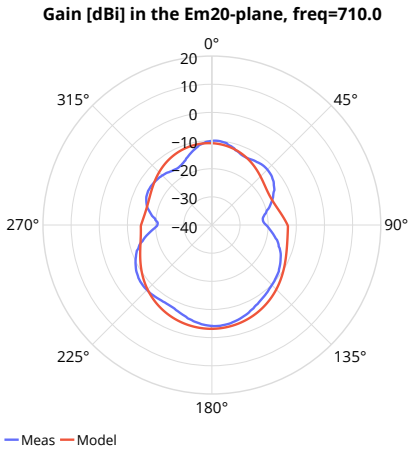

(c)

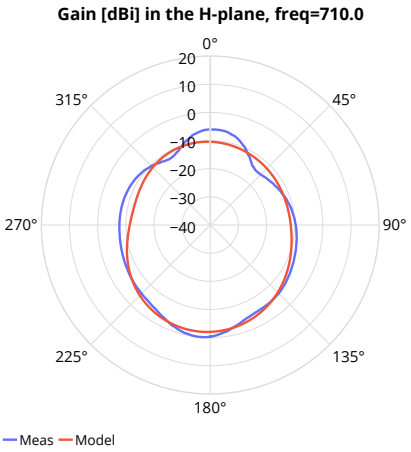

(d)

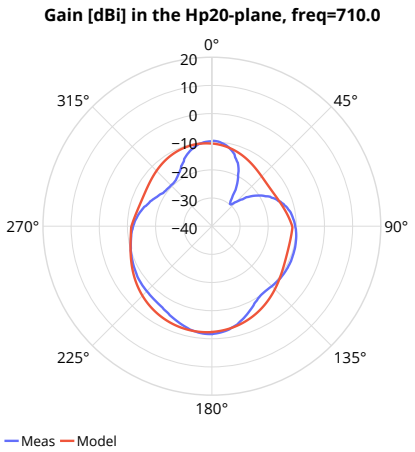

(e)

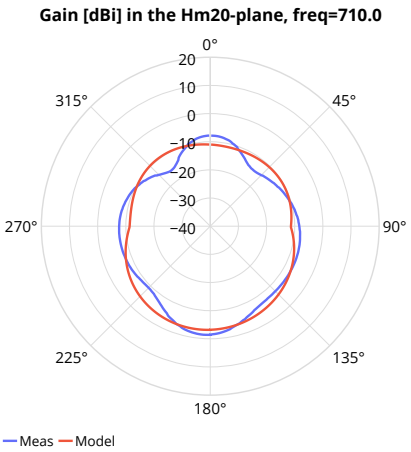

(f)

Figure B.14: These plots display comparisons between the spherical harmonic model and the input data, at 710 MHz. The order of the model is $L = 3$. Each subfigure charts the gain for a different plane.

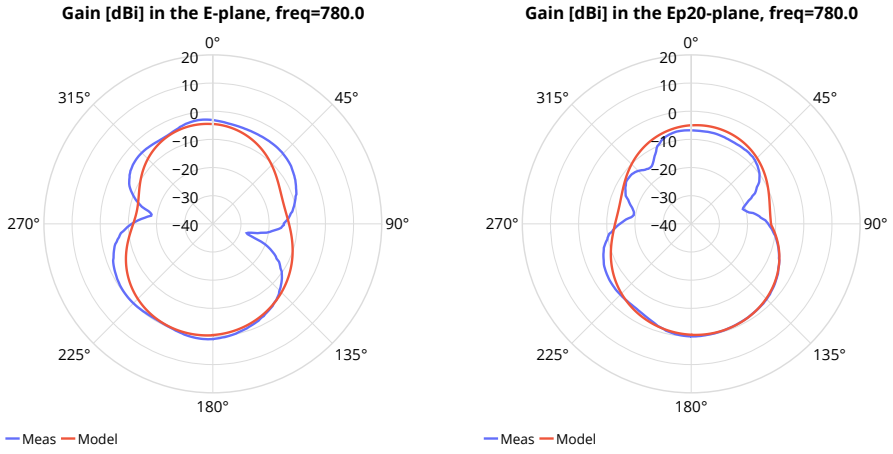

(a)

(b)

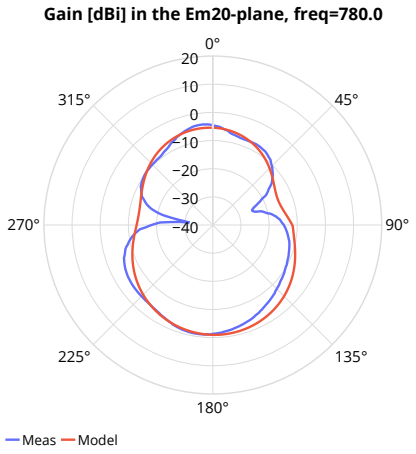

(c)

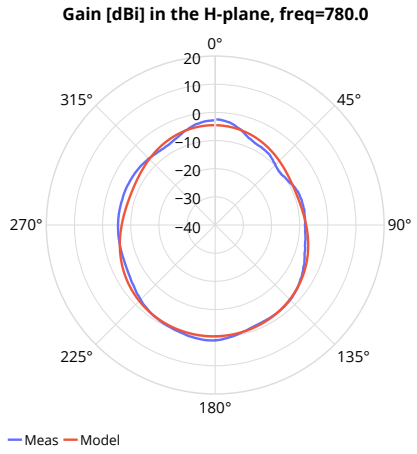

(d)

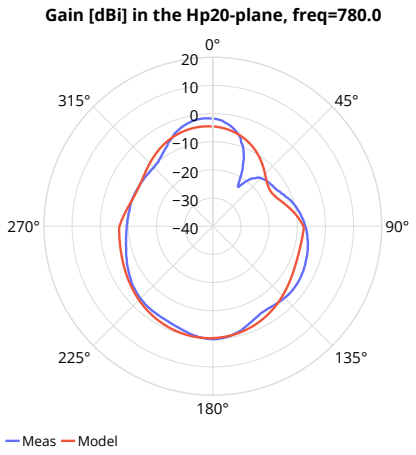

(e)

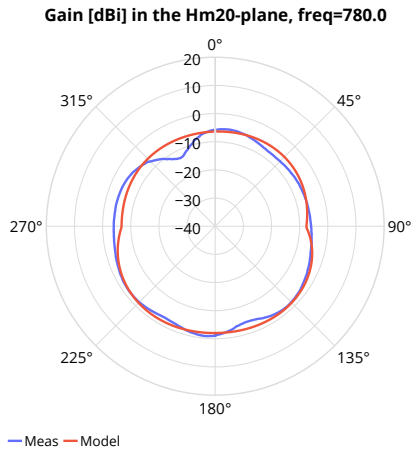

(f)

Figure B.15: These plots display comparisons between the spherical harmonic model and the input data, at 780 MHz. The order of the model is $L = 3$. Each subfigure charts the gain for a different plane.

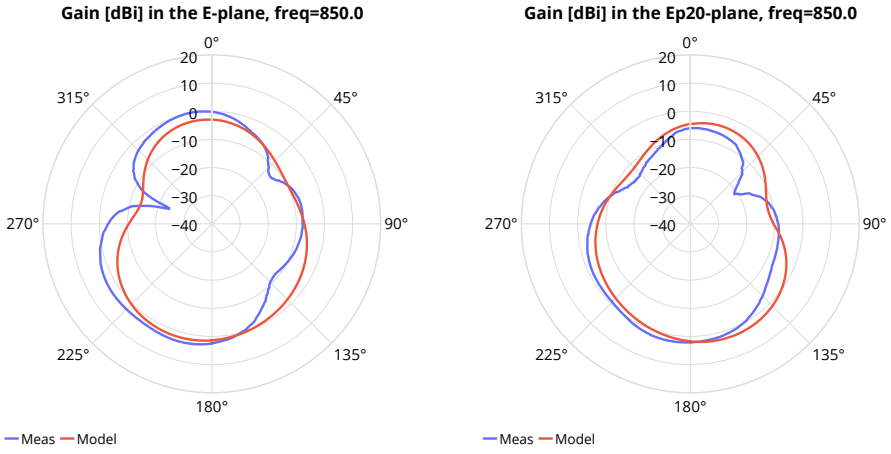

(a)

(b)

(c)

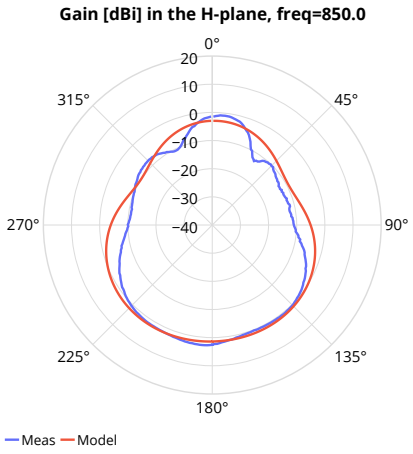

(d)

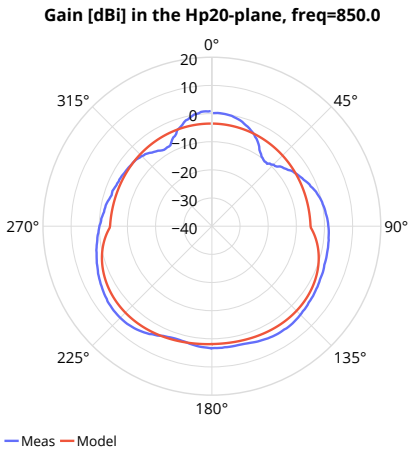

(e)

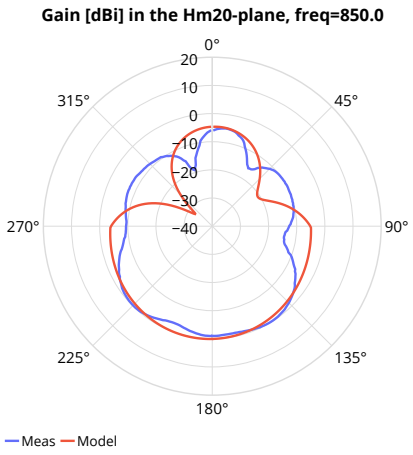

(f)

Figure B.16: These plots display comparisons between the spherical harmonic model and the input data, at 850 MHz. The order of the model is $L = 3$. Each subfigure charts the gain for a different plane.

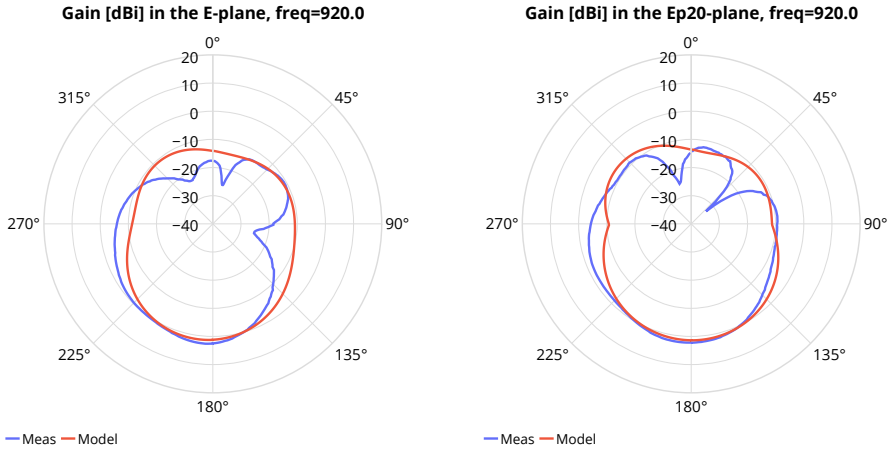

(a)

(b)

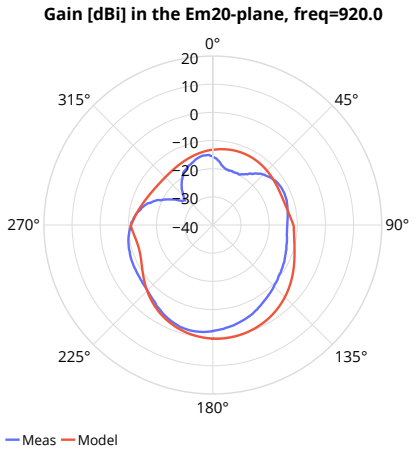

(c)

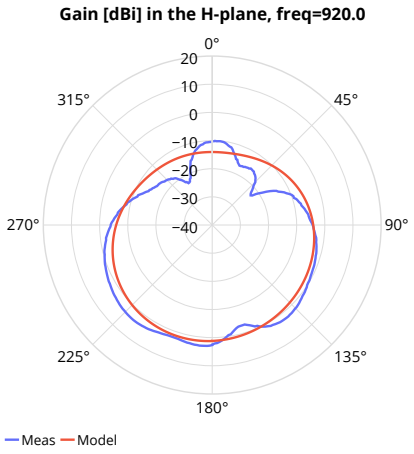

(d)

(e)

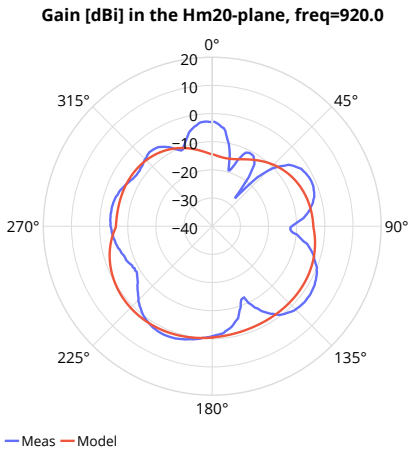

(f)

Figure B.17: These plots display comparisons between the spherical harmonic model and the input data, at 920 MHz. The order of the model is $L = 3$. Each subfigure charts the gain for a different plane.

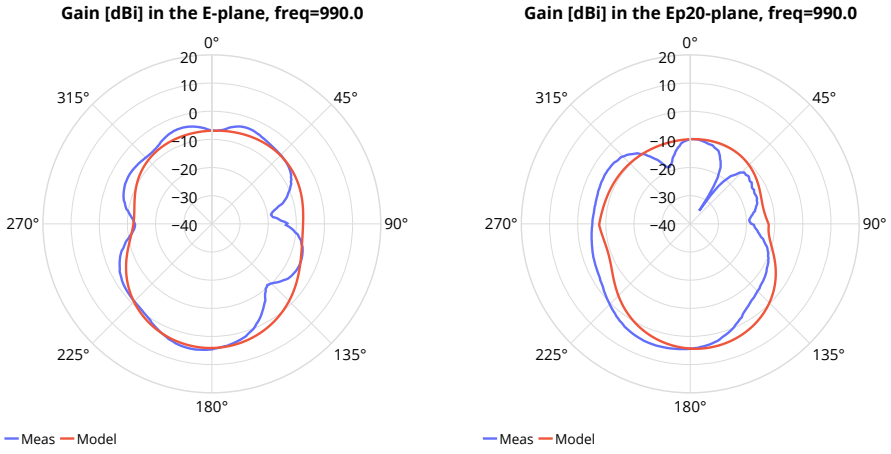

(a) (b)

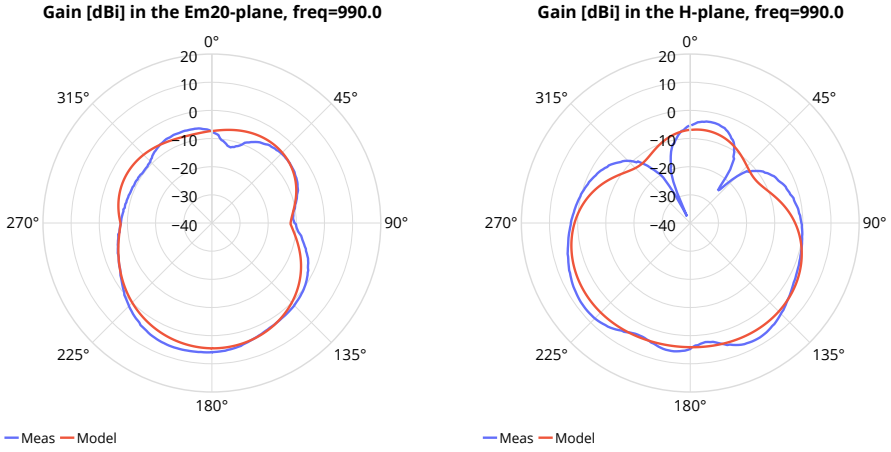

(c) (d)

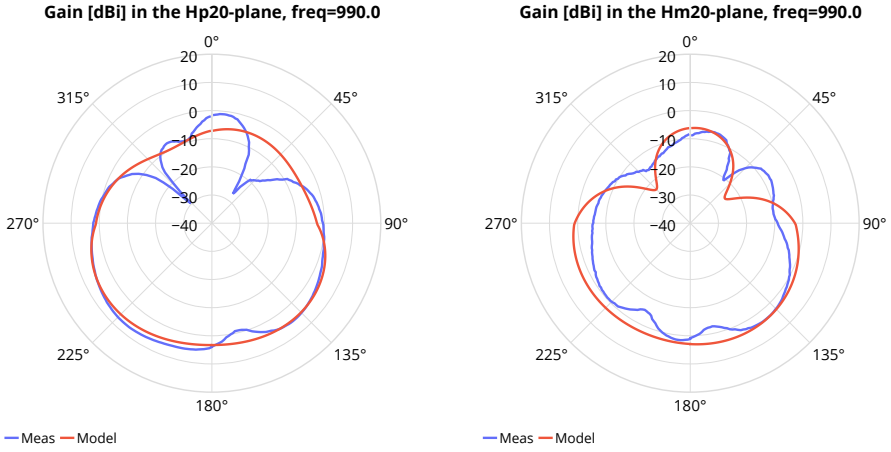

(e) (f)

Figure B.18: These plots display comparisons between the spherical harmonic model and the input data, at 990 MHz. The order of the model is $L = 3$. Each subfigure charts the gain for a different plane.

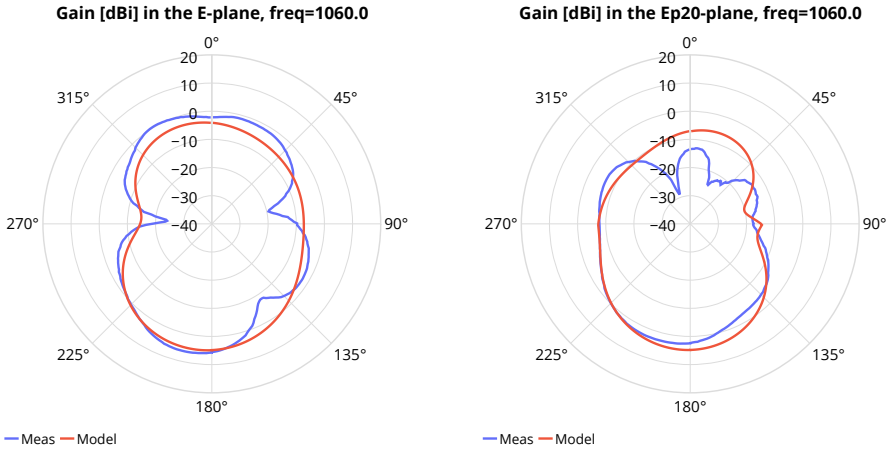

(a)

(b)

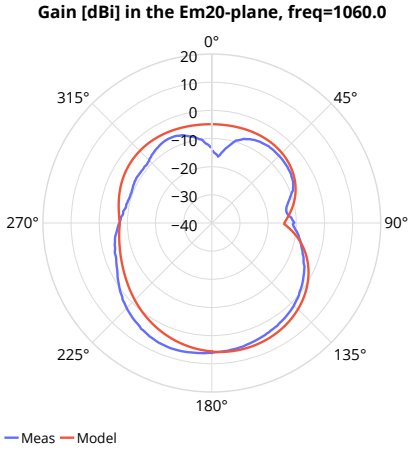

(c)

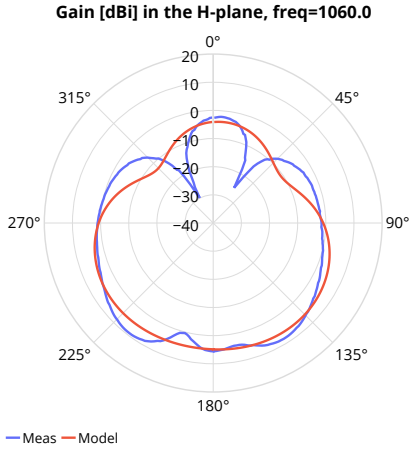

(d)

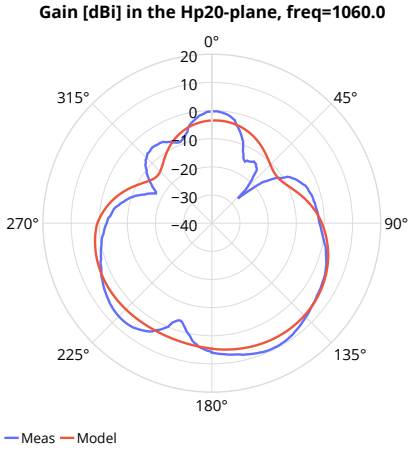

(e)

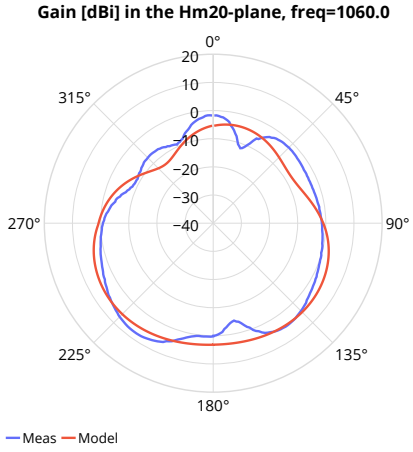

(f)

Figure B.19: These plots display comparisons between the spherical harmonic model and the input data, at 1060 MHz. The order of the model is $L = 3$. Each subfigure charts the gain for a different plane.

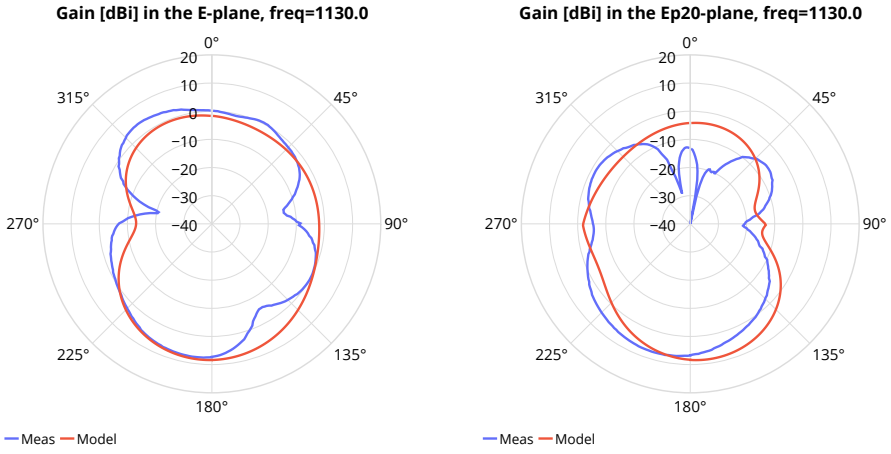

(a)

(b)

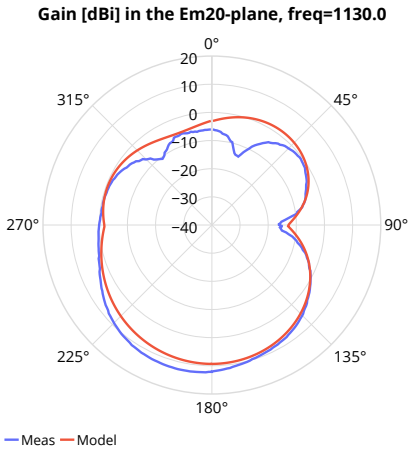

(c)

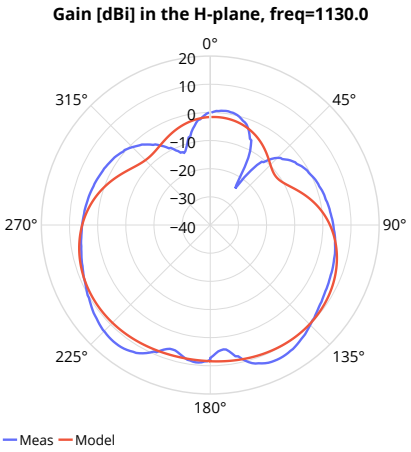

(d)

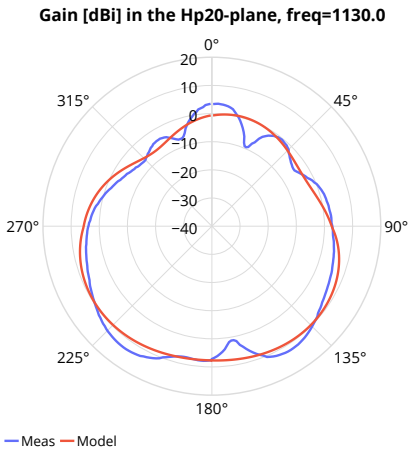

(e)

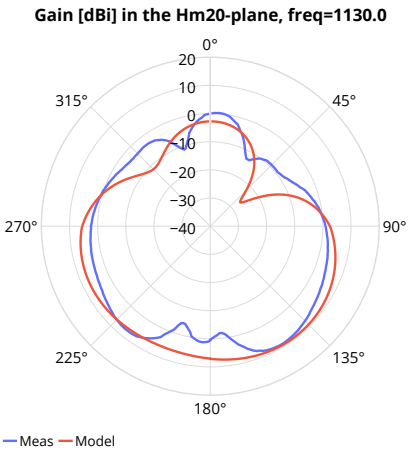

(f)

Figure B.20: These plots display comparisons between the spherical harmonic model and the input data, at 1130 MHz. The order of the model is $L = 3$. Each subfigure charts the gain for a different plane.

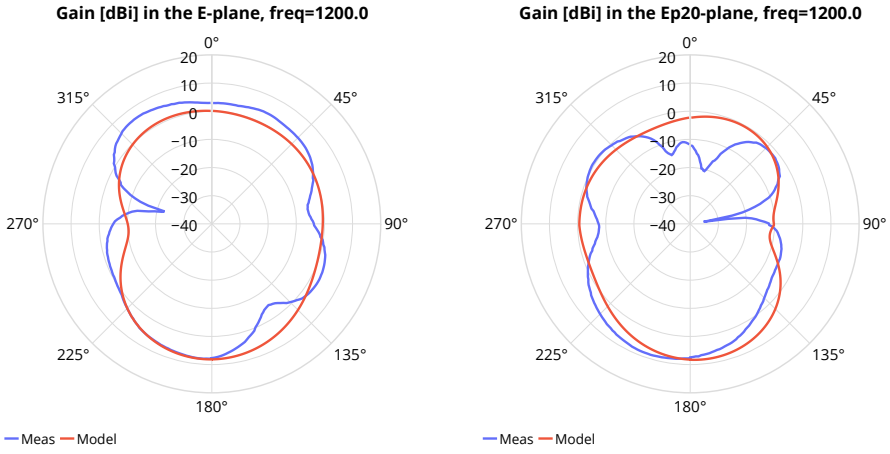

(a)

(b)

(c)

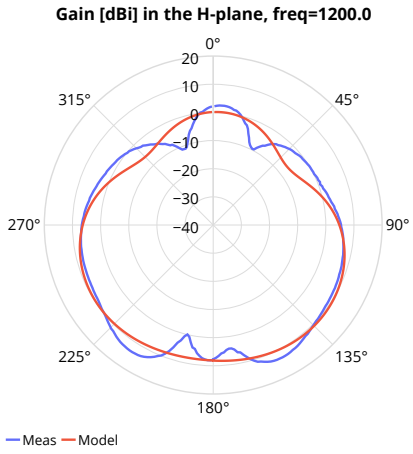

(d)

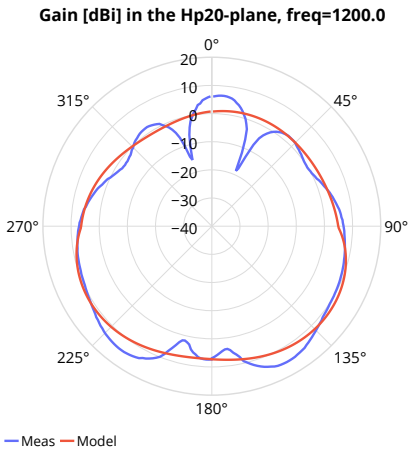

(e)

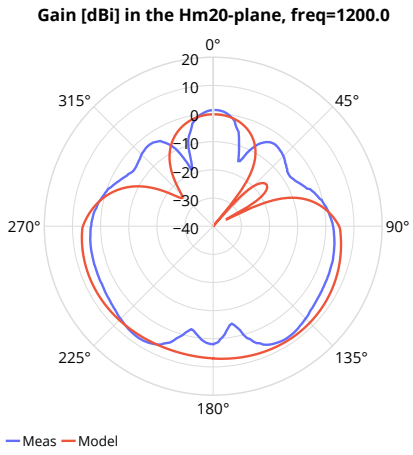

(f)

Figure B.21: These plots display comparisons between the spherical harmonic model and the input data, at 1200 MHz. The order of the model is $L = 3$. Each subfigure charts the gain for a different plane.

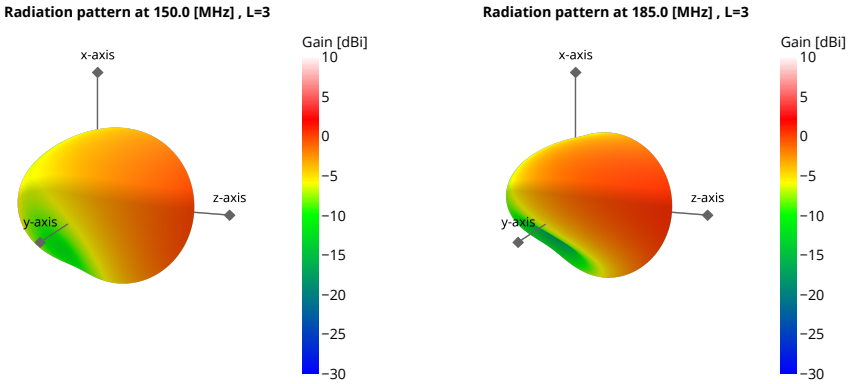

(a)

(b)

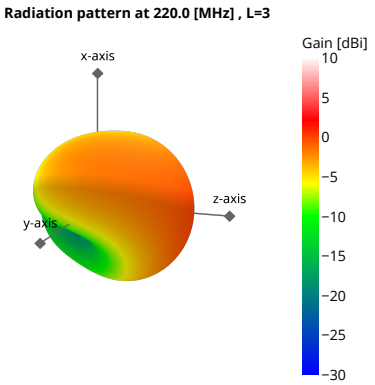

(c)

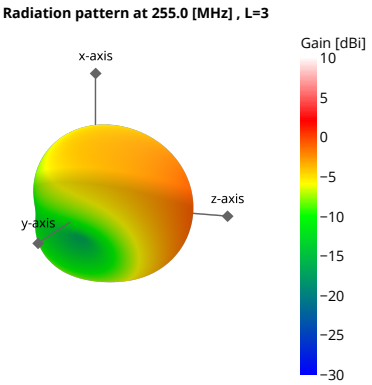

(d)

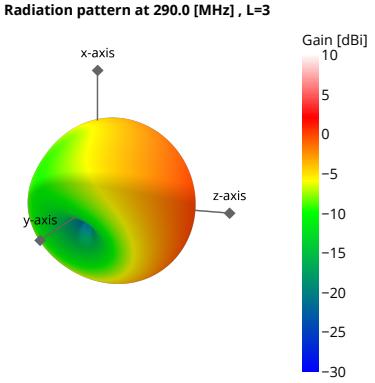

(e)

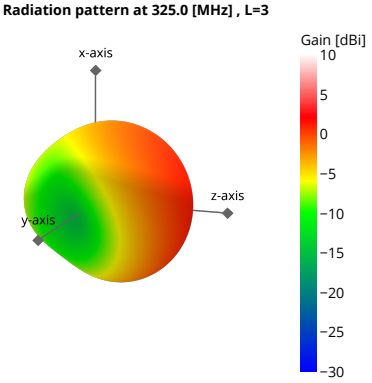

(f)

Figure B.22: These charts display the interpolated radiation patterns at frequencies 150-325 MHz and L=3.

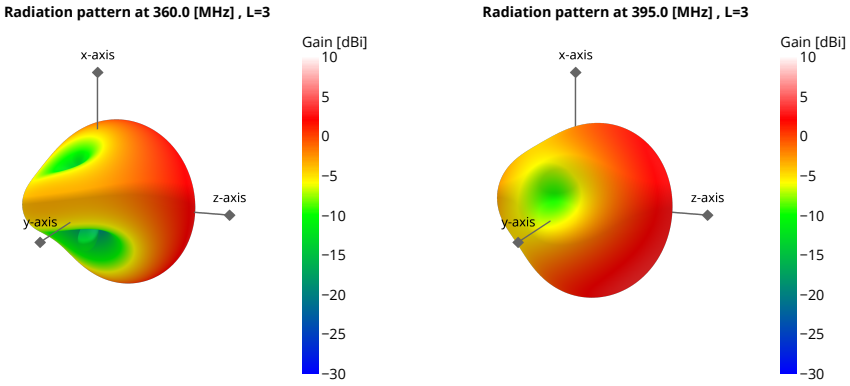

(a)

(b)

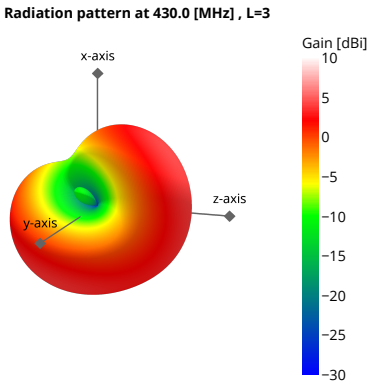

(c)

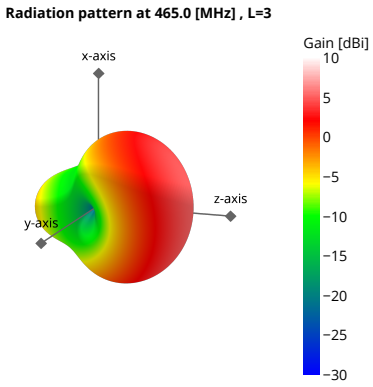

(d)

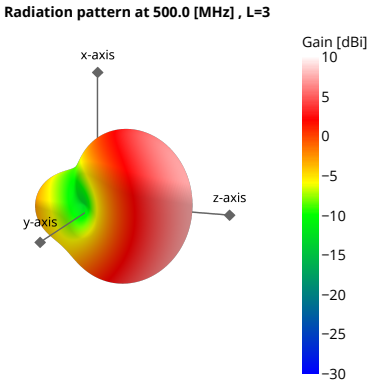

(e)

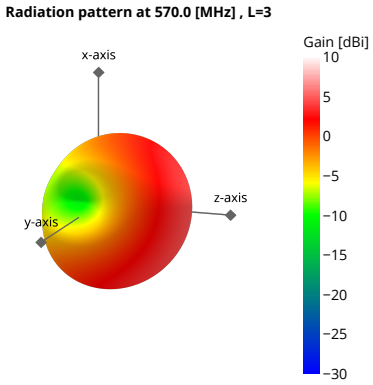

(f)

Figure B.23: These charts display the interpolated radiation patterns at frequencies 360-570 MHz and L=3.

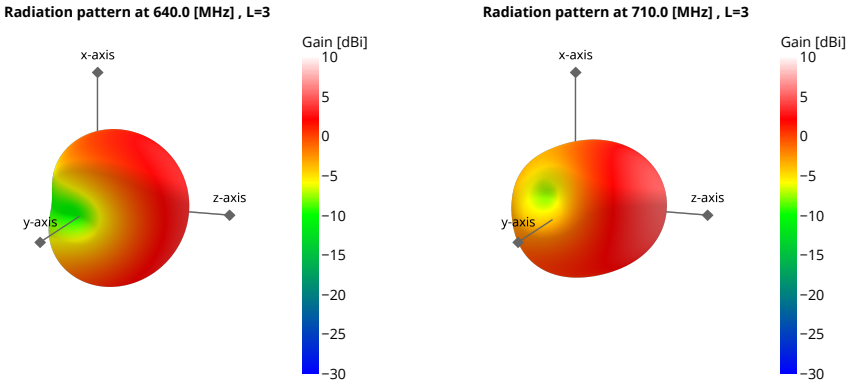

(a)

(b)

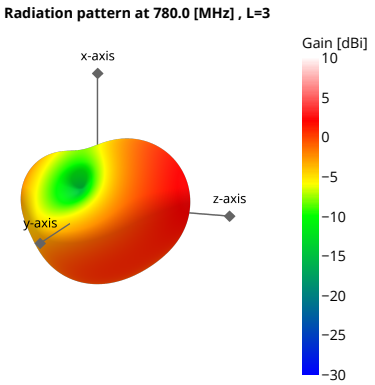

(c)

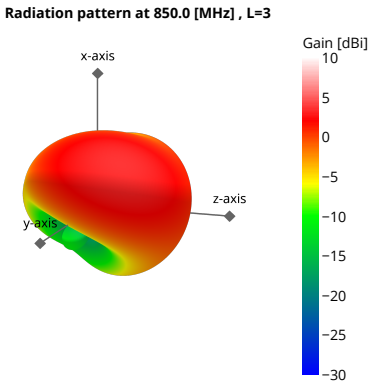

(d)

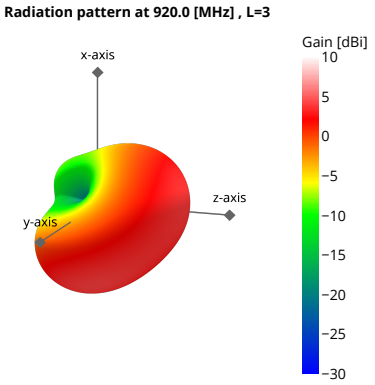

(e)

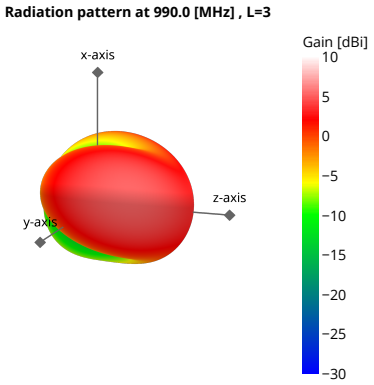

(f)

Figure B.24: These charts display the interpolated radiation patterns at frequencies 640-990 MHz and L=3.

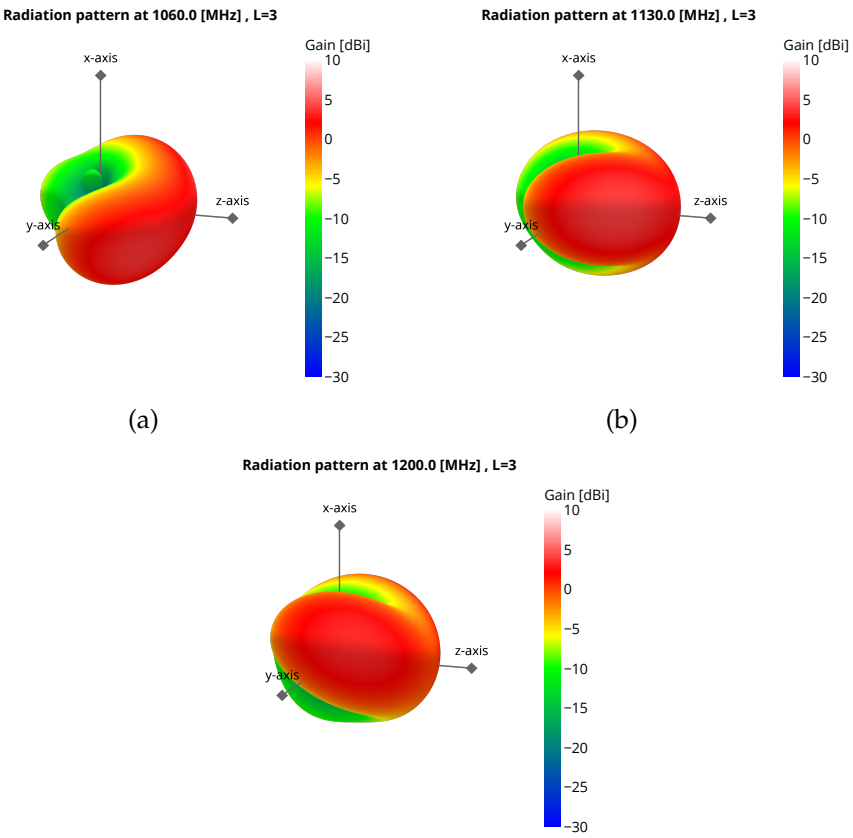

Figure B.25: These charts display the interpolated radiation patterns at frequencies 1060-1200 MHz and L=3.

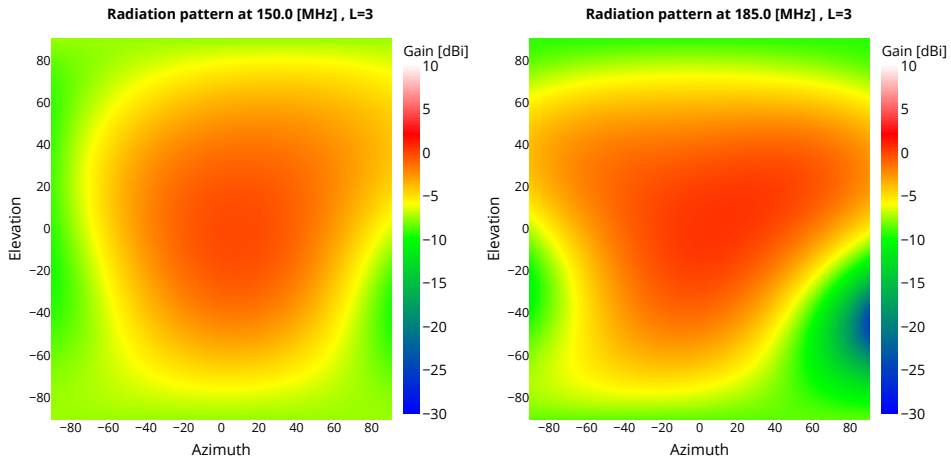

(a)

(b)

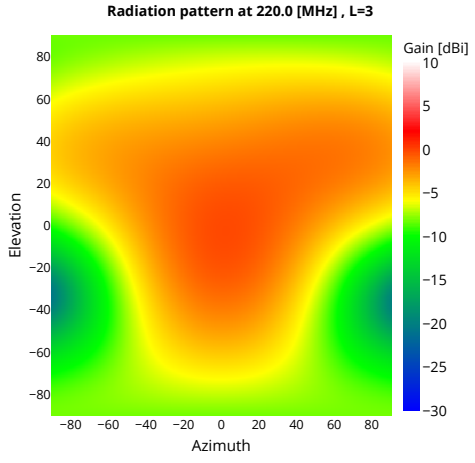

(c)

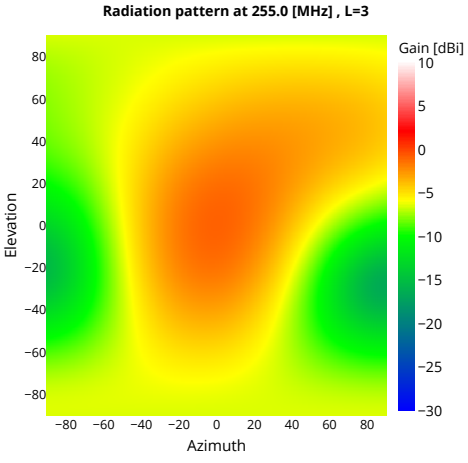

(d)

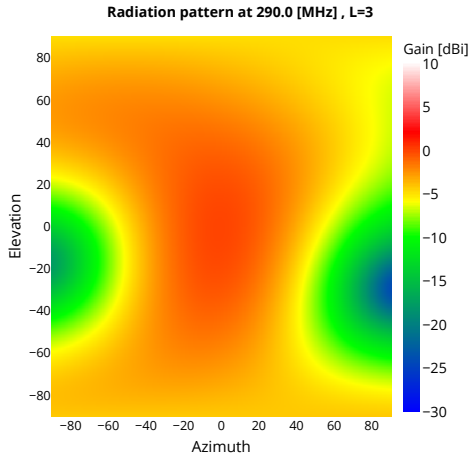

(e)

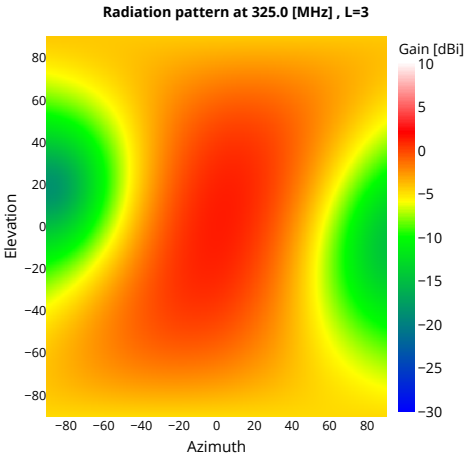

(f)

Figure B.26: These charts display the interpolated radiation pattern at frequencies 150-325 MHz and L=3.

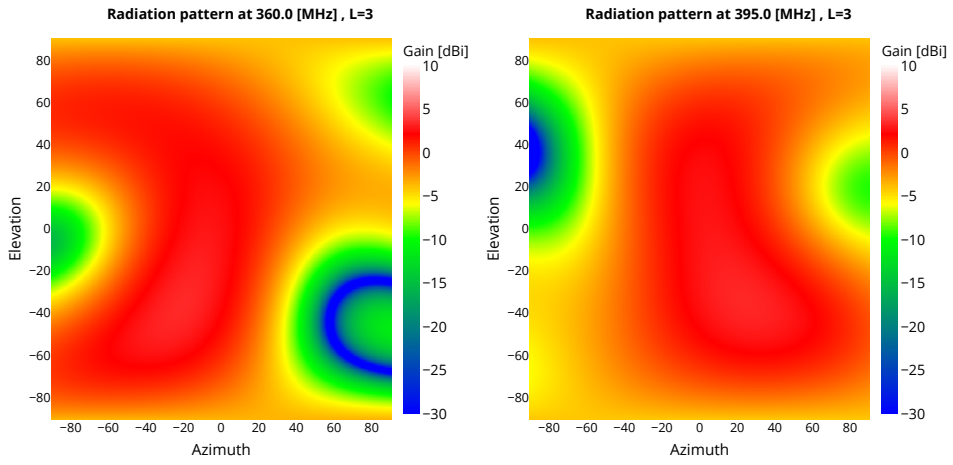

(a)

(b)

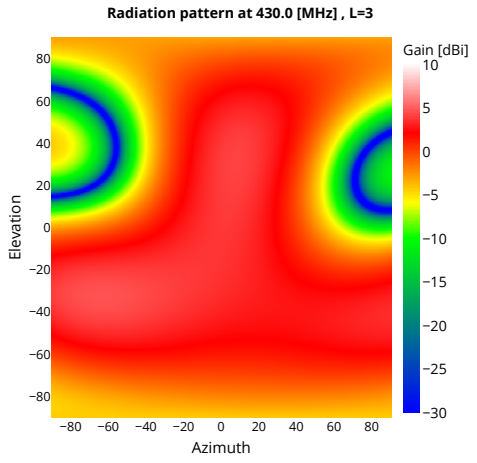

(c)

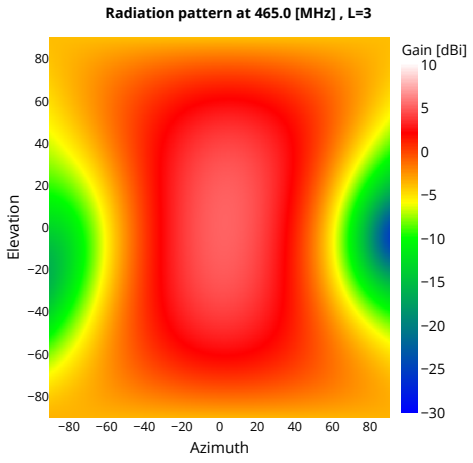

(d)

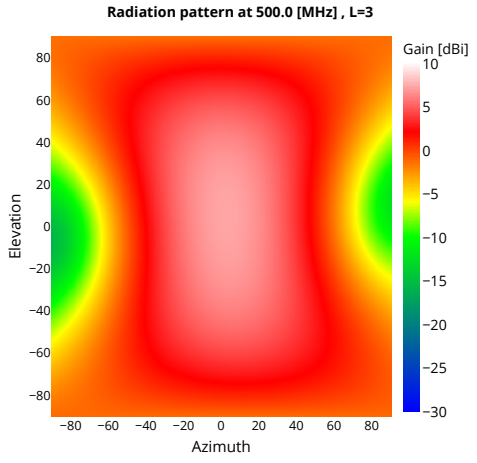

(e)

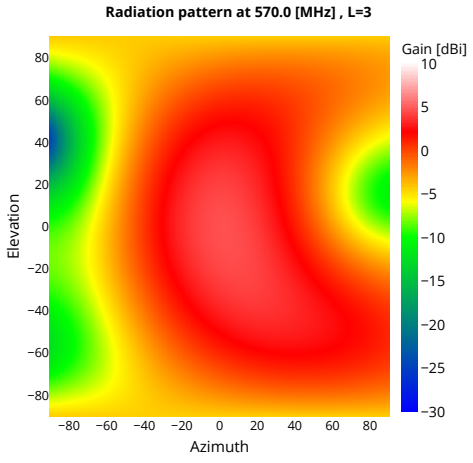

(f)

Figure B.27: These charts display the interpolated radiation pattern at frequencies 360-570 MHz and L=3.

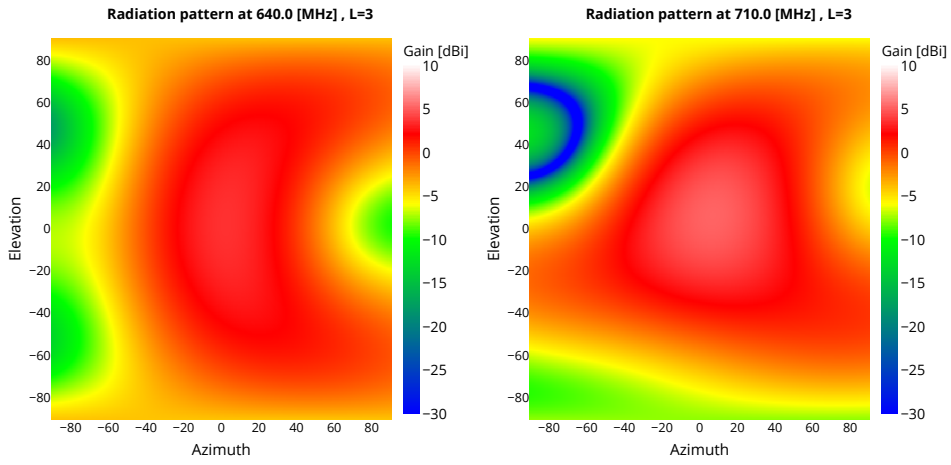

(a)

(b)

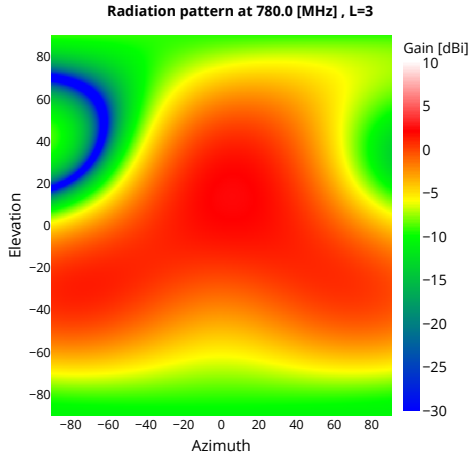

(c)

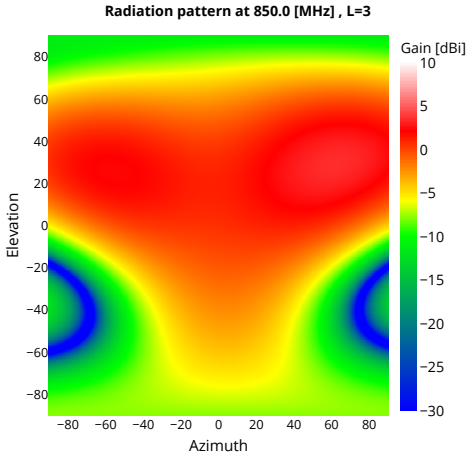

(d)

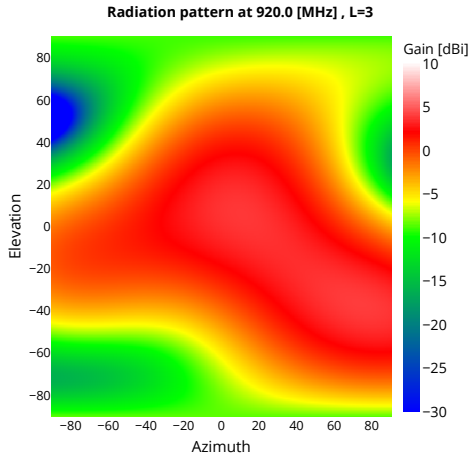

(e)

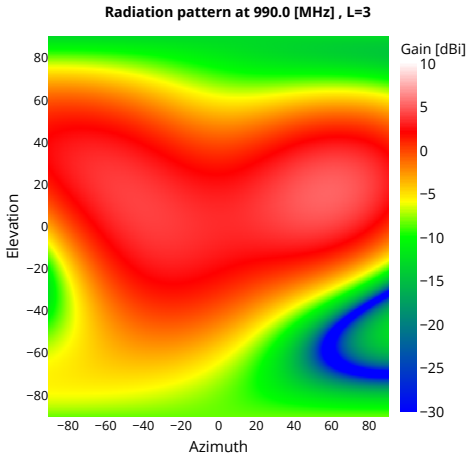

(f)

Figure B.28: These charts display the interpolated radiation pattern at frequencies 640-990 MHz and L=3.

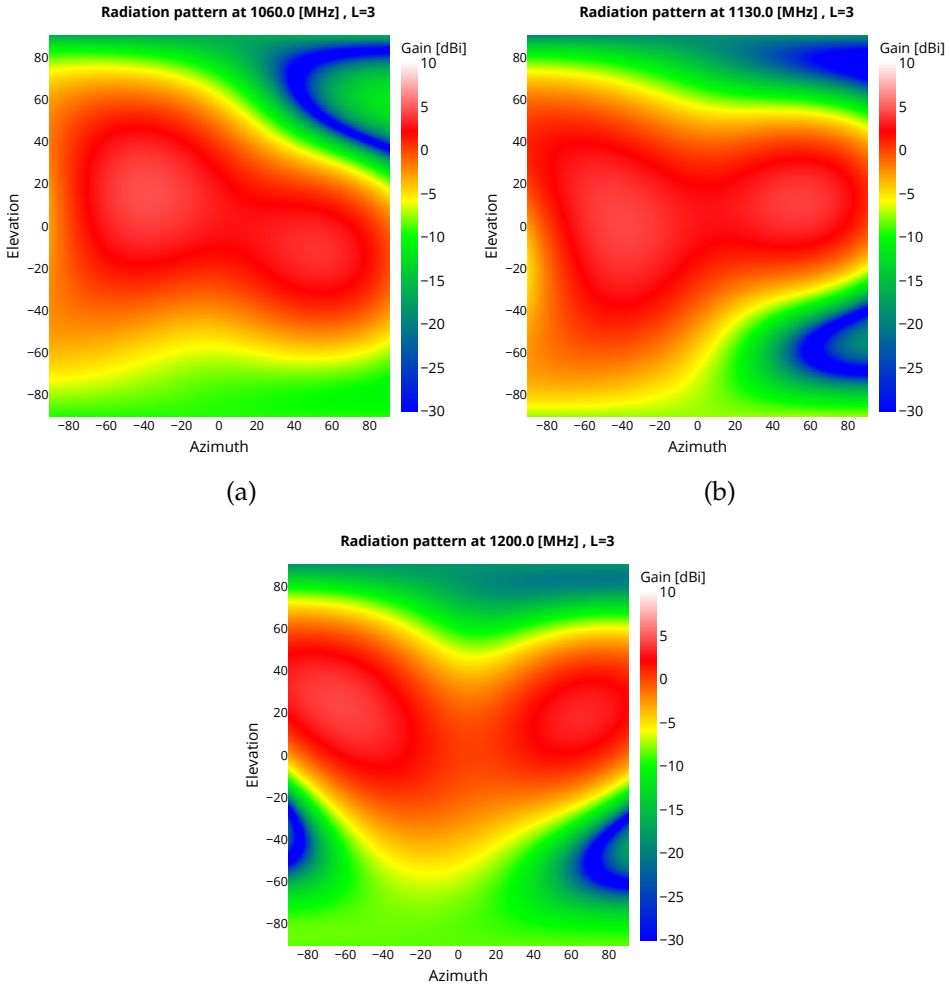

Figure B.29: These charts display the interpolated radiation pattern at frequencies 1060-1200 MHz and L=3.

Appendix C

Code

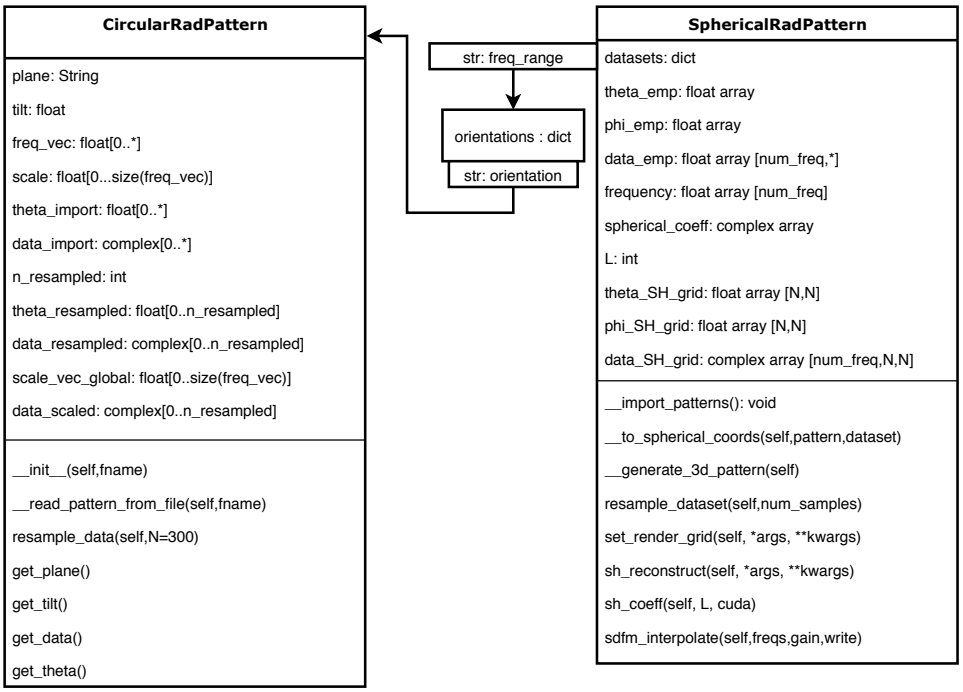

Figure C.1: UML diagram for the Spherical Harmonic interpolation.

L	coeff	reconstruct-cuda	reconstruct-cpu
5	0.01s	0.37s	0.19s
10	0.05s	0.20s	0.59s
15	0.11s	0.46s	1.42s
20	0.20s	0.88s	2.51s

Table C.1: Table showing the time taken to compute SH-coefficients and to reconstruct the model from the coefficients.

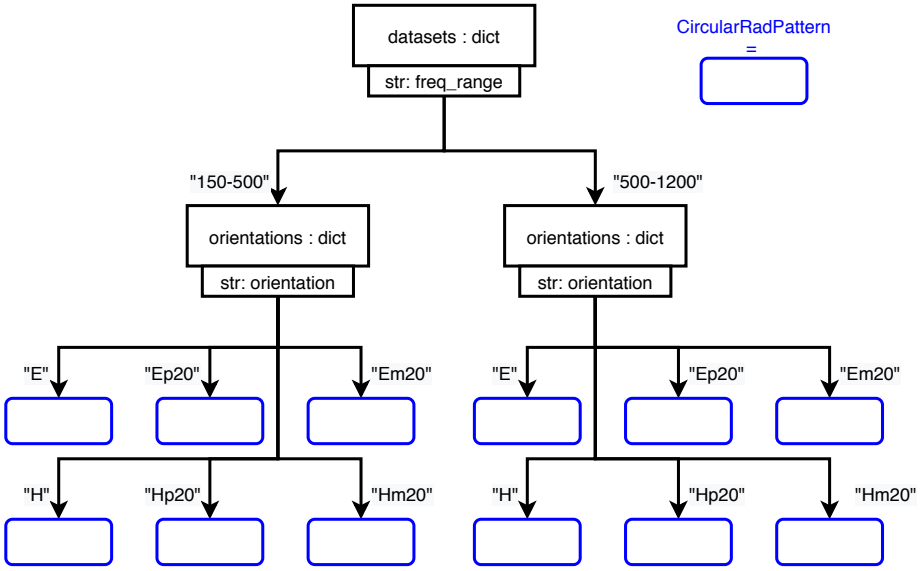

Figure C.2: The structure of the objects in the *datasets* dictionary from the *SphericalRadPattern* class in Fig. C.1. Each blue, rounded rectangle corresponds to a *CircularRadPattern* object, which represents one cut of the radiation pattern. Each of these objects have imported their data from a single file in the "Meas" directory, located within the "jupyterlab" directory.

```
self.L=L

N = int(np.power(L+1,2))
M = np.size(theta)
x = np.cos(theta)
e_i_phi = np.exp(1j*phi)
A = np.zeros([M,N],dtype=complex)
y = np.absolute(data[:,:])

i = 0
for l in range(0,L+1):
    for m in range(-l,l+1):
        #print(f"i: {i}, N: {N}")
        f = np.sqrt((2*l+1)*special.factorial((l-m))/ \
            (4*math.pi*special.factorial((l+m))))*\
            special.lpmv(m,l,x)*np.power(e_i_phi,m)
        A[:,i] = f
        i += 1
self.spherical_coeff = np.linalg.lstsq(A,y,rcond=-1)
```

Figure C.3: This algorithm finds the spherical harmonic coefficients from the preprocessed measurements.

```
num_freq = np.size(self.frequency)
theta = self.theta_render
phi = self.phi_render
spherical_coeff = self.spherical_coeff[0].T
data_modeled = np.zeros([num_freq,self.num_phi,self.num_theta],
                        dtype=complex)

i=0
for l in range(0,self.L+1):
    for m in range(-l,l+1):
        data_modeled = data_modeled+ \
                    (spherical_coeff[:,i,None,None]* \
                    special.sph_harm(m,l,phi,theta)[None,:,:]))
        i+=1
self.theta_SH_grid = theta
self.phi_SH_grid = phi
self.data_SH_grid = data_modeled
```

Figure C.4: The algorithm that reconstructs the radiation pattern from the SH coefficients. This the standard implementation that uses numpy and scipy.

```
num_freq = np.size(self.frequency)
theta = cp.asarray(self.theta_render)
phi = cp.asarray(self.phi_render)
x = np.cos(cp.asnumpy(theta))
e_i_phi = cp.exp(1j*phi)
spherical_coeff = cp.asarray(self.spherical_coeff[0].T)
data_modeled = cp.zeros([num_freq,self.num_phi,self.num_theta],
                        dtype=complex)

i=0
for l in range(0,self.L+1):
    for m in range(-l,l+1):
            C = cp.sqrt((2*l+1)*\
                cp.asarray(special.factorial((l-m))/ \
                    (4*math.pi*special.factorial((l+m)))))
            f_legendre = cp.asarray(special.lpmv(m,l,x))
            cp.cuda.Stream.null.synchronize()
            ### The SH coefficients are constant for all
            ### (theta,phi), while the two preceding functions
            ### are constant for all freq
            data_modeled = cp.add(data_modeled,
                            C*spherical_coeff[:,i,None,None]*\
                            f_legendre[None,:,:]*\
                            cp.power(e_i_phi,m)[None,:,:])
            i+=1
    cp.cuda.Stream.null.synchronize()
    self.theta_SH_grid = cp.asnumpy(theta)
    self.phi_SH_grid = cp.asnumpy(phi)
    self.data_SH_grid = cp.asnumpy(data_modeled)
```

Figure C.5: The algorithm that reconstructs the radiation pattern from the SH coefficients. This one was written in the CUDA-enabled library cupy.

```
def SDFM_interpolate(self,freqs,gain,write=False):
    """Interpolates a set of of gain/frequency measurements
    with a rational filter. Uses the same number of filter
    coefficients as the number of sampled frequencies."""
    field_strength = np.power(10,gain/10)
    num_freqs = 1000
    freq_interp = np.linspace(freqs[0],freqs[np.size(freqs)-1],
                              num_freqs)
    gain_interp = np.zeros([num_freqs,np.size(freqs)])
    nd_matrix = np.zeros([np.size(freqs),2],dtype=int)
    s_in = 2j*math.pi*freqs

    for n in range(0, np.size(freqs)):
        d = np.size(freqs)-1-n
        A = np.ones((np.size(freqs),n+d+1),
                    dtype=complex)
        B = np.ones((np.size(freqs),n+d+1),
                    dtype=np.dtype('U100'))
        for i in range(0,n+1):
            A[:,i] = np.power(s_in,i)
            B[:,i] = f's^{i}'
        for i in range(0,d):
            A[:,i+n+1] = -field_strength*np.power(s_in,i)
            B[:,i+n+1] = f'-F(s^{i})s^{i}'
        b = field_strength*np.power(s_in,d)
        x = np.linalg.solve(A,b)
        top_coeff = x[0:n+1]
        bottom_coeff = np.append(x[n+1:n+d+1], 1.0)
        s_out = 2j*math.pi*freq_interp
        freq_top = np.ones((np.size(freq_interp),n+1),
                           dtype=complex)
        for i in range(0,n+1):
            freq_top[:,i] = np.power(s_out,i)
        freq_bottom = np.ones((np.size(freq_interp),d+1),
                              dtype=complex)
        for i in range(0,d+1):
            freq_bottom[:,i] = np.power(s_out,i)
        top_eval = np.matmul(freq_top,top_coeff)
        bot_eval = np.matmul(freq_bottom,bottom_coeff)
        field_strength_interp = np.absolute(top_eval/bot_eval)
        gain_interp[:,n] = 20*np.log10(field_strength_interp)
        nd_matrix[n,:] = [n,d]
    return freq_interp,gain_interp,nd_matrix
```

Figure C.6: Function that interpolates a set of gain/frequency measurements using the Padé rational function.

```
function [] = gate_sim(win,length,pulse_width)
    Fs = 97.656e3;
    T_sweep = 3.125e-3;
    max_f = 1200e6;
    min_f = 150e6;
    ns = 1e-9;
    Fgate = 12500e3;
    FsGate = Fgate*1000;
    T = 1/Fgate;
    W = T/pulse_width;
    ramp_rate = (max_f-min_f)/T_sweep;

    reflector_if = ramp_rate*15*ns;
    reflector_if2 = ramp_rate*20*ns;

    t_pulse = -T/2:1/FsGate:T/2;
    pulse = rectpuls(t_pulse,W);
    num_periods = round(T_sweep/T);
    pulse_wave = repmat(pulse,1,num_periods);
    t_sine = linspace(0,numel(pulse_wave)/ ...
                      FsGate,numel(pulse_wave));
    reflectors = cos(2*pi*reflector_if*t_sine)+ ...
                 cos(2*pi*reflector_if2*t_sine);
    pulse_wave = pulse_wave.*reflectors;
    pw_windowed = pulse_wave;
    if win == 0
        pw_windowed = pulse_wave;
    elseif win == 1
        pw_windowed = pulse_wave.* ...
                      chebwin(numel(pulse_wave),72)';
    end
    magn_pw = db(abs(fftshift(fft(pw_windowed))));
    max_pw = max(magn_pw);
    magn_pw = magn_pw - max_pw;
    n_pw = numel(magn_pw);
    freq_pw = linspace(-FsGate/2,FsGate/2,n_pw);
    n_samples = length;
    freq_pw_extract = freq_pw(round(n_pw/2-n_samples): ...
                              round(n_pw/2+n_samples));
    magn_pw_extract = magn_pw(round(n_pw/2-n_samples): ...
                              round(n_pw/2+n_samples));
    delay = freq_pw_extract/ramp_rate;
end
```

Figure C.7: Gate-simulator written in MATLAB.

Appendix D

Miscellaneous

D.1 Derivation of the wave equation

Proof. The first step to derive the wave equation is to take the curl of equation 3.5.

$$\nabla \times \nabla \times \vec{E} = -\frac{\partial(\nabla \times \vec{B})}{\partial t}$$

By combining equation 3.4 with the constitutive equations, $\vec{D} = \varepsilon_0 \vec{E}$, $\vec{H} = \vec{B}/\mu_0$, and assume zero current $J = 0$, we get:

$$\nabla \times \vec{B} = \epsilon\mu \frac{\partial \vec{E}}{\partial t}$$

Hence,

$$\nabla \times \nabla \times \vec{E} = -\epsilon\mu \frac{\partial^2 \vec{E}}{\partial t^2}$$

We introduce the identity [18, p. 1]:

$$\nabla \times (\nabla \times \boldsymbol{A}) = \nabla(\nabla \cdot \boldsymbol{A}) - \nabla^2 \boldsymbol{A}$$

Because we assume there are no charges ($\nabla \cdot E = 0$), we can make the following simplification:

$$\nabla^2 \vec{E} = \epsilon\mu \frac{\partial^2 \vec{E}}{\partial t^2} \tag{D.1}$$

■

```
### This file explains how the empirical measurements
### of the RIMFAX antenna is encoded. Every extensionless
### file in the /Meas directory has the same encoding.
### Line 7 and out is repeated for each frequency.

Line 1-4: Header
Line 5: Number of samples - N
Line 6: Text - "Azimuth"

Line 7 to N+6: Every sampled direction in degrees
Line N+7: Frequency [MHz] <Space> Scale
Line N+8 to 2N+7: Every sampling of the electric field
                                    strength as a complex number
```

Figure D.1: The layout of the antenna measurement files.

Frequency [MHz]
150
185
220
255
290
325
360
395
430
465
500

(a) 150-500MHz

Frequency [MHz]
500
570
640
710
780
850
920
990
1060
1130
1200

(b) 500-1200MHz

Figure D.2: The measurement frequencies

D.2 Spatial interpolation methods

The methods in this section were first thought to be viable options for interpolating the radiation patterns. We will now discuss some of the issues with both of these methods.

D.2.1 The summing method

The simplest method for interpolating from plane cuts of the radiation pattern to full 3d directivity is the "summing method". The main idea is to assume the pattern is separable to orthogonal cuts,

$$G(\theta, \phi) = G_{XZ}(\theta) G_{YZ}(\phi)$$

Variations of this method has been shown to give a good overall approximation of the pattern, especially in the main lobe [32]. The problem with this method is that it only uses two orthogonal cuts as input. We would like a method that takes all the cuts illustrated in Fig. 3.4 into account.

D.2.2 Binomial interpolation

Binomial interpolation is a set of techniques that are very common in image processing. They have several implementations in python, so it is natural to explore whether they could be applied to solve our problem. Bilinear and bicubic are perhaps the most common examples of this type of interpolation. Bilinear requires four known values in a rectangular grid to compute the polynomial coefficients while bicubic requires 16.

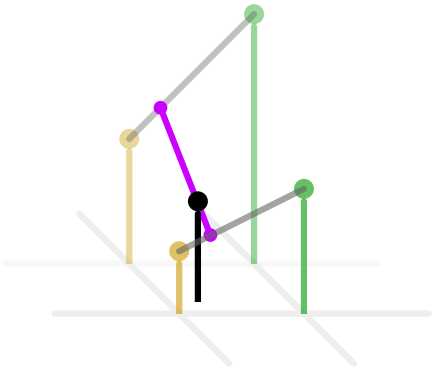

(a) Linear interpolation takes four values and interpolates between them.

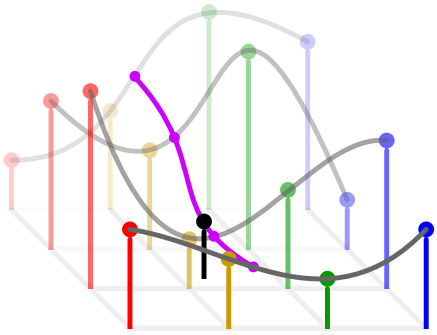

(b) Bicubic interpolation takes 16 points and interpolates between the four outermost points.

Figure D.3: Two interpolation methods. *Created by: Cmglee* (CC BY-SA 4.0). The original image displayed six interpolation methods.

Among the coordinate systems discussed in Section 3.6, Azimuth-Elevation brings the data closest to a rectangular grid. Close to the center of Fig. D.4, we have something that is almost a 9-point rectangular grid. Due to the 16-point restriction, it is clearly impossible to perform bicubic interpolation on

our data.

Linear interpolation can be performed in each of the four sub-rectangular shapes. The interpolated gain in each of these rectangles would only be based on the gain at the four edges of the rectangles. Because we cannot incorporate more than 9 data points into our model by using standard binomial interpolation, and because the model would be restricted to $|\theta|, |\phi| < 20°$, we have chosen not to use this method.

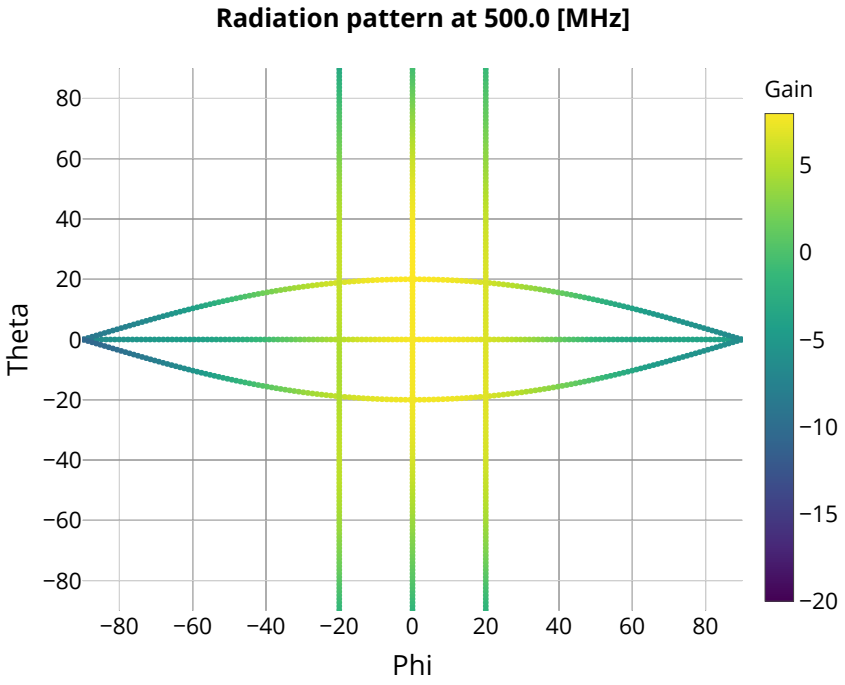

Figure D.4: The measured radiation pattern in the Azimuth-Elevation coordinates (from Fig. 3.3).

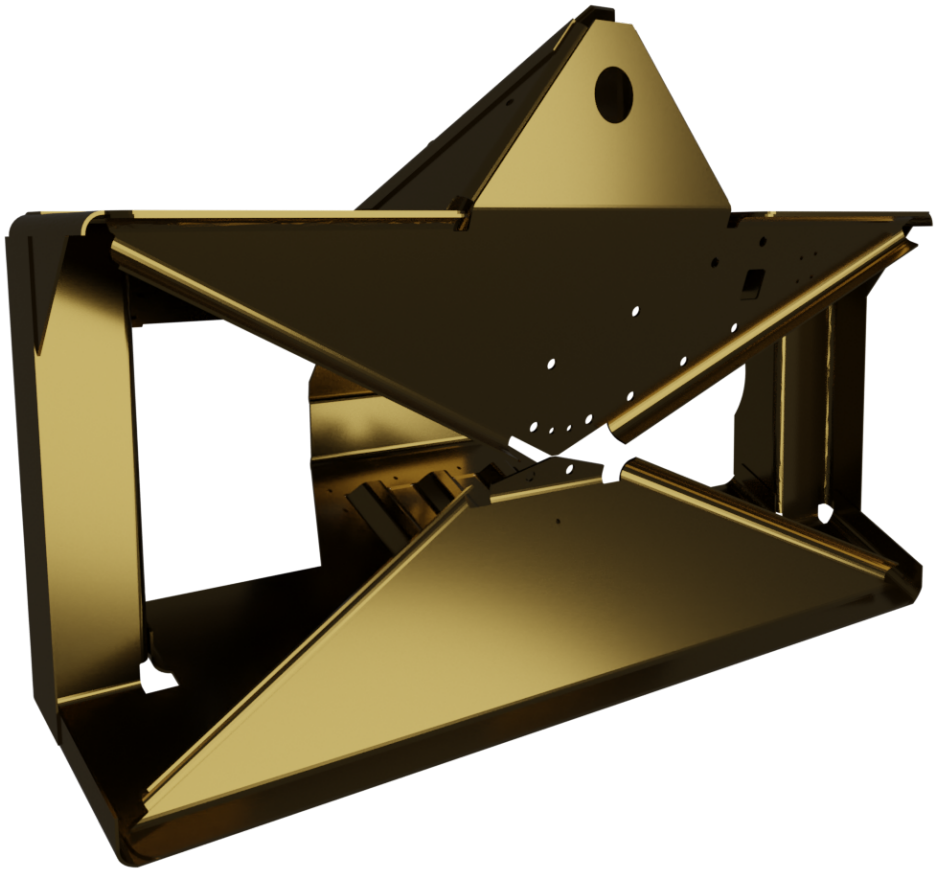

Figure D.5: RIMFAX antenna, rendered with blender.

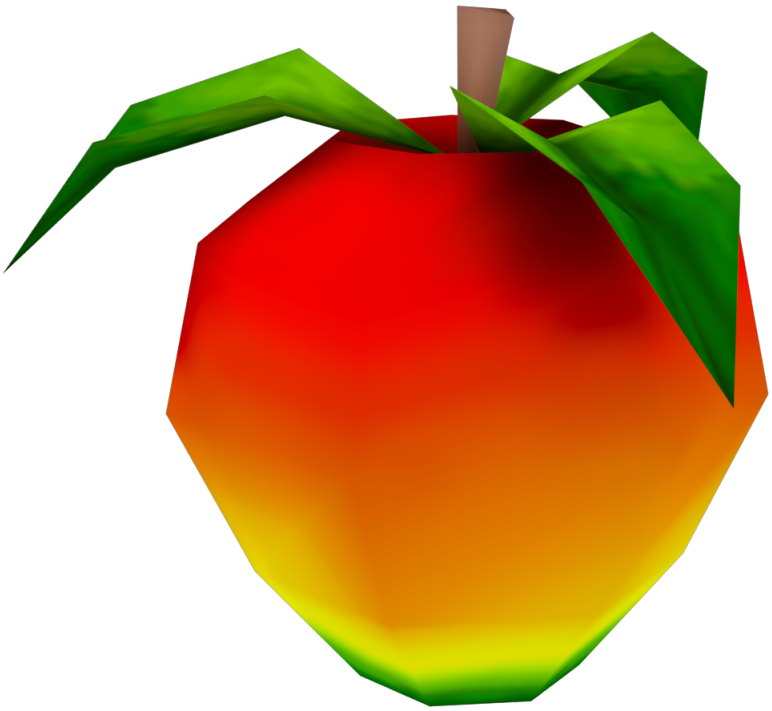

Figure D.6: A wumpa fruit. *Credits: Traveller's tales*.

References

[1] H. A. Wheeler, 'The Radiansphere around a Small Antenna,' *Proc. IRE*, vol. 47, no. 8, pp. 1325–1331, Aug. 1959.

[2] F. Ulaby, D. Long, W. Blackwell *et al.*, *Microwave Radar and Radiometric Remote Sensing*. Michigan: The University of Michigan Press, 1st Jan. 2014, ISBN: 978-0-472-11935-6.

[3] NASA. (2019). 'Launch Vehicle,' [Online]. Available: https://mars.nasa.gov/mars2020/mission/launch-vehicle/ (visited on 03/10/2019).

[4] ——, (2019). 'Rover,' [Online]. Available: https://mars.nasa.gov/mars2020/mission/rover/ (visited on 03/10/2019).

[5] ——, (2019). 'Instruments,' [Online]. Available: https://mars.nasa.gov/mars2020/mission/instruments/ (visited on 03/10/2019).

[6] Patrick S. Russell, Daniel C. Nunes, Svein-Erik Hamran *et al.*, 'RIMFAX Ground Penetrating Radar Field Tests in the Western USA,' in *LPSC*, vol. 51, Houston: Lunar and Planetary Institute, 2020.

[7] M. A. H. El-said, 'Geophysical Prospection of Underground Water in the Desert by Means of Electromagnetic Interference Fringes,' *Proc. IRE*, vol. 44, no. 1, pp. 24–30, Jan. 1956.

[8] L. Porcello, R. Jordan, J. Zelenka *et al.*, 'The Apollo lunar sounder radar system,' *Proc. IEEE*, vol. 62, no. 6, pp. 769–783, Jun. 1974.

[9] NIKU. (15th Oct. 2018). 'Georadar detects a Viking ship in Norway,' [Online]. Available: https://www.niku.no/en/2018/10/georadar-detects-a-viking-ship-in-norway/ (visited on 17/02/2020).

[10] A. P. Annan, *Ground Penetrating Radar: Principles, Procedures & Applications*. Mississauga, Canada: Sensors & Software Incorporated, 2003, 278 pp.

[11] NASA. (2019). 'Overview,' [Online]. Available: https://mars.nasa.gov/mars2020/mission/overview/ (visited on 11/09/2019).

[12] H. J. Melosh, *Planetary Surface Processes*. Cambridge: Cambridge University Press, 2011, 534 pp., ISBN: 978-0-511-97784-8.

[13] Editorial Team - everything RF. (22nd May 2018). 'What are Near Field and Far Field Regions of an Antenna? - everything RF,' [Online]. Available: https://www.everythingrf.com/community/what-are-near-field-and-far-field-regions-of-an-antenna (visited on 17/06/2020).

[14] Charles Capps, 'Near field or far field?' *EDN Mag.*, 16th Aug. 2001. [Online]. Available: https://people.eecs.ku.edu/~callen58/501/Capps2001EDNpp95.pdf.

[15] Jo Eide, *M2020 EM electrical test procedure*, Dec. 2017.

[16] R. Allard and D. Werner, 'The model-based parameter estimation of antenna radiation patterns using windowed interpolation and spherical harmonics,' *IEEE Trans. Antennas Propag.*, vol. 51, no. 8, pp. 1891–1906, Aug. 2003.

[17] B. Fuchs, L. Le Coq, S. Rondineau and M. D. Migliore, 'Fast Antenna Far-Field Characterization via Sparse Spherical Harmonic Expansion,' *IEEE Trans. Antennas Propag.*, vol. 65, no. 10, pp. 5503–5510, Oct. 2017.

[18] J. D. Jackson, *Classical Electrodynamics*, Third Edition. Wiley, 1998, 832 pp., ISBN: 978-0-471-30932-1.

[19] G. C. Cohen, 'Plane Wave Solutions,' in *Higher-Order Numerical Methods for Transient Wave Equations*, ser. Scientific Computation, Berlin: Springer, 2002, pp. 25–30, ISBN: 978-3-662-04823-8. [Online]. Available: https://doi.org/10.1007/978-3-662-04823-8_3 (visited on 23/06/2020).

[20] P. K. Koivisto, 'Reduction of Errors in Antenna Radiation Patterns Using Optimally Truncated Spherical Wave Expansion,' *Electromagnetic Waves*, pp. 313–333, 2004.

[21] Wikipedia contributors, *Gauss–Markov theorem*, in *Wikipedia*, 13th Jun. 2020. [Online]. Available: https://en.wikipedia.org/w/index.php?title=Gauss%E2%80%93Markov_theorem&oldid=962375436 (visited on 18/06/2020).

[22] E. Miller, 'Model-based parameter estimation in electromagnetics. I. Background and theoretical development,' *IEEE Antennas Propag. Mag.*, vol. 40, no. 1, pp. 42–52, Feb. 1998.

[23] ——, 'Model-based parameter estimation in electromagnetics. II. Applications to EM observables,' *IEEE Antennas Propag. Mag.*, vol. 40, no. 2, pp. 51–65, Apr. 1998.

[24] D. Werner and R. Allard, 'The simultaneous interpolation of antenna radiation patterns in both the spatial and frequency domains using model-based parameter estimation,' *IEEE Trans. Antennas Propag.*, vol. 48, no. 3, pp. 383–392, Mar. 2000.

[25] R. Johnston and J. McRory, 'An improved small antenna radiation-efficiency measurement method,' *IEEE Antennas Propag. Mag*, vol. 40, no. 5, pp. 40–48, Oct. 1998.

[26] D. Pozar and B. Kaufman, 'Comparison of three methods for the measurement of printed antenna efficiency,' *IEEE Trans. Antennas Propag.*, vol. 36, no. 1, pp. 136–139, Jan. 1988.

[27] S. Hamran, T. Berger, L. Hanssen and M. J. Oyan, 'Gated FMCW SAR System,' in *2008 38th European Microwave Conference*, Oct. 2008, pp. 1644–1647.

[28] S. .-E. Hamran, D. T. Gjessing, J. Hjelmstad and E. Aarholt, 'Ground penetrating synthetic pulse radar: Dynamic range and modes of operation,' *Journal of Applied Geophysics*, vol. 33, no. 1, pp. 7–14, 1st Jan. 1995. [Online]. Available: http : / / www . sciencedirect . com / science/article/pii/092698519590025X (visited on 25/09/2019).

[29] Sverre Brovoll, 'RIMFAX gating PowerPoint,' (Kjeller, Norway), Jan. 2019.

[30] ——, *RIMFAX gate measurements*, 2020.

[31] N. Pires, C. Mendes, M. Koohestani, A. K. Skrivervik and A. A. Moreira, 'Novel Approach to the Measurement of Ultrawideband Antenna Efficiency,' *IEEE Antennas Wireless Propag. Lett.*, vol. 12, pp. 1512–1515, 2013.

[32] T. Petrita and A. Ignea, 'A new method for interpolation of 3D antenna pattern from 2D plane patterns,' in *Proc. 10th ISETC*, 16th Nov. 2012.